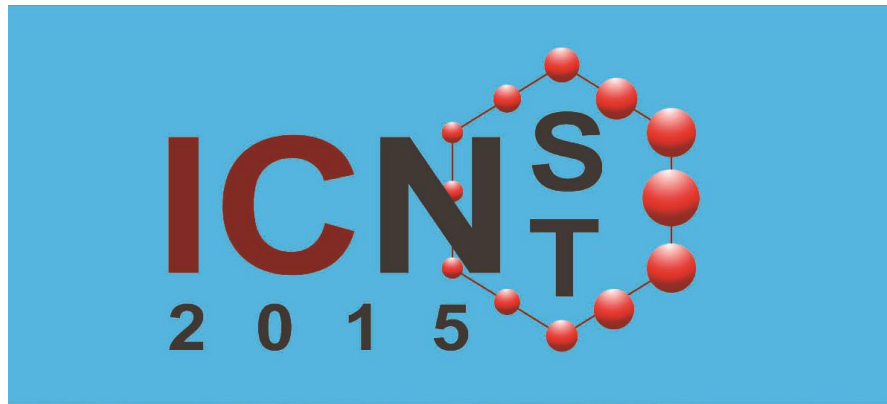




CONFERENCE PROCEEDINGS

CONFERENCE PROCEEDINGS



02nd – 04th September, 2015

Colombo, Sri Lanka

Committee of the ICNSNT- 2015

The International Institute of Knowledge Management (TIKM)

Tel: +94(0) 11 3132827

info@tiikm.com

Disclaimer

The responsibility for opinions expressed, in articles, studies and other contributions in this publication rests solely with their authors, and this publication does not constitute an endorsement by the ICNSNT or TIIKM of the opinions so expressed in them

Official website of the conference

www.nanoconference.co

Conference Proceedings of the 2nd International Conference on Nanoscience and Nanotechnology, 2015

Edited by Prof. K. M Nalin de Silva and Ms. Udayangani Premarathne

ISSN: 2386-1215

Copyright @ TIIKM

All rights are reserved according to the code of intellectual property act of Sri Lanka, 2003

Published by The International Institute of Knowledge Management (TIIKM)

Tel: +94(0) 11 3132827

Fax: +94(0) 11 2835571

Technical Co-sponsor:

Institute of Electrical and Electronics Engineers (IEEE)

IEEE Nanotechnology Council

Organized by:

The International Institute of Knowledge Management (TIKM)

ICNSNT 2015 Committee

PROF. K.M. NALIN DE SILVA

(Chair, ICNSNT 2015)

Professor of Chemistry, University of Colombo and Science Team Leader, Sri Lanka Institute of Nanotechnology (SLINTEC), Sri Lanka

PROF. R.M. GAMINI RAJAPAKSE

(Session Chair, ICNSNT 2015)

Senior Professor in Chemistry at the University of Peradeniya, Sri Lanka

PROF. P. RAVIRAJAN

(Session Chair, ICNSNT 2015)

Professor and Head, Department of Physics, University of Jaffna, Sri Lanka

DR. ROHINI M. DE SILVA

(Session Chair, ICNSNT 2015)

Department of Chemistry, University of Colombo, Sri Lanka

PROF. C. A. N. FERNANDO

(Session Chair, ICNSNT 2015)

Head/Chair/Department of Electronics, Senior Professor, Department of Electronics, Wayamaba University of Sri Lanka, Sri Lanka

DR. SHEHAN DE SILVA

(Session Chair, ICNSNT 2015)

Senior Research Scientist, Sri Lanka Institute of Nanotechnology

MR. ISANKA. P. GAMAGE

(Conference Convener, ICNSNT 2015)

The International Institute of Knowledge Management

MR. OSHADEE WITHANAWASAM

(Conference Publication Chair, ICNSNT 2015)

The International Institute of Knowledge Management

MISS. SUVINIE RAJAPAKSHA

(Conference Coordinator, ICNSNT 2015)

The International Institute of Knowledge Management

Editorial Board - ICNSNT - 2015

Editor in Chief

Prof. K.M. Nalin de Silva, *Professor of Chemistry, University of Colombo and Science Team Leader, Sri Lanka Institute of Nanotechnology (SLINTEC), Sri Lanka.*

Editorial Board

Prof. R.M. Gamini Rajapakse, *University of Peradeniya, Sri Lanka*

Mr. D. T. Rathnayake, *Faculty of Management Studies and Commerce, University of Sri Jayewardenepura, Sri Lanka*

Ms. Udayangani Premarathne, *The International Institute of Knowledge Management*

The Editorial Board is not responsible for the content of any research paper

Scientific Committee - ICNSNT - 2015

Dr. Yu Zhou, *Department of Chemistry, Northwestern University, USA.*

Prof. P. Pramanik, *Indian Institute of Technology Kharagpur, India*

Prof. P. Ravirajan, *University of Jaffna, Sri Lanka.*
Prof. Bharat Bhushan, *The Ohio State University, USA.*

Dr. K.Gurunathan, *Department of nanoscience and Technology, Alagappa University, India.*

Dr. Mohamed Bououdina, *College of Science, University of Bahrain, Bahrain.*

Dr. R. P. Singh, *Amity Institute of Nanotechnology, India.*

Dr. T. Theivasanthi, *International Research Centre of Kalasalingam university. India.*

MESSAGE FROM PROF. K.M. NALIN DE SILVA

CONFERENCE CHAIR – ICNSNT 2015

Welcome to the 2nd Annual International Conference on Nanoscience and Nanotechnology.

It is my great pleasure to invite the community of research scientists, academics and postgraduate students to participate in the 2nd Annual International Conference on Nanoscience and Nanotechnology to be held in Colombo, Sri Lanka during 2-4 September 2015. It has been a real honor and privilege to serve as the Chair of this conference. First International Conference on Nanoscience and Nanotechnology 2014 was successfully completed with more than 60 participants from 19 countries. TIIKM has brought together a rich diversity of authors and speakers from various universities and industry covering more than 16 countries to share ideas and new perspectives on a wide range of topics related to nanoscience and nanotechnology.

The conference focuses on many areas through the Keynotes Speeches, Invited Talks, and Technical Program. This year we have carefully selected few areas such as Textile & Apparel, smart agriculture, energy, water purification, nanobiotechnology, computational nanoscience, and nanotechnology safety & policy. The conference will be organized by the experienced local organizing committee at TIIKM. There will be a significant participation by researchers from local universities and industrial organizations and the potential for collaboration and cross fertilization across borders would be substantial, especially due to the fact that Sri Lanka has already started the nanotechnology programme through a national nanotechnology initiative by setting up Sri Lanka Institute of Nanotechnology (SLINTEC), a world class fifty acre nanotechnology and science park comprising nanotechnology center of excellence equipped with state of the art equipment for nano characterization.

As the Chair of the conference I am requesting you to submit an abstract and participate in the ICNST 2015. Extended versions of selected papers from the conference will be published after peer review. I am confident that these experienced local organizers TIIKM will make the ICNST 2015 an unforgettable event for all the participants. I would also like to invite you to attend this most enjoyable gathering of scientists belonging to the universities and industries from many countries across the globe.

Prof. K.M. Nalin de Silva

Professor of Chemistry / University of Colombo,
Science Team Leader / Sri Lanka Institute of Nanotechnology,
Sri Lanka.

MESSAGE FROM PROF. MORINOBU ENDO

KEYNOTE SPEAKER - ICNSNT 2015

It is my great honor to send this message to the ICNSNT 2015 and to be a member of the scientific committee organized by the International of Knowledge and Management TIIKM during 2-4 September 2015 at Colombo, Sri Lanka.

Nanoscience and nanotechnology (NS&NT) are very important fields for engineering in the 21st century, in both developed and developing countries, as fundamentals of knowledge and technology as well. NS&NT are very different from conventional science fields, such as chemistry, physics, biology, because at the nanolevel these fields are totally fused and there is no boundary anymore. So, from such new fields of NS&NT, we can expect innovations that will contribute to the sustainability of human beings in the current century.

I hope that the present conference can promote the development for such an important and advanced field of NS&NT in this country and at the global level.

Prof. Morinobu Endo

Department of Electrical and Electronic Engineering, Faculty of Engineering,
Shinshu University, Japan.

Table of Contents	Page No
1. Synergistic Effect of Photocatalytic Ozonation in Phenol Degradation <i>C.A. Mecha, M.S. Onyango, O. Aoyi and M.N.B. Momba</i>	01
2. Phytofabrication of Silver Nanoparticles using <i>Riccia</i> Sp. <i>J.A.M.S. Jayasinghe, B.S. Dassanayake and S.C.K. Rubasinghe</i>	05
3. Facile Synthesis of Hydroxyapatite/ Iron Oxide Nanocomposite to be used as a Drug Carrier <i>D. C. Manatunga, W.R.M.de Silva and K.M.N.de Silva</i>	15
4. Comparison of Surface Morphology of Smooth Versus Porous Microfibres Made from Poly(L-Lactide) <i>Eva Macajová, Marcela Cudlínová and Pavel Kejzlar</i>	39
5. Analyzing the Multi-Resonant Property of Graphene Optical Nanoantenna <i>Jie Yang and Fanmin Kong</i>	45
6. Synthesis of Silver Nanoparticles using the Medicinal Plant <i>Pterocarpus marsupium</i> and Evaluation of its Antimicrobial Activities <i>S. Parvathy and B.R. Venkatraman</i>	50
7. Photovoltaic Performance of CaCO ₃ -Coated SnO ₂ -Based Dye-Sensitized Solar Cells with Composite Liquid/Quasi-Solid-State Electrolytes <i>W. M. N. M. B. Wanninayake, K. Premaratne and R. M. G. Rajapakse</i>	56
8. Effect of Acid on Nanovanadium Oxide <i>Hirihattaya Phetmung, Sirirat Prompakdee and Parachute Kong rat</i>	61

SYNERGISTIC EFFECT OF PHOTOCATALYTIC OZONATION IN PHENOL DEGRADATION

Mecha, C.A^{1,3*}, Onyango, M.S¹, Aoyi, O² and Momba, M.N. B^{3**}

¹Department of Chemical, Materials and Metallurgical Engineering, Tshwane University of Technology, Pretoria, South Africa

²Centre for Renewable Energy and Water, Vaal University of Technology, Vanderbijlpark, South Africa

³Department of Environmental, Water and Earth Sciences, Tshwane University of Technology, Pretoria, South Africa

Abstract

Advanced oxidation processes such as photocatalysis and ozonation have shown tremendous potential in water treatment. However, their major challenges are that photocatalysis is a relatively slow process whereas ozonation by molecular ozone is highly selective. This study demonstrates how simultaneous photocatalytic ozonation can be used to overcome these drawbacks by the synergistic generation of highly reactive and nonselective hydroxyl radicals. Titanium dioxide (TiO₂) nanoparticles were synthesized and their photocatalytic effectiveness investigated. The photocatalytic ozonation activity of the catalysts was evaluated by the degradation of 50 ppm phenol in aqueous solution using Ultraviolet (UV) radiation coupled with ozonation. The results showed that over 90% phenol degradation was achieved using UV photocatalytic ozonation in 60 minutes compared to the 240 minutes required to achieve 50% degradation (ozonation) and 45% degradation (UV photocatalysis). Total organic carbon analysis indicated that photocatalytic ozonation achieved over 80% mineralization of phenol whereas photocatalysis achieved 40% and ozonation 15% in 240 minutes. The study demonstrated that photocatalytic ozonation enhanced the oxidation process resulting in faster reactions and higher removal rates of phenol (more than the sum of photocatalysis and ozonation) due to the production of hydroxyl radicals by ozone over TiO₂.

Keywords: ozonation, phenol, photocatalysis, photo catalytic ozonation, titanium dioxide

INTRODUCTION

Water detoxification is important for environmental protection which is an important aspect of sustainability. Advanced oxidation processes (AOPs) such as photocatalysis and ozonation have unique advantages in water treatment. For instance, the ability of AOPs to mineralize bio-recalcitrant organic contaminants to harmless products such as carbon dioxide and water (Oyama et al., 2009) is a major advantage compared to the alternative treatment processes (membrane separation, activated carbon adsorption, chemical coagulation), which generate more wastes that need further removal steps which have cost implications (Ahmed, Rasul, Martens, Brown, & Hashib, 2010). Contamination of water sources with organic micro-pollutants such as phenolic compounds which are endocrine disrupting is detrimental to human health. Their removal is

therefore essential for environmental protection and to make the water reusable. Titanium dioxide (TiO₂) is the semiconductor catalyst that is most extensively used in photocatalysis due to its unique advantages such as high physical and chemical stability, high catalytic activity and oxidative power, low cost and ease of production (Subrahmanyam, Biju, Rajesh, Jagadeesh Kumar, & Raveendra Kiran, 2012). UV irradiation of ozone promotes the formation of .OH radicals by the rapid decomposition of ozone. Therefore, the application of photocatalytic ozonation in the removal of organic contaminants is superior to that by O₃ alone and UV irradiation photocatalysis because of the direct UV photodegradation, direct ozone oxidation and by the .OH radicals oxidation. Ozone is able to generate .OH radicals on the TiO₂ surface through the formation of the ozonide radical ion (O₃⁻), leading to a synergistic performance between photocatalysis and ozonation) (Kim &

Tanaka, 2011). In this study, heterogeneous photocatalysis and ozonation have been applied individually and in combination (photocatalytic ozonation) in the degradation of phenol solutions. The results were used to investigate the performance of the process with phenol removal efficiency and total organic carbon (TOC) as measurement criteria.

MATERIALS AND METHODS

Materials

The materials and chemicals used in the study together with the synthesis of TiO₂ nanoparticles was described in our previous study (Mecha, Onyango, Aoyi, & Momba, 2014). The process flow diagram for photocatalysis ozonation is depicted in Figure 1.

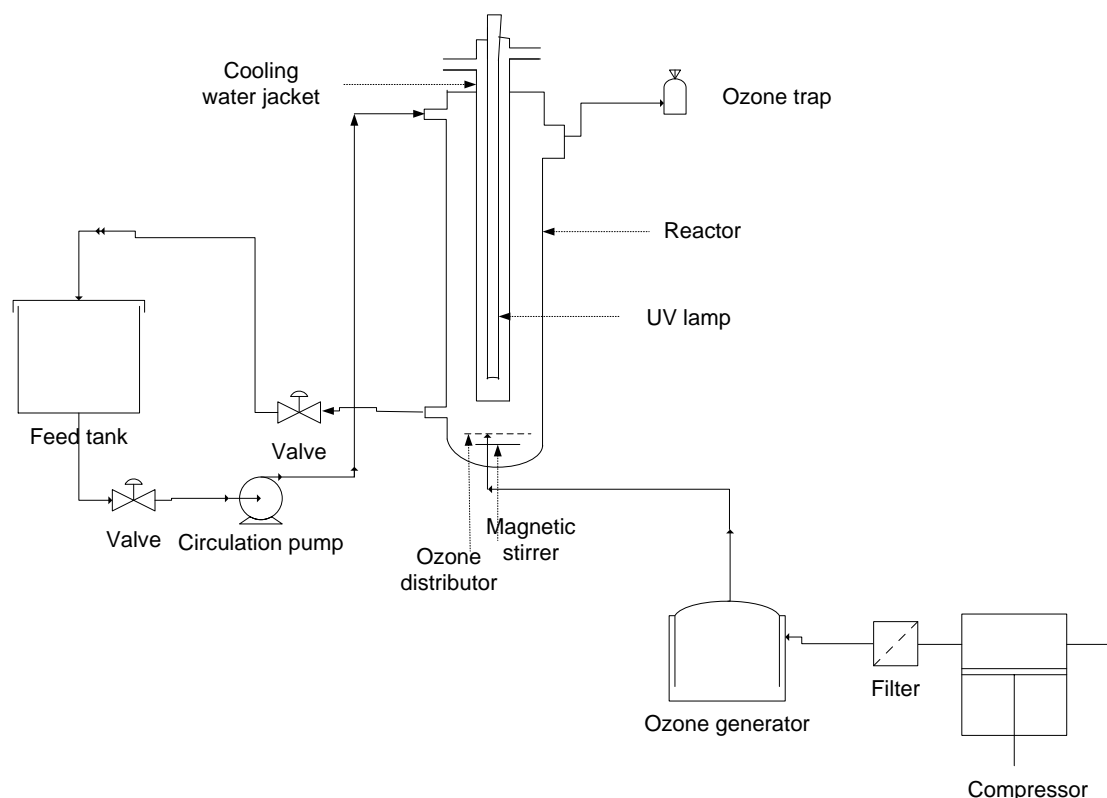


Figure 1. Process flow diagram for the photocatalytic ozonation scheme

Methods

Treatment of phenol solutions was done using three processes: ozonation, photocatalysis and photocatalytic ozonation in order to explore comparative performance. During ozonation, the UV lamp was switched off and the TiO₂ catalyst was not added; during photocatalysis, the ozone supply was closed and the catalyst was added and the UV lamp switched on and air was supplied. Photocatalytic ozonation was conducted with continuous supply of ozone and with the UV lamp switched on and in the presence of a catalyst. Phenol degradation performance assessment was conducted using a UV-Vis spectrophotometer at 270 nm while the mineralization efficiency was determined by analysis

of total organic carbon using Shimadzu TOC equipment.

RESULTS AND DISCUSSION

Phenol degradation efficiency

The rate of disappearance of phenol was monitored using UV-Vis spectrophotometer. Figure 2 shows the disappearance of phenol for the different processes investigated.

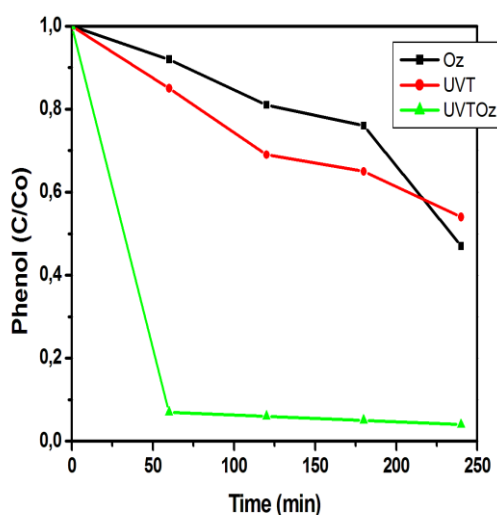


Figure 2. Degradation of 50 ppm phenol using ozonation, UVT and UVTOz

It was found that the removal of phenol from water was 50% for ozonation, 45% for photocatalysis (UVT) and 99% for photocatalytic ozonation (UVTOz) over a period of 240 minutes. It was further noted that over 90% of the phenol degradation using UVTOz occurred in 60 minutes as opposed to the 240 minutes required to achieve 50% (ozonation) and 45% (UVT). Therefore, photocatalytic ozonation resulted not only in increased degradation efficiency, but also, in significant reduction of the reaction time. It was readily observed that at a time of 60 minutes, the sum of the degradation by the individual processes was hardly 20% whereas; the combined process achieved 90% removal over the same period. This clearly indicated that there was synergy in the two processes probably due to the enhanced production of highly reactive $\cdot\text{OH}$ radicals.

Phenol mineralization efficiency

The TOC removal is plotted as a function of time in Figure 3 for ozonation, photocatalysis and photocatalytic ozonation.

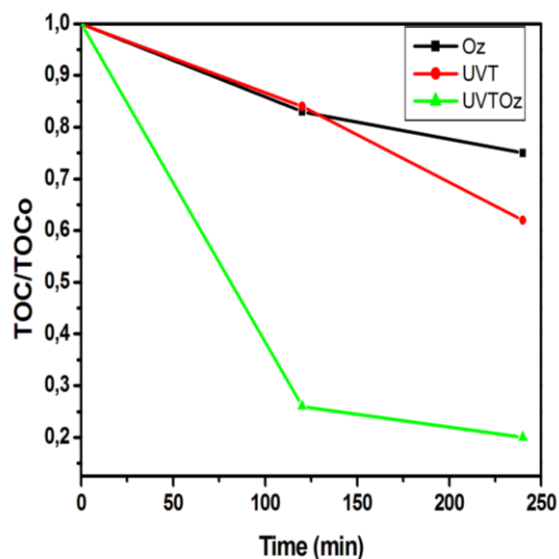


Figure 3. TOC profiles for 50 ppm phenol degradation using ozonation, UVT and UVTOz

It was observed that mineralization of phenol and the resulting intermediate compounds was 15% for ozonation, 40% for photocatalysis (UVT) and 80% for photocatalytic ozonation (UVTOz). A closer look revealed that 75% of the mineralization was achieved in 120 minutes for the combined process and increased to 80% in 240 minutes. The combined process achieved better mineralization efficiency over the period of the experiment. Photocatalytic ozonation is a complex three phase reaction which involves ozonation, photolysis, photocatalysis, photo-ozonation and photocatalytic ozonation (Chen, Xie, Yang, Cao, & Zhang, 2014), hence when these processes work together, they can be very effective in the mineralization of organics. Moreover, effects of synergy were much pronounced since the sum of the mineralization efficiencies of the individual processes in 240 minutes was 55% compared to 80% achieved by the combined process.

Comparing Figures 2 and 3, it was inferred that phenol degradation was faster than mineralization and this could be due to the fact that phenol degradation occurs in stages leading to the production of intermediate compounds which contribute to the TOC. Previous studies have shown that the degradation pathway of phenol during oxidation occurs via the $\cdot\text{OH}$ radicals attack on the phenyl ring, yielding catechol, resorcinol and hydroquinone, then the phenyl rings in these compounds break up to give

malonic acid, then short-chain organic acids such as maleic, oxalic, acetic and formic acids, and finally CO₂ (Grabowska, Reszczyńska, & Zaleska, 2012; Liotta, Gruttadauria, Carlo, Perrini, & Librando, 2009; Moreno-Piraján & Giraldo, 2013). In this regard, the low mineralization achieved by ozonation could be attributed to the oxidation of phenol into acidic type intermediates which are resistant to the attack by molecular ozone which is highly selective (Gurol & Vatistas, 1987). Similarly, since UV photocatalysis is also based on the production of ·OH radicals, this resulted in better TOC removal in photocatalysis compared to ozonation. Apart from the ·OH radicals, the synergistic effect could also be enhanced by the retardation of electron-hole recombination on the surface of TiO₂ resulting from the reaction between ozone and electrons (Shinpon, Fumihide, & Katsuyuki, 2002).

CONCLUSIONS

Ozonation, heterogeneous photocatalysis and their combination were studied for the oxidation of phenol in aqueous solution. The study revealed that photocatalytic ozonation is particularly effective for water detoxification since the oxidation of phenol was significantly increased with respect to the sum of the degradation by individual processes (ozonation and UV photocatalysis). The combined process resulted in significant improvement in phenol degradation and mineralization together with a significant reduction in the process time. This enhanced performance of UVTOz was postulated to occur due to the synergistic effects created by the production of hydroxyl radicals and the reduction of electron-hole recombination on the TiO₂ surface by ozone. The very high phenol concentrations employed in this study (50 ppm) is far greater than the concentration in environmental samples (normally <1 ppm). Therefore, the use of UVTOz has potential to completely remove recalcitrant organic micro-pollutants in water.

ACKNOWLEDGMENT

The authors would like to thank the National Research Foundation (NRF), South Africa and the Tshwane University of Technology for funding this study. The Egypt – South Africa joint project collaboration is highly appreciated.

REFERENCES

- Ahmed, S., Rasul, M. G., Martens, W. N., Brown, R., & Hashib, M. A. (2010). Heterogeneous photocatalytic degradation of phenols in wastewater: A review on current status and developments. *Desalination*, 261(1–2), 3–18. doi: <http://dx.doi.org/10.1016/j.desal.2010.04.062>
- Chen, Y., Xie, Y., Yang, J., Cao, H., & Zhang, Y. (2014). Reaction mechanism and metal ion transformation in photocatalytic ozonation of phenol and oxalic acid with Ag⁺/TiO₂. *Journal of Environmental Sciences*, 26, 662–672.
- Grabowska, E., Reszczyńska, J., & Zaleska, A. (2012). Mechanism of phenol photodegradation in the presence of pure and modified-TiO₂: A review. *Water Research*, 46(17), 5453–5471. doi: <http://dx.doi.org/10.1016/j.watres.2012.07.048>
- Gurol, M. D., & Vatistas, R. (1987). Oxidation of phenolic compounds by ozone and ozone + u.v. radiation: A comparative study. *Water Research*, 21(8), 895–900. doi: [http://dx.doi.org/10.1016/S0043-1354\(87\)80006-4](http://dx.doi.org/10.1016/S0043-1354(87)80006-4)
- Kim, I., & Tanaka, H. (2011). Energy Consumption for PPCPs Removal by O₃ and O₃/UV. *Ozone: Science & Engineering*, 33, 150–157.
- Liotta, L. F., Gruttadauria, M., Carlo, G. D., Perrini, G., & Librando, V. (2009). Heterogeneous catalytic degradation of phenolic substrates: Catalysts activity. *Journal of Hazardous Materials*, 162, 588–606.
- Mecha, A. C., Onyango, M. S., Aoyi, O., & Momba, M. N. (2014, Nov. 24–25, 2014). Enhanced activity of metal doped titanium dioxide in photo catalytic ozonation. Paper presented at the Int'l Conf. on Chemical Engineering & Advanced Computational Technologies (ICCEACT'2014) River Meadow Manor, Centurion, Pretoria (South Africa).
- Moreno-Piraján, J. C., & Giraldo, L. (2013). Comparison of the Oxidation of Phenol with Iron and Copper Supported on Activated Carbon from Coconut Shells. *Arab J Sci Eng*, 38, 49–57.
- Oyama, T., Yanagisawa, I., Takeuchi, M., Koike, T., Serpone, N., & Hidaka, H. (2009). Remediation of simulated aquatic sites contaminated with recalcitrant substrates by TiO₂/ozonation under natural sunlight. *Applied Catalysis B: Environmental*, 91, 242–246. doi: [10.1016/j.apcatb.2009.05.031](http://dx.doi.org/10.1016/j.apcatb.2009.05.031)
- Shinpon, W., Fumihide, S., & Katsuyuki, N. (2002). A synergistic effect of photocatalysis and ozonation on decomposition of formic acid in an aqueous solution. *Chemical Engineering Journal*, 87(2), 261–271. doi: [http://dx.doi.org/10.1016/S1385-8947\(02\)00016-5](http://dx.doi.org/10.1016/S1385-8947(02)00016-5)
- Subrahmanyam, A., Biju, K. P., Rajesh, P., Jagadeesh Kumar, K., & Raveendra Kiran, M. (2012). Surface modification of sol gel TiO₂ surface with sputtered metallic silver for Sun light photocatalytic activity: Initial studies. *Solar Energy Materials and Solar Cells*, 101(0), 241–248. doi: <http://dx.doi.org/10.1016/j.solmat.2012.01.023>

PHYTOFABRICATION OF SILVER NANOPARTICLES USING *Riccia* SP.

Jayasinghe, J.A.M.S¹, Dassanayake, B.S^{1,2} and Rubasinghe, S.C.K^{1,3,*}

¹Postgraduate Institute of Science, University of Peradeniya, Peradeniya, Sri Lanka

²Department of Physics, Faculty of Science, University of Peradeniya, Peradeniya, Sri Lanka

³Department of Botany, Faculty of Science, University of Peradeniya, Peradeniya, Sri Lanka

Abstract

Plant-mediated synthesis is a cost-effective eco-friendly method to produce silver nanoparticles. In this study, ethanolic plant extracts of *Riccia* sp. were used as the reductive source while low concentrations (1- 10 mM) of AgNO₃ were chosen as the source of silver. Formation of silver nanoparticles was observed by a colour change from light green to reddish-brown and confirmed by Energy Dispersive X-ray (EDX) measurements. An absorption peak resulting from silver nanoparticles was obtained from the UV-visible spectrum at a wavelength of 415 nm. UV-visible spectroscopic studies during 38 days after the reaction process indicated a gradual disappearance in chlorophyll peak (437.5 nm) and appearance of new a peak at 403 nm due to the removal of chelated Mg²⁺ from porphyrin ring in chlorophyll due to the mild acidity of the medium. Resulted silver nanoparticles had an average size of 86 nm, which was examined through the Scanning Electron Microscopic (SEM) images. Microbial susceptibility to the Silver nanoparticles was studied for different concentrations of AgNO₃ through the well diffusion method and a highest inhibition zone was obtained for the *Riccia* sp. extract treated with 7 mM of AgNO₃.

Keywords: *Riccia* sp., silver nanoparticles, phytofabrication

INTRODUCTION

In the recent past, researches have paid much attention on silver nanoparticles due to its potential applications in various fields such as medical, electronics, chemical etc. [1-7]. Subsequently various chemical pathways have been developed for the fabrication of silver nanoparticles. However, most of the common chemical methods of nanoparticle synthesis such as reduction of solutions, thermal decomposition and biological reductions have adverse effects [8]. Therefore eco-friendly methods of silver nanoparticle fabrication needed to be introduced. Consequently, researchers have explored the use of plant materials for silver nanoparticles. Various plant species tested have yielded appreciable results. These synthesis techniques provide eco-friendly cost-effective methods, which do not require high temperature, pressure conditions, and toxic chemicals.

Flowering plants (Angiosperms) have successfully

been used in the synthesis of nanoparticles; *Medicago sativa* was the first reported plant used for green synthesis of silver and gold nanoparticles [9]. Since then many researchers have experimented different plant species for the synthesis of silver nanoparticles. Also it is confirmed that the stability of silver nanoparticles formed by plant-mediated synthesis is greater than that of the other methods [10]. As an example, *Magnolia kobus* forms excessively stable silver nanoparticles in the range of 15 – 500 nm. In various studies, it is found that the influence of amino groups, sulfhydryl groups and carboxylic groups are responsible for this silver nanoparticle formation. Also it is confirmed that the rate of formation depends on the reaction temperature and other physical properties [11, 12].

Bryophytes form the earliest diverging lineage of land plants and therefore hold the key position in land plant evolution. They show simple organization of the plant body (thallus) and comprise of three distinct morphological groups; liverworts (Phylum

Corresponding Author Email: *srubasinghe@pdn.ac.lk

Marchantiophyta), mosses (Phylum Bryophyta) and hornworts (Phylum Anthocerotophyta) [13]. Phytochemical studies carried out on these bryophytes have shown that they possess a variety of chemicals that can be used in various synthesis strategies [14]. However, only a few species of bryophytes have been tested on nanoparticles synthesis [15, 16].

In this article we explain a simple eco-friendly, one step process of biosynthesis of silver nanoparticles using *Riccia crispatula* Mitt. (Phylum Marchantiales, Class Ricciaceae) as the plant source. Characterizations of the fabricated silver nanoparticles have been carried out using UV- visible spectrometry, Scanning Electron Microscopy (SEM) and Energy Dispersive X-ray (EDX) analysis and Fourier Transform Infrared Spectroscopy (FTIR). Antibacterial activity of silver nanoparticles was studied using well diffusion method against human pathogenic bacterium *Pseudomonas aeruginosa*.

MATERIALS AND METHODS

Plant material and extraction process

Fresh thalli of *Riccia crispatula* were collected, and subsequent taxonomic identification was made by using taxonomic keys and descriptions [17]. Plant extractions were conducted by two different methods. In the first method, fresh mature thalli of the *R. crispatula* was cleaned using distilled water and air-dried. Then, 1 g of dried plant material was measured and crushed in 30 ml of 70% ethanol (99.9 (v/v), VWR Prolabo® Chemicals, EC). The extract obtained was filtered through coarse filter paper to obtain a clear extract and then it was diluted using 40 ml of 70% ethanol. In the second method, this procedure was repeated using absolute ethanol. Silver nanoparticle synthesizing procedure was carried out for both extracts separately.

Synthesis of nanoparticles

After preparing plant extracts, aqueous solutions of silver nitrate (AgNO_3 , 99.9%, RL Analytical Reagent, Sr. 1334) concentrations varying from 1- 10 mM were prepared. Then 1 ml of each AgNO_3 solution was added to 5 ml extract of the plant extract separately and kept at 25 °C on a shaker at 80 rev/min in dark, allowing the formation of silver nanoparticles.

Characterization of nanoparticles

UV-Visible Spectrophotometry

Optical absorption measurements of plant extracts were studied using normal incidence in the wavelength range 200 to 600 nm using UV-1800 Shimadzu single beam UV-vis spectrophotometer at 27 °C.

Scanning Electron Microscopy

Scanning electron microscopic (SEM) images of the fabricated silver nanoparticles were obtained using a Zeiss EVO LS 15 SEM. All the SEM images were taken at a tilt angle of 0° using an accelerating voltage of 20 keV.

Energy Dispersive X-ray Analysis

Energy dispersive X-ray analysis (EDX) was also obtained using Zeiss EVO LS 15 SEM.

Antibacterial activity

Antibacterial activity of the fabricated silver nanoparticles against human pathogenic bacterium *Pseudomonas aeruginosa* was examined using standard well diffusion method [18]. First, 10 g of nutrient agar was dissolved in 250 ml of distilled water in a conical flask, and kept in a sterilizer for 1 hour. Then the sterile nutrient agar solution was poured into sterile glass petri dishes and kept on the laminar floor at room temperature for solidification. Then 200 µl of fresh overnight grown pure cultures of the *Pseudomonas aeruginosa* was spread on nutrient agar using spreader. Then 3 wells (12 mm diameter, 50 mm apart from one another) were cut in the agar gel in one petri dish. After that solutions of synthesized silver nanoparticles were added into 2 wells and control solution (plant extract without silver nitrate) was added in to one well. The systems were incubated for 24 h at 37 °C, under aerobic conditions. After incubation, bacterial growth was observed, and area of inhibition was measured in mm.

RESULTS AND DISCUSSION

Reduction of Ag^+ ions in AgNO_3 to silver nanoparticles in *R. crispatula*. Extracts could be detected by a colour variation. Figure 1 (a) shows the colour of the pure extract (extreme left), and just after adding 1 to 10 mM of AgNO_3 to the extract (second

from left to extreme right respectively). As seen in Figure 1 (a), all the solutions including the pure extract look green initially. After three days, the colour was changed gradually for extracts treated with AgNO₃ concentrations beyond 3 mM, as seen in

Figure 1 (b). The colour variation from light-green to reddish-brown is an indication of the formation of silver nanoparticles. Silver nanoparticles exhibit a reddish-brown colour in aqueous solutions due to effects of surface plasmon resonance [19].

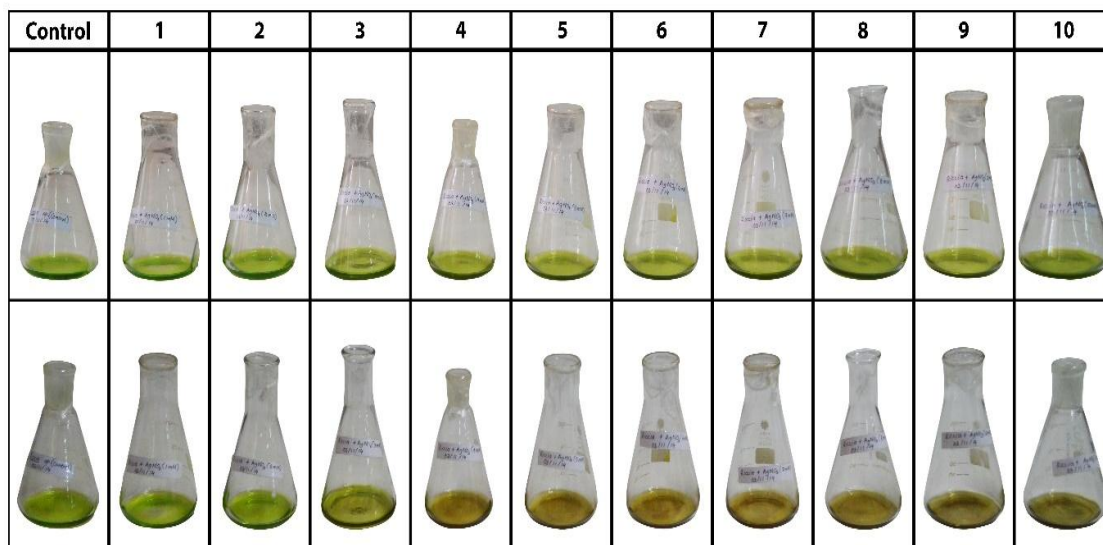


Figure 1. Color of solutions (a) immediately after and (b) 3 days after synthesis

The presence of silver nanoparticles was then studied using UV-visible spectrographs for extracts of *R.crispatula* treated with 1 – 10 mM of AgNO₃ (results not shown). Absorbance measurements were conducted in the range 200 to 600 nm and the results revealed that the optimum concentration to synthesize silver nanoparticles is 7 mM.

The UV-visible spectrographs taken at different time intervals from immediately after, to 38 days after, for the extract treated with 7 mM AgNO₃ are shown in Figure 2. There are two absorption regions available

for chlorophylls, the most common plant pigments in plants, which are at about 430 nm and 660 nm for chlorophyll a and 453 nm and 643 nm for chlorophyll b. Chlorophyll a, which is located in the PS II system plants give maximum absorption around 437 nm [20]. Hence the peak at 437.5 nm in Figure 2 was identified as chlorophyll a. The peak at 415 nm corresponds to formed silver nanoparticles.

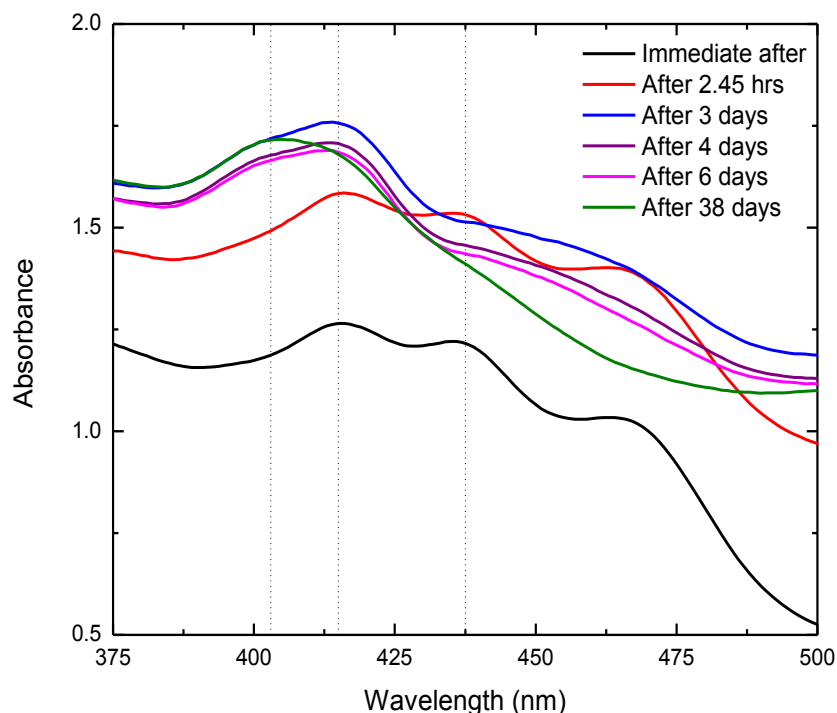


Figure 2. UV-visible spectrographs for *Riccia sp.* treated with 7 mM AgNO_3 at different time intervals

According to the UV-vis spectrographs, the intensity of the silver peak at 415 nm intensified compared to the chlorophyll peak at 437.5 nm over the course of time, suggesting the existence and potential increment in the concentration of silver nanoparticles in the solution. In addition, the chlorophyll peak seems to disappear after 38 days, while a new peak emerge at 403 nm in the spectrum.

In order to investigate this new peak at 403 nm a separate test was conducted for the *R. crispatula* extracts using two different extraction solvents; absolute ethanol and 70% ethanol. UV-visible spectrographs were taken immediately after and 38 days after to investigate any potential variations in the characteristic absorbance peaks of the solutions over the course of time.

The obtained results for the test are shown in Figure 3. Figure 3 (a) shows the UV-visible spectrographs obtained using 70% ethanolic plant extract and Figure

3 (b) using absolute ethanol for both immediately after (red line) and 38 days after (black line). While there is no significant alteration of the chlorophyll peak at 437.5 nm for the case of absolute ethanol extract (Fig. 3b), the 70% ethanolic extract (Figure 3a) shows clear indication of disappearance of the chlorophyll peak and a new broad peak emerging at about 403 nm.

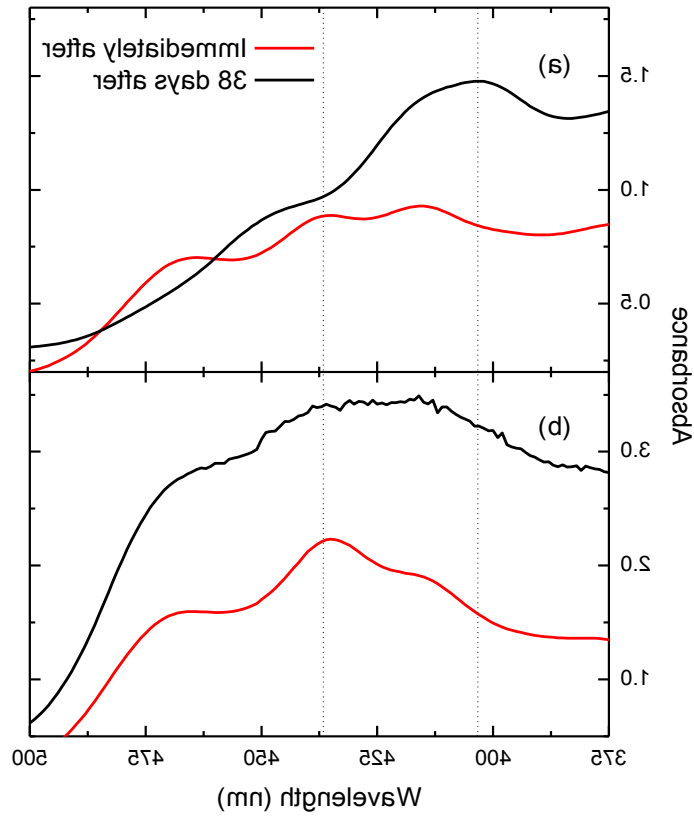


Figure 3. UV-visible spectrographs of plant extracts using 70% ethanol as the solvent (a) and using absolute ethanol as the solvent (b)

The 70% ethanolic plant extract is more acidic than absolute ethanol plant extract. The pH measurements revealed a pH value of 4.8 for 70% ethanolic extract and 6.5 for the absolute extract. When chlorophyll is treated with an acid, it removes a chelated Mg^{2+} ion from the porphyrin ring of chlorophyll, and subsequently Mg^{2+} in chlorophyll is replaced with two hydrogen atoms as shown in Figure 4. The non-

chelated porphyrin ring gives a peak around 400-405 nm for the UV-vis spectrum. Therefore, this could be the reason for the newly emerged peak when 70% ethanol used as the solvent and hence the broad peak in Figure 2 after 38 days.

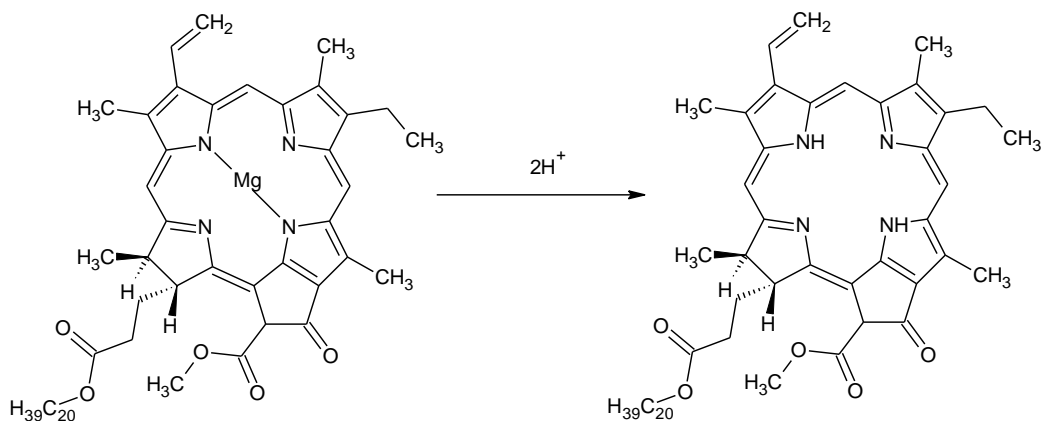


Figure 4. Schematic representation of the conversion of chlorophyll a to pheophytin a through acid hydrolysis [21]

In order to observe the fabricated silver nanoparticles, an SEM image was taken after depositing 7 mM AgNO₃ treated *Riccia* sp. extract on a carbon strip. Figure 5 shows the SEM image of the silver nanoparticles obtained under a magnification of ×81,000. The bright spherical structures suggest the presence of silver nanoparticles. The size of nanoparticles was approximated to be about 86 nm (Figure 6).

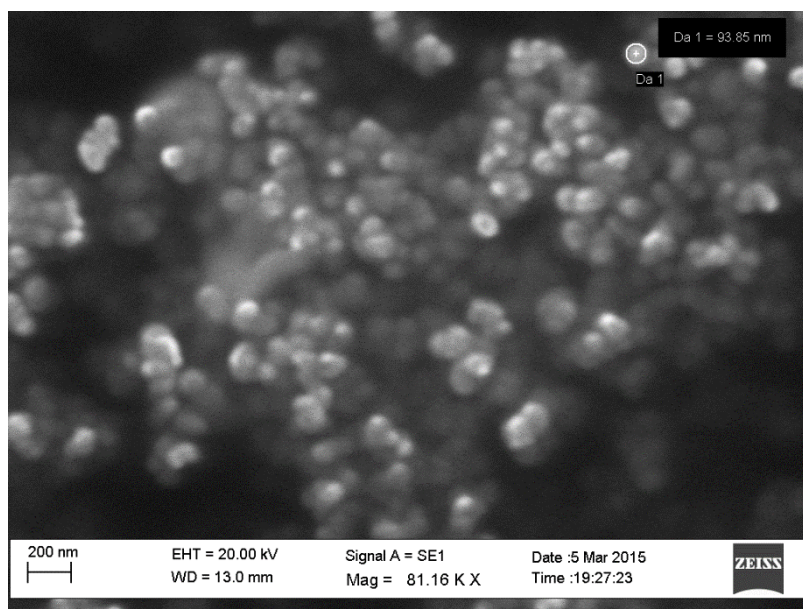
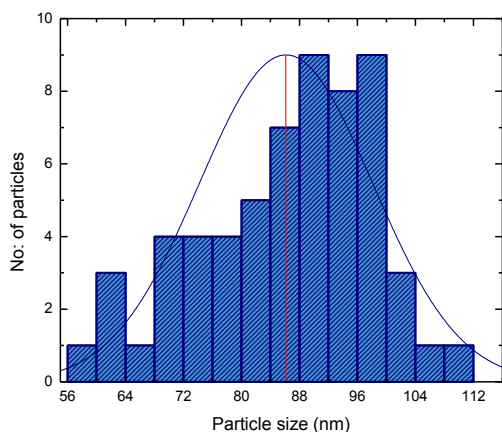


Figure 5. SEM image of synthesized silver nanoparticles



The presence of silver nanoparticles was further confirmed by an EDX spectrum. The result obtained is shown in Figure 7. The strong signals resulting from silver atoms in the nanoparticles further confirms the reduction of silver ions into elemental silver and hence the formation of silver nanoparticles.

Figure 6. Size distribution of the silver nanoparticles

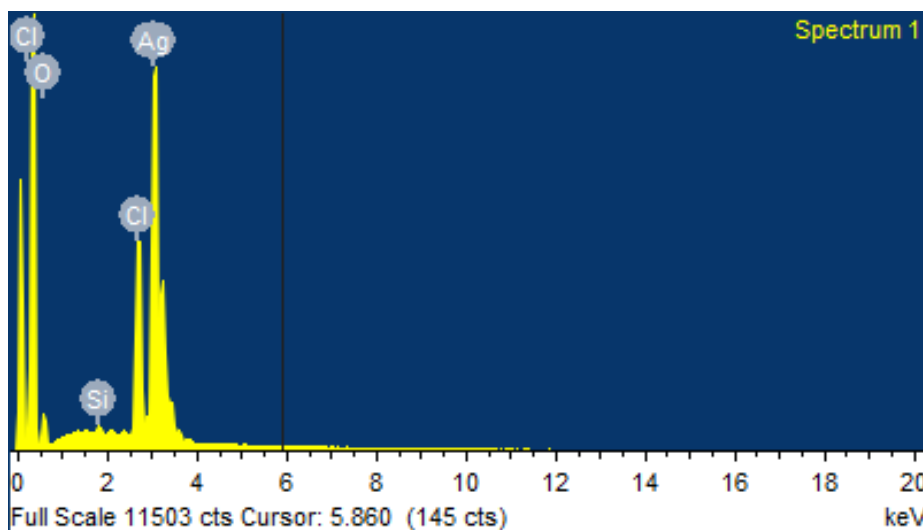


Figure 7. EDX spectrum of silver nanoparticles

The antibacterial activity of silver nanoparticles was assessed using a bioassay through the well diffusion method [22]. Silver nanoparticles synthesized from 5 – 9 mM of AgNO₃ along with the pure *Riccia* sp. extract were individually subjected to the test to obtain the zonal inhibitions. During the experiment a large number of *P. aeruginosa* cells from a single strain were spread over the agar, and then incubated in the presence of silver nanoparticle solution for a period of 24 hours. Figure 8 shows the result obtained by using nanoparticles extracted using 7 and 8 mM AgNO₃ and the pure extract. It is expected to visually identify the zones of inhibition in the agar plate if the

applied bacterial strain is susceptible to the silver nanoparticles. The experiment resulted clear zones of inhibition against *P. aeruginosa* as seen in the figure. The measured values of the zones of inhibition with respect to the different concentrations of AgNO₃ are shown in Figure 9.

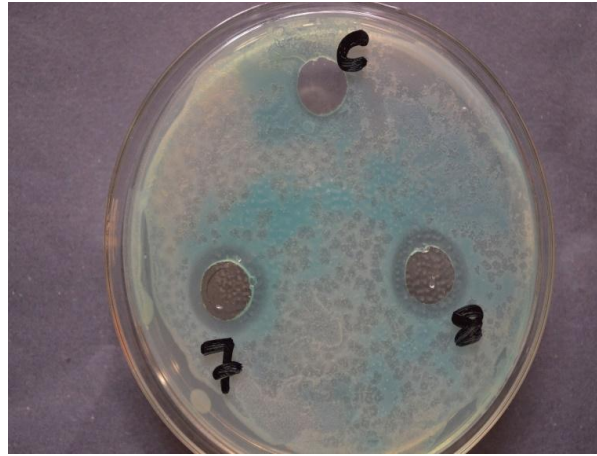


Figure 5: Zonal inhibition of silver nanoparticles against *Pseudomonas aeruginosa* with 7 mM and 8 mM AgNO_3 treated extract with respect to control solution

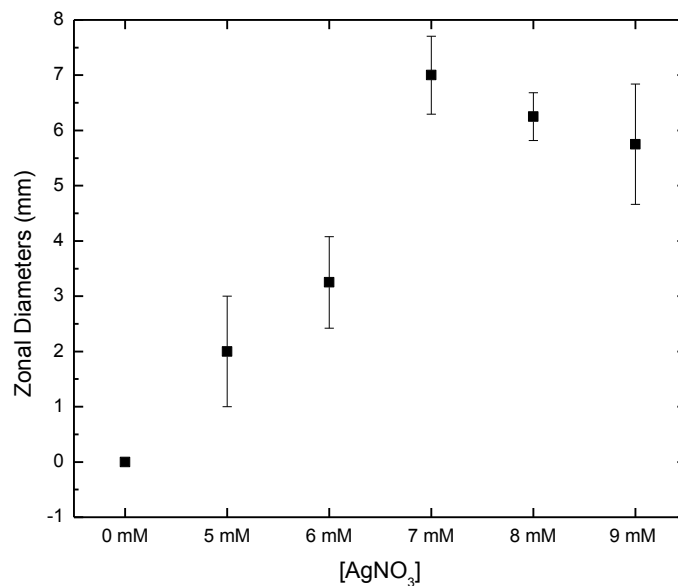


Figure 6. Size distribution of zonal inhibitions against *Pseudomonas aeruginosa*

According to the measured zonal diameters, 7 mM of AgNO_3 resulted highest diameter and hence higher antibacterial activity with respect to other concentrations. It is believed that the antibacterial activity of silver nanoparticles is a result of its interference with respiratory metabolism of bacterial organisms and subsequent destruction [1, 23]. These evidences prove the possibility in formation of Ag

NPs by environmental friendly method using bryophytes.

CONCLUSION

In conclusion, the ability of the thalloid liverwort *Riccia* sp. for fabricating Ag nanoparticles was determined using various experimental techniques. A

peak for pure silver nanoparticles was identified at 415 nm from the UV-visible spectrographs. After 38 days the reaction process a gradual disappearance in peak at 437.5 nm, and appearance of new peak at 403 nm was observed. This was identified due to the removal of chelated Mg²⁺ from porphyrin ring in chlorophyll, which occurs in the mild acidic medium. EDX was used to confirm the presence of elemental silver. Resulted silver nanoparticles had an average size of 86 nm which was examined through the SEM imaging. Furthermore, microbial susceptibility to the silver nanoparticles for *Pseudomonas aeruginosa* was studied for all concentrations of AgNO₃, through the well diffusion method and highest inhibition zone was obtained for 7 mM of AgNO₃.

ACKNOWLEDGEMENT

Support by the academic and technical staff of the departments of Physics, Botany and the Postgraduate Institute of Science, University of Peradeniya are highly appreciated.

REFERENCES

- Tran, Q. H., Nguyen, V. Q., & Le, A. T. (2013). Silver nanoparticles: synthesis, properties, toxicology, applications and perspectives Adv. Nat.,Sci: Nanosci. Nanotechnol, 4, 1-20.
- Ju-Nam, Y., & Lead, J. R. (2008). Manufactured nanoparticles: An overview of their chemistry, interactions and potential environmental implications, Science of The Total Environment, 400, 369- 414.
- Sharma, V. K., Yngard, R. A., & Lin, Y. (2009). Silver nanoparticles: Green synthesis and their antimicrobial activities, Adv. Colloid Sur. Interface, 145, 83- 96.
- Krutuyakov, Y. A., Kudrynskiy, A. A., Olenin, A. Y., & Lisichkin, G. V. (2011). Antimicrobial activity of Silver Nanoparticles synthesized by using Medicinal Plants, International Journal of ChemTech Research, 3, 1394-1402.
- De, M., Ghosh, P. S., & Rotello, V. M. (2008). Applications of Nanoparticles in Biology, Advanced Materials, 20, 4225-4241.
- Lu, A. H., Salabas, E. L., & Ferdi, S. (2007). Magnetic Nanoparticles: Synthesis, Protection, Functionalization, and Application, Angew. Chem. Int. Ed, 46, 1222-1244.
- Chaudhuri, R. G., & Paria, S. (2012). Core/Shell Nanoparticles: Classes, Properties, Synthesis Mechanisms, Characterization, and Applications, Chem. Rev, 112, 2373-2433.
- Afreen, Rathod, V., & Ranganath, E. (2011). Synthesis of monodispersed silver nanoparticles by Rhizopus Stolonifera and its antibacterial activity against MDR strains of Pseudomonas Aeruginosa from burnt patients, International Journal of Environmental Sciences, 1(7),
- Gardea-Torresdey, J. L., Gomez, E., Peralta-Videa, J. R., Parsons, J. G., Troiani, H., & Jose-Yacamán, M. (2003). Alfalfa sprouts: A natural source for the synthesis of silver nanoparticles. Langmuir, 19, 1357-1361.
- Baker, S., Rakshith, D., Kavitha, K. S., Santosh, P., Kavitha, H. U., Rao, Y., & Satish, S. (2013). Plants: Emerging as nanofactories towards facial route in synthesis of nanoparticles, Bioimpacts, 3(3), 111-117.
- Song, J. Y., & Kim, B. S. (2008). Biological synthesis of bimetallic Au/Ag nanoparticles using Persimmon (Diopyros kaki) leaf extract. Korean J ChemEng, 25, 808-811.
- Baker, S., Rakshith, D., Kavitha, K. S., Santosh, P., Kavitha, H. U., Rao, Y., & Satish, S. (2013). Plants, 3, 111-117.
- Kim, J. S., & Kuk, E. (2007). Antimicrobial effects of silver nanoparticles, Nanomedicine, 3, 95-101.
- Yasin, S., Liu, L., & Yao, J. (2013). Biosynthesis of Silver Nanoparticles by Bamboo Leaves Extract and Their Antimicrobial Activity, Journal of Fiber Bioengineering and Informatics, 6(1), 77-84.
- Kulkarni, A. P., Srivastava, A. A., Harpale, P. M., & Zunjarrao, R. S. (2011). Plant mediated synthesis of silver nanoparticles-tapping the unexploited sources, J of Natural Product and Plant Resources, 4, 100-107.
- Kulkarni, A. P., Srivastava, A. A., Nagalgaon, R. K., & Zunjarrao, R. S. (2012). Phytofabrication of silver nanoparticles from a novel plant source and its application, International J of Biological and Pharmaceutical Research, 3, 417-421.
- Sing, S. K., Bag, A. K., & Bhattacharya, S. G. (2010). Riccia (hepaticae :ricciaceae) of west Bengal. Taiwan, 55.
- Sen, A., & Batra, A. (2012). Evaluation of Antimicrobial Activity of Different Solvent Extracts of Medicinal Plant: *Melia Azedarach*, International Journal of Current Pharmaceutical Research, 4, 67- 73.
- Zielinska, A., Skwarek, E., Zaleska, A., Gazdac, M., & Hupka J. (2009). Preparation of silver nanoparticles with controlled particle size, j.proche., 1, 1560-1566.
- Munns, R., Schmidt, S., & Beveridge, C. (2010). Chlorophyll absorption and photosynthetic action spectra, Plants in Action, (2).
- Joslyn, M. A., & Mackinney, G. (1938). The Rate of Conversion of Chlorophyll to Pheophytin, J. Am. Chem. Soc., 5, 1132-1136.
- Magaldi, S., et al. (2004). Well diffusion for antifungal susceptibility testing, International Journal of Infectious Diseases, 8, 39- 45
- Le, A. T., et al. (2011). Novel silver nanoparticles: synthesis, properties and applications, International Journal of Nanotechnology (IJNT), 8, 1- 20.
- Basavaraja, S., Balaji, S. D., Arunkumar, L., Rajasab, A. H., & Venkataraman, A. (2008). Extracellular biosynthesis of silver nanoparticles using the fungus Fusarium semitectum, Materials Research Bulletin, 43, 164-1170.
- David, D., Evanoff, J. R., & Chumanov, G. (2005). Synthesis and Optical Properties of Silver Nanoparticles and Arrays, ChemPhysChem, 6, 1221-1231.

Jones, C. M., & Hoek, E. M. (2010). A review of the antibacterial effects of silver nanomaterials and potential implications for human health and the environment, *J. Nanopart. Res.*, 12, 1531-1551.

Sotiriou, G. A., & Pratsinis, S. E. (2010). Antibacterial Activity of Nanosilver Ions and Particles, *Environ SciTechnol*, 44, 5649-5654.

Taiz, L., & Zeiger, E. (2003). *Plant Physiology*, (3), 179-191.

<http://www.ch.ic.ac.uk/local/projects/steer/chloro.htm> (sited on 16-05-2015).

FACILE SYNTHESIS OF HYDROXYAPATITE/ IRON OXIDE NANOCOMPOSITE TO BE USED AS A DRUG CARRIER

Manatunga, D.C¹, De Silva, W.R.M^{2,*} and De Silva, K.M.N³

^{1,2} Department of Chemistry, University of Colombo

³ Sri Lanka Institute of Nanotechnology, Nanotechnology & Science Park, Mahenwatte, Pitipana, Homagama, Sri Lanka

Abstract

Hydroxyapatite (HAp) is an inorganic calcium phosphate ceramic which has been widely used for many biological applications like bone tissue engineering, bone reconstruction and in drug delivery because of its known biocompatibility and biodegradability. In most of the reported work the synthesized hydroxyapatite nanoparticles had a nanocrystalline nature with a needle shape. However this study has involved the facile creation of low crystalline HAp as an alternative to these methods. Moreover a magnetic core of iron oxide nanoparticles (IONPs) has coupled to this system in order to increase the targeted delivery by using an external magnetic field. The formation of HAp coated on IONPs was evident from Scanning electron micrographs (SEM), Fourier Transform Infra-red spectroscopy (FT-IR) and X-ray diffraction (XRD) studies. Later this composite was used to study the drug encapsulation efficiency using paracetamol as a model drug. Several systems having different degree of crystallinity were studied for their capability to bind with the drug molecules out of which one system has been identified as the best system, having an encapsulation efficiency of 95%. This system has highlighted its ability to perform slow releasing property of paracetamol in both pH 7.4 and pH 5.5 buffer systems. Therefore the main objective of this work was identify a potential drug delivery agent for the purpose of targeted and controlled delivery of drug molecules which could be used for the purpose of cancer drug delivery.

Keywords: Hydroxyapatite, Iron oxide, drug-carrier, magnetic, controlled, targeted

INTRODUCTION

Functionalization of nanomaterials via a chemical or biological moiety will anchor some additional properties for these nanomaterials which could extend its application in many fields. However when these nanomaterials are being utilized in biomedical applications, the main issue that has limited their application is the biocompatibility [1]. Therefore much attention has been devoted in recent years to tackle this problem by providing a surface modification to those bear nanomaterials, which could prevent aggregation and possible removal of them by the immune system. Among the well-known inorganic nanomaterials, iron oxide nanoparticles (IONPs) have been widely consumed for several biomedical applications such as magnetic resonance imaging (MRI), hyperthermia, magnetofection, cell

separation, drug delivery etc [1-7]. For these applications the surface of IONPs has been modified with the use of polymer coatings [4-6] or inorganic coatings [4,6], mainly to avoid the risk of elimination by the reticular endothelium system (RES) prior to reaching the targeted site [5] and to increase the stability [5,6]. This is because the fate of these nanoparticles are highly dependent on the size, morphology and the surface chemistry of the nanoparticles [1].

There are number of reports where polymer and inorganic coatings have been used to functionalize the IONPs where IONPs have acted as the core and the respective coatings giving rise to a shell like structure. Use of (poly D, L/lactide-co-glycolide acid-PLGA) [4,8], carboxymethyl cellulose (CMC) [9], dextran [4], polyethylene glycol (PEG) [4] as

polymers and silica [4,6], hydroxyapatite (HAp) [2-5,7,10], Al₂O₃ [1] as inorganic materials are among the reported work. The main intention behind the use of magnetic core shell structures is the possibility of manipulating them using an external magnetic field which could in-turn trigger the release of bioactive molecules [6] that are bound to these carriers or to improve the efficacy of a particular application by coupling in to a magnetic field (e.g. protein separation [11], transfection [12] and heavy metal removal [13]).

Recently it has been identified that inorganic coatings have much capability to withstand the in-vivo harsh environments rather than the polymer coatings [5]. Among the use of core shell inorganic hybrids of IONPs, the use of hydroxyapatite (HAp) as a coating has gained much considerable attention over the last few years, because of the unique features provided by HAp. Hydroxyapatite is a naturally available calcium phosphate form [4,10] which accounts for the main mineral component in hard tissues (bone and teeth) [4,14-19]. It possessed a good biocompatibility and biodegradability [5,10,12,17,19] which has extended its application widely in biomedical field [11,19] specially in osseoregeneration [18], bone implantation [4], drug delivery [4], gene delivery [12] and in many other applications [19]. There are number of studies which involve in the preparation of HAp with various shapes like nanorods, needles, nanospheres etc [19-23]. Moreover due to its crystalline structure and the adsorption capability it has made it possible for different modifications like substitution, doping which has tailored additional properties on to HAp [14]. However the synthesis of HAp/IONPs is a novel concept where much work is not reported in this particular area [2,5,14].

In this situation, the development of HAp/IONPs composites can be identified as a novel tool, which can be utilized for bone tissue engineering [6,24] which will enhance the bone cell regeneration, hyperthermia application [6] and also it could be loaded with biomolecules like drugs [6], growth factors [7] which can be delivered to the area of interest like cancer cells in a controlled and a targeted manner using an external magnetic field. The major problem in common cancer treatment protocols is the non-specificity and the damage caused to normal and healthy tissues. This could be avoided by using

biocompatible HAp/IONP composites which could provide more direct and effective treatment protocol [1,7].

According to the reported work in this area [2,5,14,19,25], it is clear that obtaining a facile synthetic approach for the synthesis of HAp/IONPs is still remained to be a challenge where only few were based on ultrasonication irradiation [2], ultrasonic spray pyrolysis at high temperature [26], coprecipitation [14,27,28], hydrothermal synthesis [15], mechanochemical synthesis [10] and microwave irradiated synthesis [19]. More importantly these methods are labor intensive, expensive, require lengthy processing time (several hours to days) [3,5,6,11,12,14,27,28] high temperature treatment [15,19,24,26], calcination [11], freeze drying [4,6] which makes it energy and time consuming [14].

In our present work, we have attempted to follow a facile synthetic approach to obtain HAp coated IONPs where it has avoided many of the energy and time requiring steps so far reported. A basic coprecipitation technique has been utilized without using calcination or freeze drying at the end. As synthesized HAp/IONPs composites were used to load a model drug to check the encapsulation efficiency. The best system based on the encapsulation efficiency was subjected to in-vitro controlled release assessment in two buffer media. This work highlights the possibility of synthesizing HAp/IONP nanocomposites via a simple and a rapid approach which can be used for the purpose of targeted and controlled delivery of drugs, specially for the treatment of cancer.

METHOD

Materials

All chemicals were reagent grade and used without further purification. Ferrous ammonium sulfate hexahydrate ((NH₄)₂Fe(SO₄)₂·6H₂O, 99%), ferric ammonium sulfate dodecahydrate ((NH₄)₂Fe(SO₄)₂·12H₂O, 99%), ammonium hydroxide (NH₄OH, 25%), Ca(NO₃)₂·4H₂O (99%), (NH₄)₂HPO₄ (≥ 99%), MgCl₂·6H₂O (99-102%), sodium alginate (low viscosity, NaAlg), carboxymethyl cellulose sodium salt (low viscosity, CMC) were purchased from Sigma Aldrich. Double distilled degassed water

was used throughout the experiment. Paracetamol (99.3 %) was kindly donated by the State Pharmaceuticals (SPMC) of Sri Lanka.

Preparation of HAp/IONP composites

Synthesis of iron oxide nanoparticles (IONP)

Magnetite (Fe₃O₄) nanoparticles were prepared using the co-precipitation technique. Briefly ferric and ferrous aqueous ion solutions were mixed in 2:1 molar ratio under an inert atmosphere to which ammonia was added in dropwise manner. Vigorous stirring was carried out till a black colored suspension was obtained. These IONPs were magnetically separated, washed and used for the creation of HAp/IONP composites.

Synthesis of CMC added HAp/IONP composite (S1)

Hydroxyapatite coating was created on IONPs by simply adding an alkaline solution of Ca(NO₃)₂ to the IONPs dispersion containing (NH₄)₂HPO₄ and carboxymethyl cellulose. Vigorous stirring was allowed at low temperature while adjusting the pH at 8-9. Stirring was continued for several hours and the magnetic separation was carried out at the end. The obtained brown black product was washed thoroughly till the pH becomes neutral.

Synthesis of Mg doped HAp/IONP composite (S2)

Synthesis of S2 was performed in the same manner following the procedure in S1 except the step where CMC has been added. Instead IONPs were mixed with MgCl₂ and phosphate precursor prior to the addition of the calcium precursor.

Synthesis of NaAlg added HAp/IONPs (S3)

For the synthesis of S3 the same procedure in S1 and S2 was followed by replacing CMC/Mg²⁺ with the addition of NaAlg as a polymer to the IONP suspension containing the phosphate precursor.

Material Characterization

X-ray powder diffraction pattern (PXRD) was recorded using Bruker D8 Focus X-ray Diffractometer with CuK α radiation ($\lambda = 1.5418 \text{ \AA}$) over the range of 5°-8°. Fourier Transform Infra-Red (FT-IR) spectroscopy was performed with a spectrometer (Bruker Vertex 80) over the range of 400-4000 cm⁻¹ with the KBr pellet technique. To characterize the size and the shape of the neat IONPs, a drop of the IONP suspension was placed on a copper grid and the image was obtained by Transmission Electron Microscope (TEM-JOEL JEM 1011) operating at an accelerating voltage of 100 kV. Morphology of the magnetic HAp composite was examined by the Scanning Electron Microscope (SEM- SU 6600, Hitachi) operating at 10 kV. The elemental analysis of the HAp/IONP composites was analyzed by the X-Ray Fluorescence Microscope (XGT-5200, Horiba). Thermal degradation pattern of each composite was obtained by the Thermogravimetric analysis (TGA), which was performed by Thermogravimetric Analyzer (SGT Q 600) where the samples were heated from room temperature to 1000 °C. Finally the Ca and Fe leaching from the composites were analyzed from the liquor collected at the end by subjecting in to atomic absorption spectroscopy (AAS- Hitachi 2-8100, spectrophotometer).

In-vitro drug loading and releasing studies

Paracetamol was used a model drug in this study. Paracetamol adsorption study was carried out by adding a constant amount of drug to a varying amount of composite from each system and incubating for 17 hours at 37 °C at 180 rpm. The maximum loading was assessed by measuring the remaining amount of paracetamol in the suspension. All the experiments were based on the UV absorption measurement of paracetamol at 244 nm (λ_{max}). With respect to the amount that has been loaded in to the each system, the encapsulation efficiency was calculated.

$$\text{Encapsulation efficiency} = \frac{\text{Initial drug concentration} - \text{Remaining drug concentration}}{\text{Initial drug concentration}} \times 100 \%$$

The best system out of S1, S2, and S3 was selected as the one which is showing the highest encapsulation efficiency. That particular system was further analyzed for its ability to do controlled releasing over a period of time. The drug loaded HAp/IONP composite was of 100 mg was immersed in 10 ml of PBS (ph 7.4) at 37°C with a constant shaking at 80 rpm. At each time interval 1 ml of the release medium was withdrawn for UV Vis analysis at 244 nm and the medium was replaced with a same amount of the fresh buffer.

Similarly another releasing study was carried out in a lower pH buffer (pH 5.5, acetate buffer). Rest of the procedure was same as in the case of releasing study done in PBS buffer.

Statistical Analysis

All data were expressed as mean (\pm) SD, and were analyzed by analysis of variance (one-way ANOVA). Statistical significance was accepted at a level of $p < 0.05$.

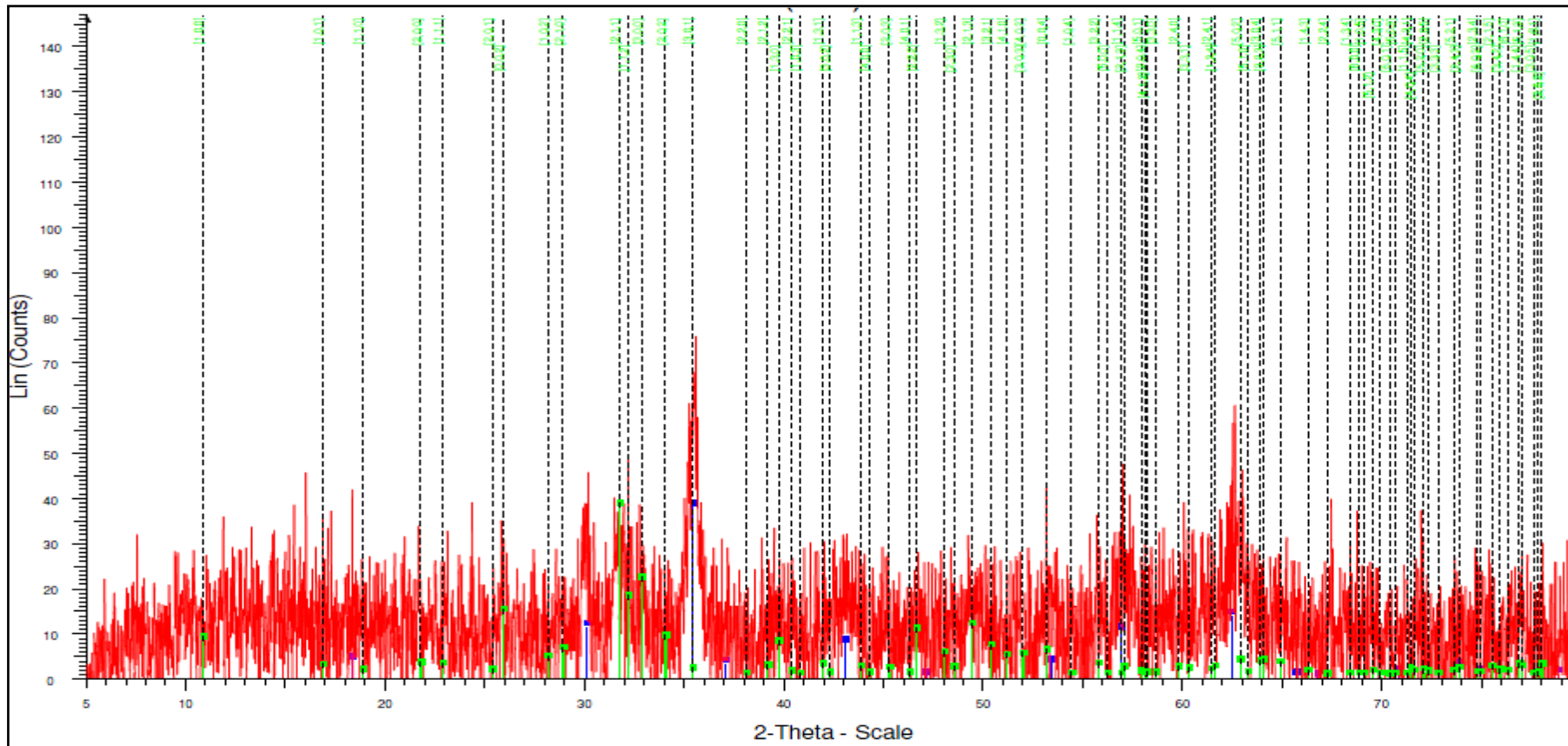
RESULTS

X-Ray Diffraction studies of HAp/IONP composites

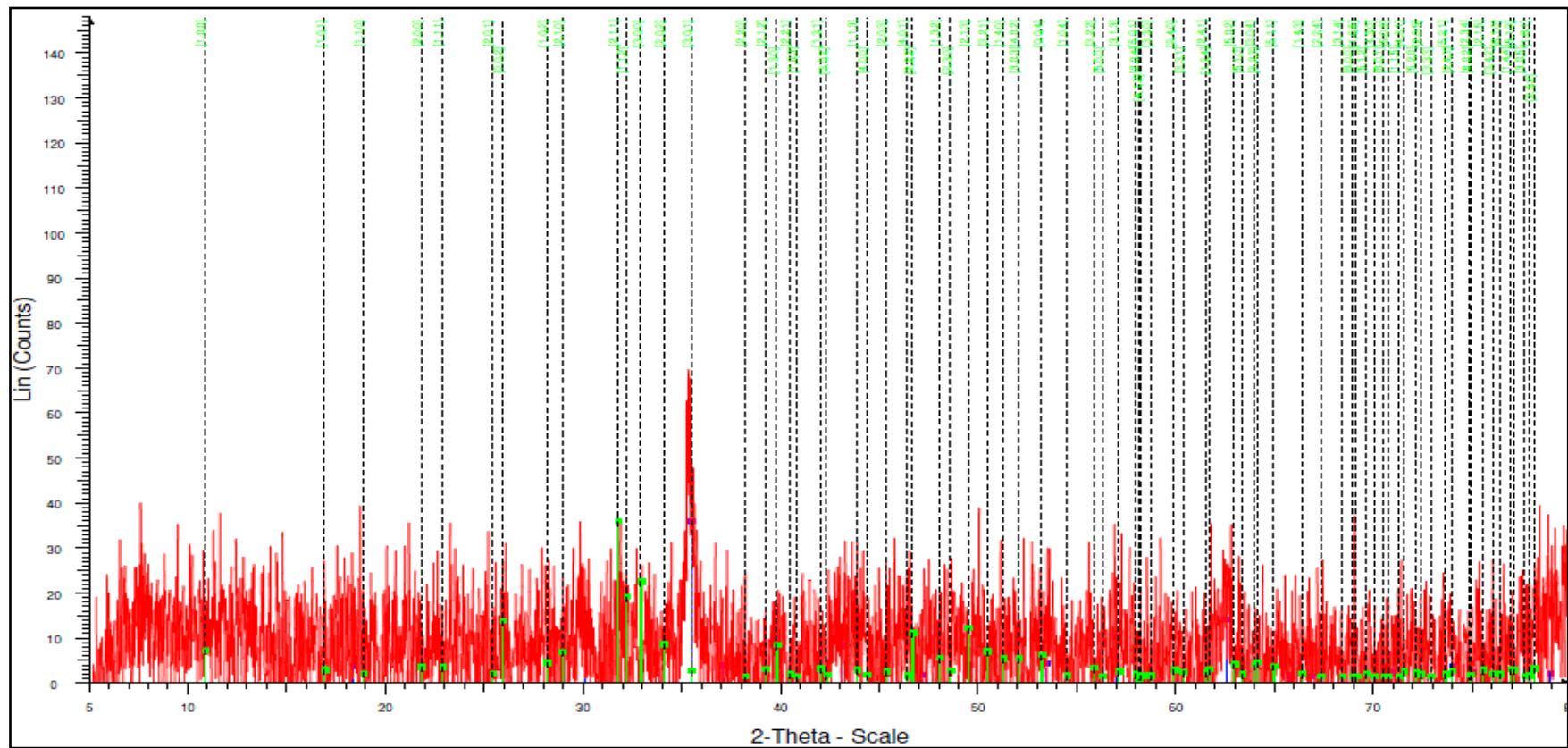
The XRD pattern of magnetite (Supplementary Information, Fig. S1) and HAp (Supplementary Information, Fig. S2.a,b) were in accordance with the reported XRD patterns [12,13,17,19] except in the case where Mg^{2+} doping has been carried out (Supplementary Information, Fig. S2.c). This system has given rise to very low crystalline HAp which is evidenced with the low intense Sand broad peaks in the XRD pattern. In general the HAp samples corresponding to S1,S2 and S3 has resulted with peak broadening which has highlighted the low crystalline or small crystallite size of the HAp [7].

The PXRD patterns of the magnetic HAp nanoparticles of each system synthesized by the coprecipitation method are given in Fig.1. a,b,c. All of these patterns were more similar to the diffraction pattern of magnetite with much broader peaks. This type of an observation is in accordance with the reported work [6,13,14,29]. Also the intensity of the HAp was very low and only few peaks were appearing in the region of 2θ 30-35°, which depicted the presence of HAp. However this type of a pattern can be expected as the crystalline magnetite nanoparticles with high intensity in its XRD pattern might have masked the appearance of the low crystalline HAp that is being coated on the IONP surface. Moreover a low concentration of HAp was used as a coating on IONPs that will again minimize the appearance of HAp peaks over the more prominent IONP peaks.

a)



b.)



c.)

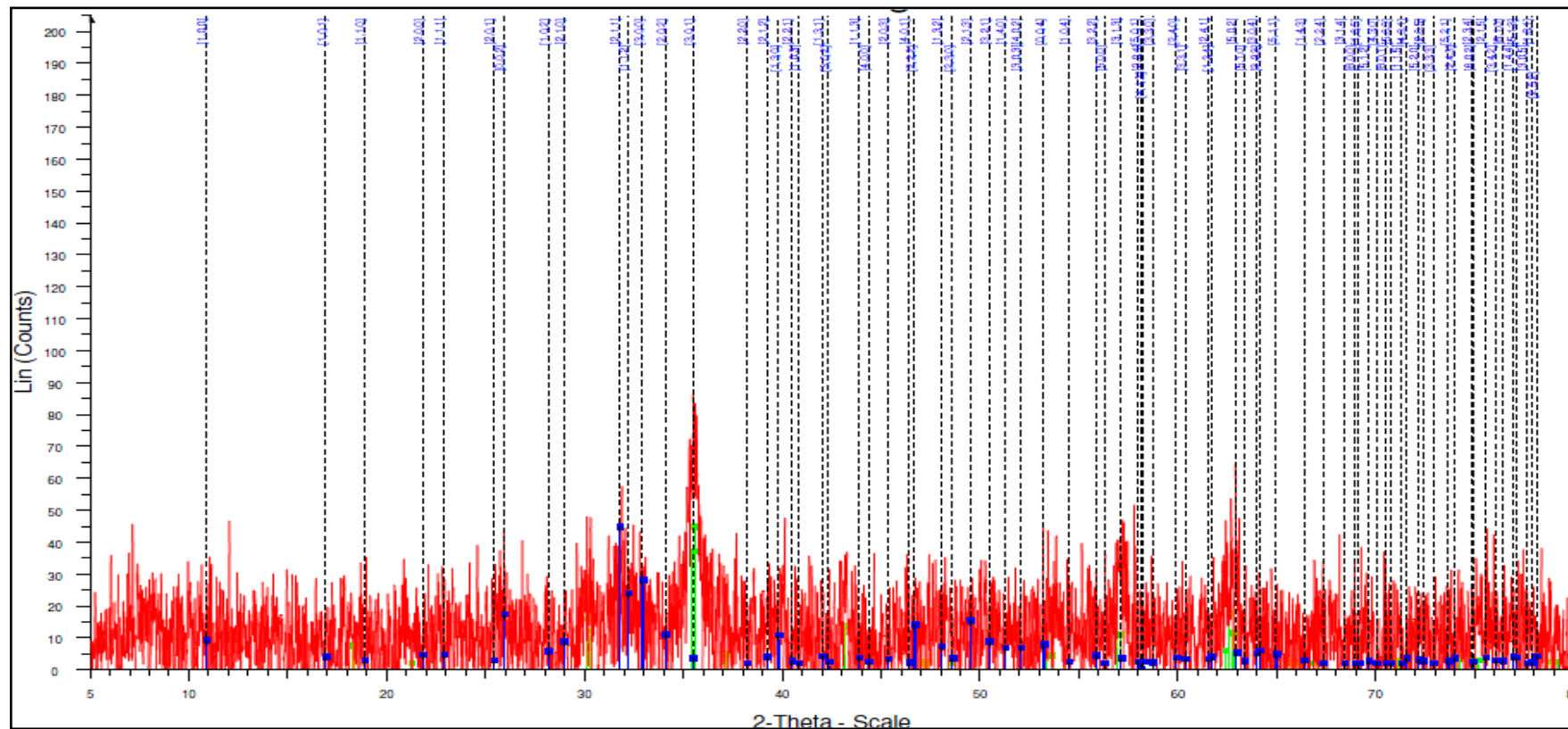


Figure. 1. a. PXRD pattern of HAp/IONPs (S1), HAp/IONPs (S2), HAp/IONPs (S3)

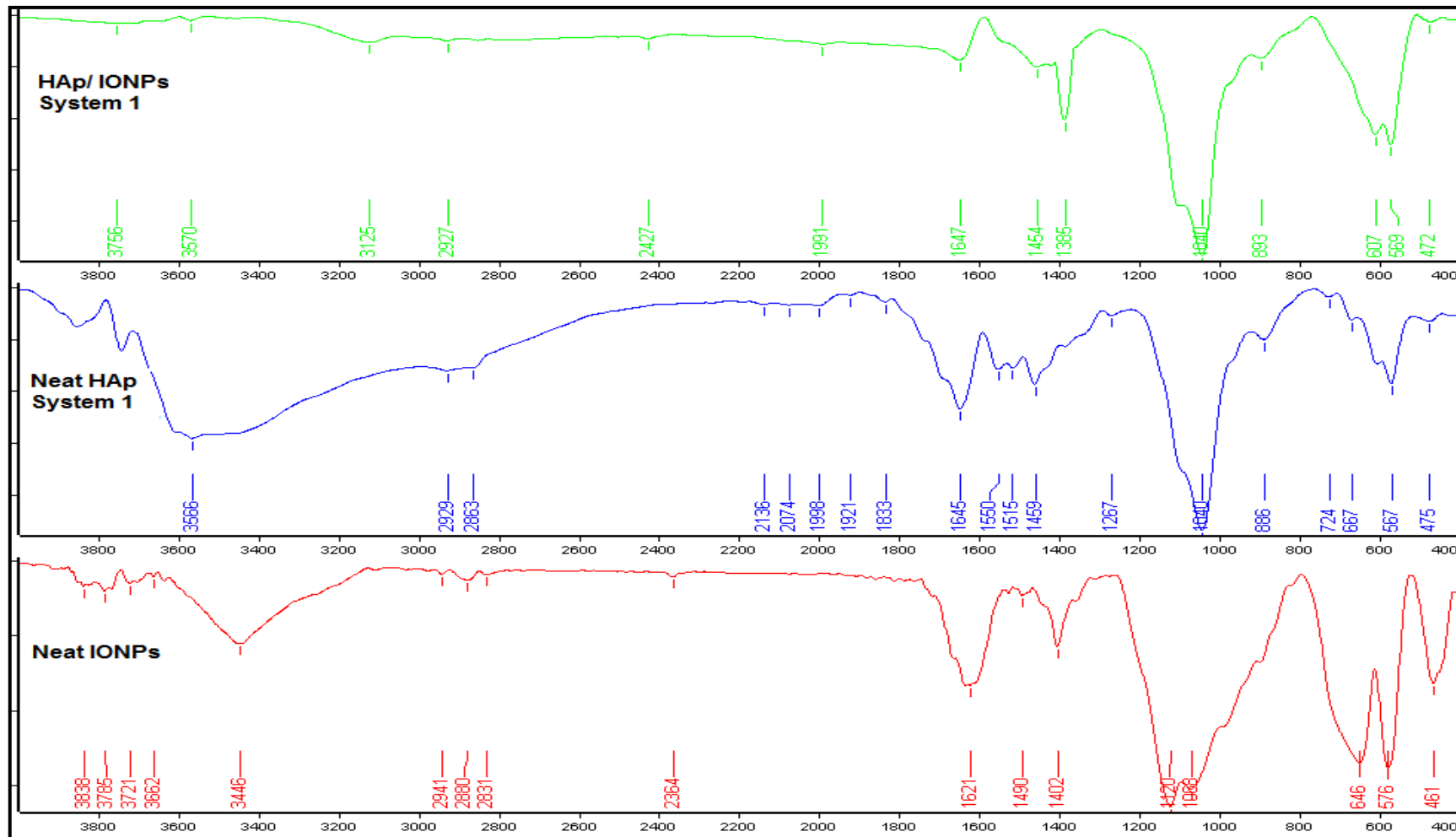
Fourier Transform Infra-red spectroscopy of HAp/IONP composites

The infra-red vibrational bands of magnetic HAp systems are shown in Fig.2 and summarized in the table 1 (Supplementary Information).

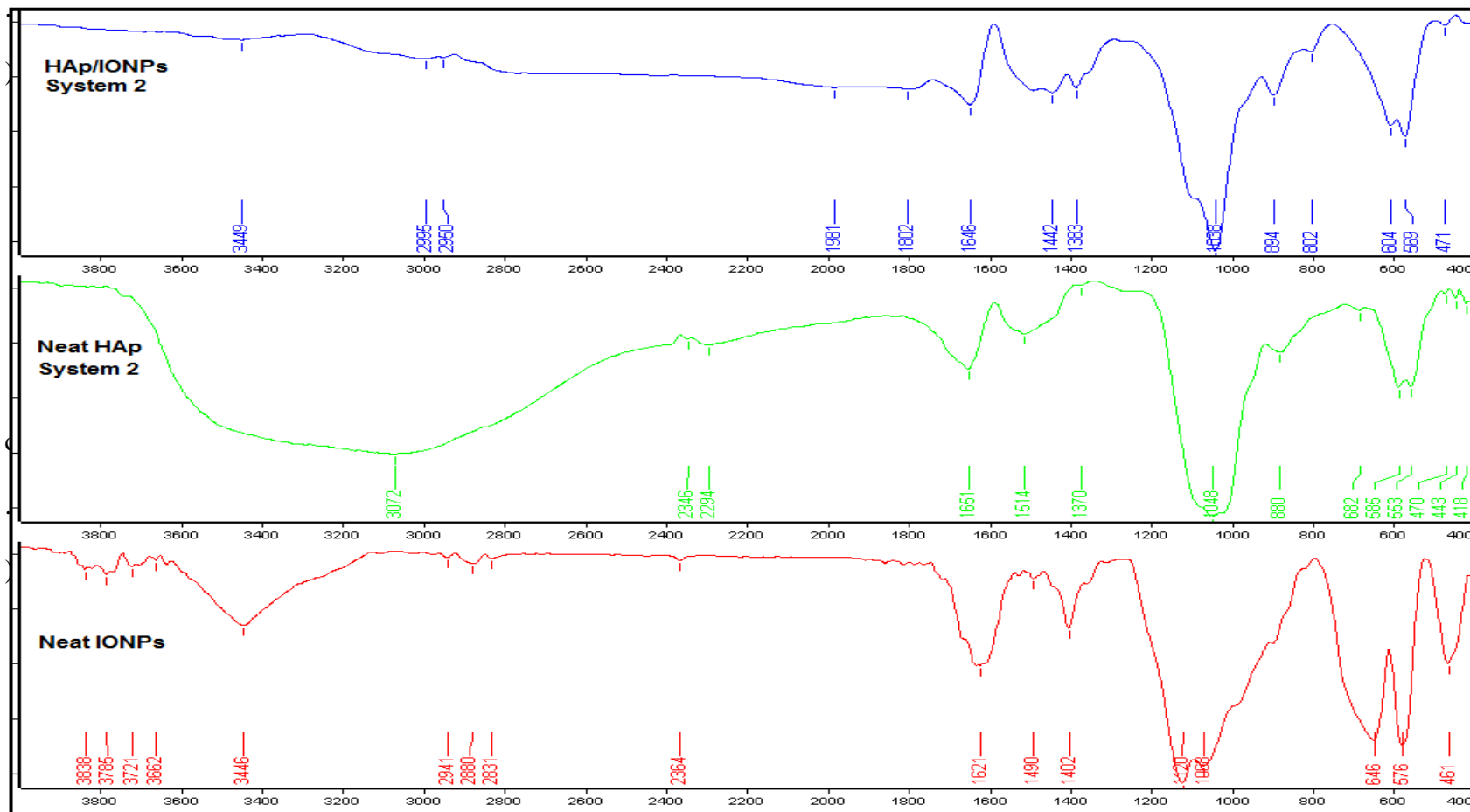
Table 1: Vibrational bands of HAp/ IONP composites

Type of vibration	Wave number (cm-1)
Fe-O	576 [3,5,14]
PO ₃ ⁴⁻ stretching	471, 961,1040,1090 [3,14]
PO ₃ ⁴⁻ bending	567, 606 [3,14]
Apatite –OH	3572,633 [3,14]
Adsorbed –OH stretching and bending	3440, 1640 [3]
-CH ₂ symmetric	2925 [30]
-CH ₂ asymmetric	2852 [30]

a.)



b



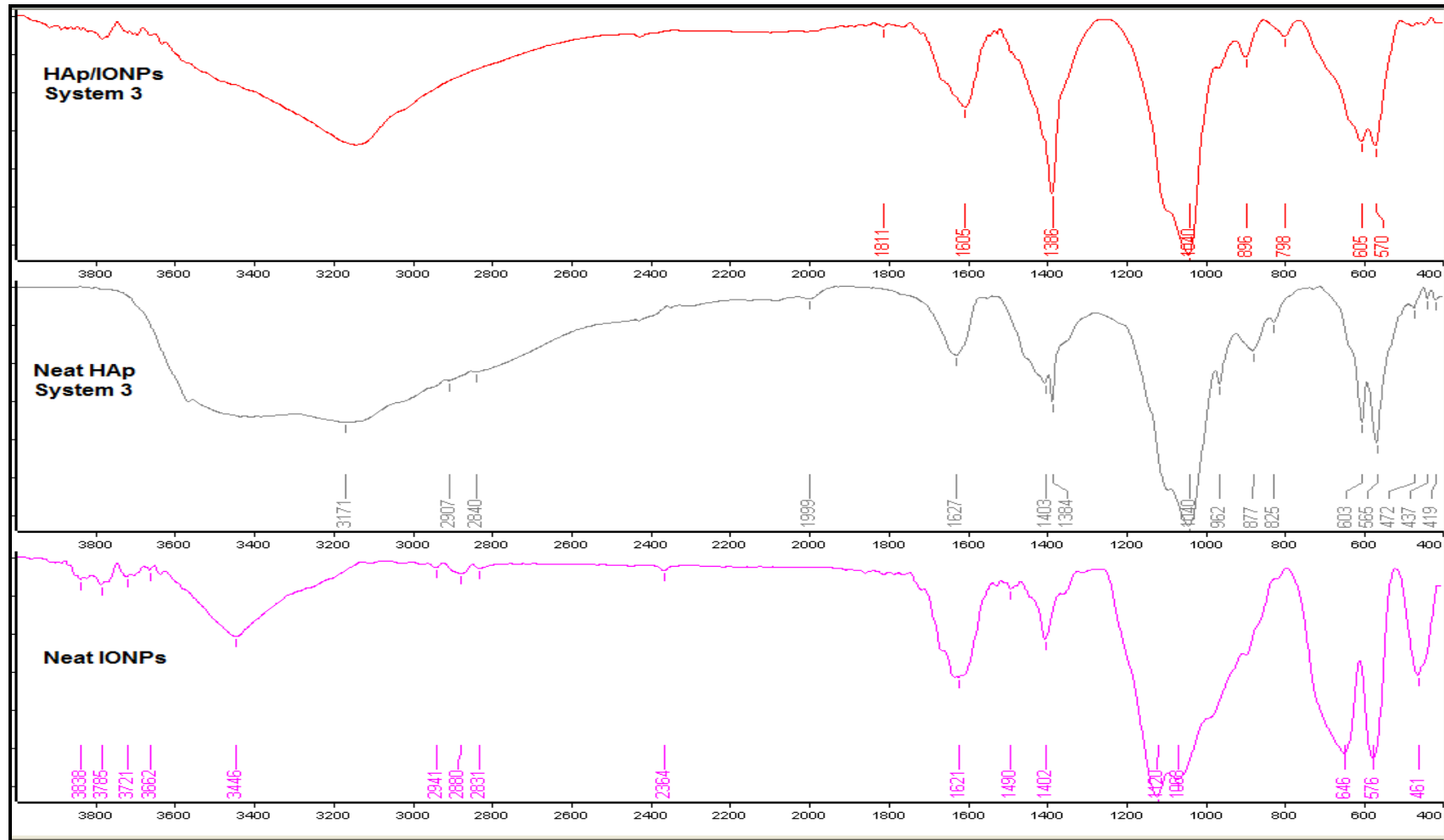


Figure. 2. FT-IR spectra of HAp/IONPs a.) S1, b.) S2, c.) S3 compared with neat IONPs and neat HAp

As given in Fig.2 it was hard to identify Fe-O bands in the composites due to the presence of HAp coating [30] as there are overlapping regions of both IONPs and HAp [29]. However the phosphate lattice as not affected by the presence of IONPs, but the intensity of the peaks has reduced more clearly as in S2 system (Fig. 2. b). The interaction of polymer molecules during the preparation of HAp/IONP composites was evidenced with presence of small humps in S1 and S3 which corresponds to the $-CH_2$ vibrational bands [30].

Morphological characterization of HAp/IONP composites by SEM and TEM

The morphological appearance of as synthesized neat IONPs was examined using TEM. Fig.3 shows that these nanoparticles were almost monodispersed and spherical in shape giving rise to an average diameter of 10-15 nm.

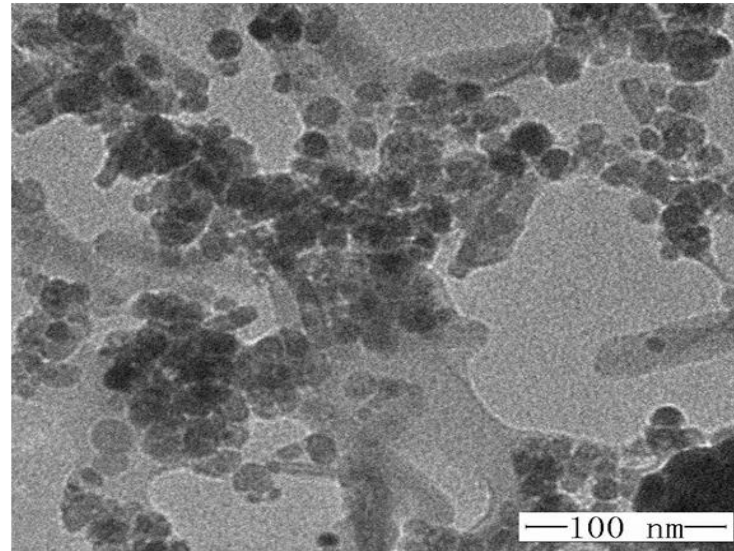
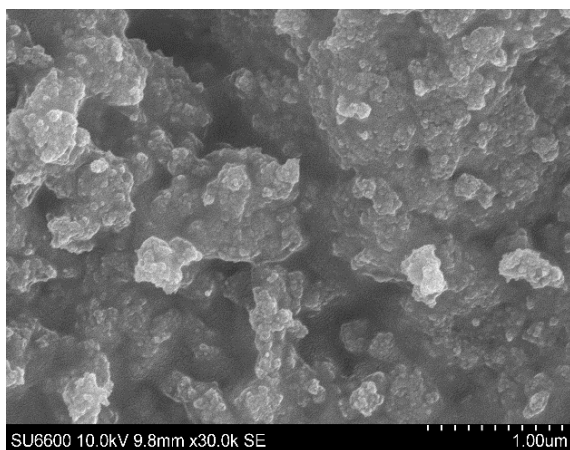
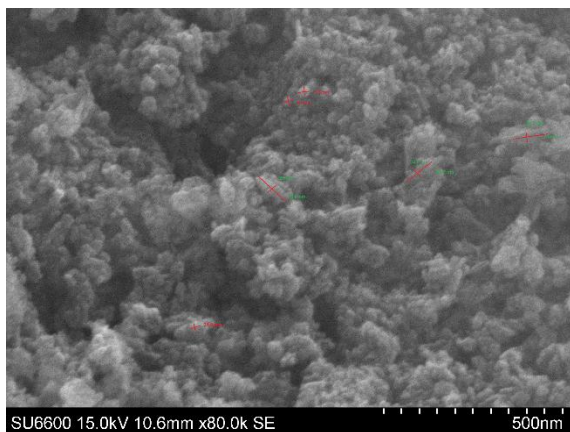


Figure.3. TEM micrograph of neat IONPs obtained under an accelerating voltage of 10 kV

According to the SEM micrographs of HAp/IONPs composites given in Fig.4.c, it is clear that S3 is more homogeneous in nature when compared with the other systems having a diameter of $15 \text{ nm} \pm 7.5 \text{ nm}$. S1 (Fig.4.a.) is consisted of both rods ($100 \pm 1 \text{ nm}$ length $24.9 \pm 0.4 \text{ nm}$ width) and spheres (diameter of $25 \pm 2.3 \text{ nm}$) in the HAp coating. This has created somewhat heterogeneity to the final appearance of the HAp/IONP composite. However this type of an observation could occur due to the reason that the ripening time was not adequate for S1 system for the spheres to transform in to rods completely. In S2 (Fig.4.b.), an aggregated cluster like appearance was created where the IONPs are embedded on the HAp matrix. As it is appearing as clusters a definite size cannot be specified. More importantly these obtained morphologies are different from the ones in already reported work. Specifically preserving the spherical nature of the IONPs while being coated by the HAp is not that common [4,12,13,15,18,19,24,29].

a.) & b.)



c.)

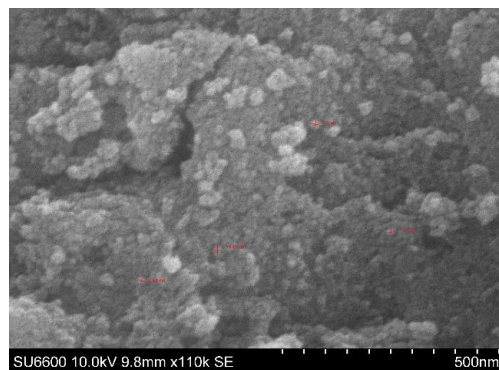


Figure. 4. SEM micrographs of HAp/IONPs systems a.) S1, b.) S2, c.) S3

Elemental composition analysis by XRF

X-ray fluorescence was adopted to investigate the elemental composition, and the corresponding XRF spectra revealed (Supplementary Information- Fig. S3 a,b,c) the presence of Ca, P and Fe in the samples. Additionally in the system S2, Mg^{2+} was scarcely appearing with a weak peak around 1.25 eV, as the emission of Mg is too weak to detect above the noise.

Thermal degradation of the HAp/IONP composites

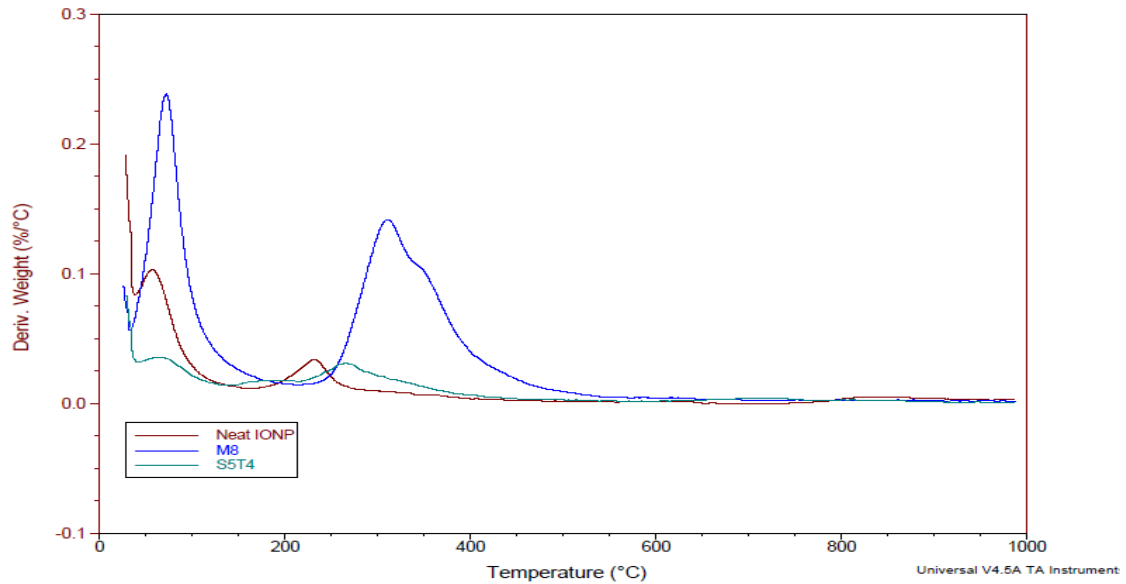
Fig.6 Shows the DTG curves of the composites compared with the DTG curves of the neat IONPs and HAp. In neat IONPs, HAp corresponding to S1 and S1 the weight loss in the 0-150 °C range could be due to the removal of adsorbed water [10,14]. A signature peak at 250 °C of IONPs is absent in neat HAp sample [14]. The weight loss in neat HAp occurring in the region of 250-450 °C can be accounted for the degradation of polymer [10] associated with the loss of lattice water [10,14]. Therefore in the composite a peak appearing in between 250-300 °C (with a peak shift towards the high temperature) highlights the incorporation of the polymer bound HAp and neat IONPs.

Similarly in S2, the degradation pattern is more similar to neat IONPs with a slight shift of the characteristic peak of IONPs neat 250 °C. This highlights the interaction of HAp with IONPs. A peak at 900-1000 °C could arise due to the evolution of CO_3^{2-} ions from HAp as CO_2 [31].

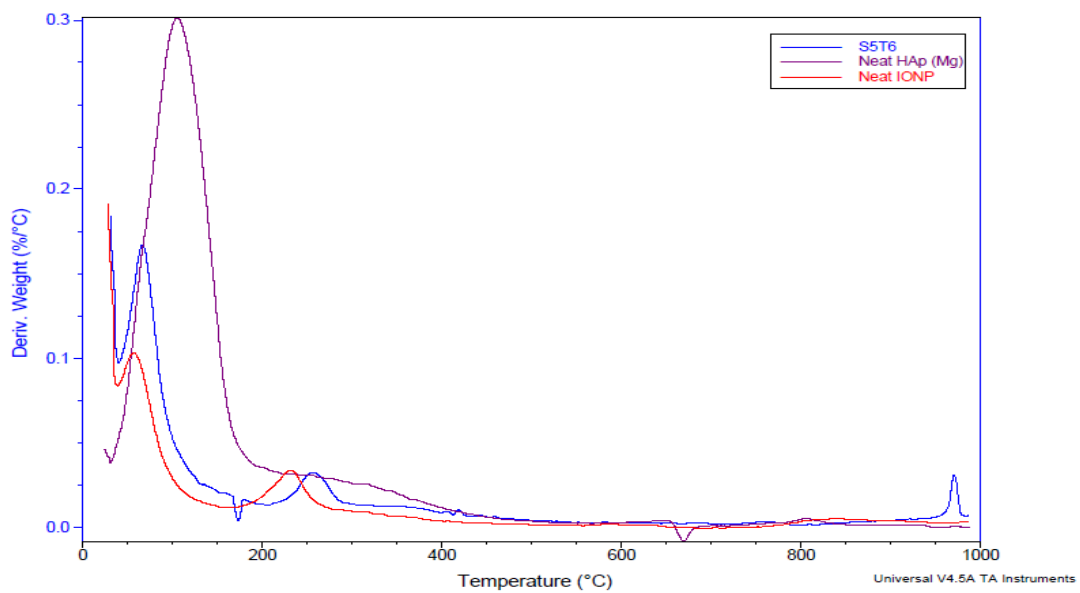
In S3, apart from the removal of adsorbed water, it is clearly observed that the signature peak of IONPs has linked with the decomposition of the polymer

(NaAlg) bound to HAp and the dehydroxylation of HAp. This has created a peak shift in the DTG curve of S3.

a.)



b.)



c.)

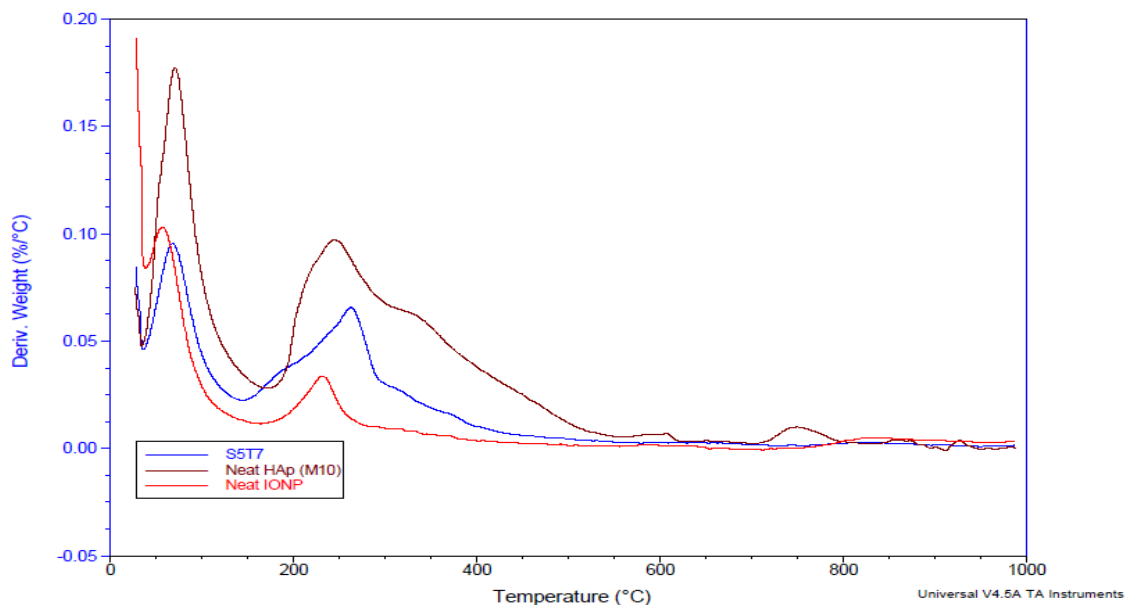


Figure. 5. DTG curves of HAp/IONPs composites a.) S1, b.) S2 and c.) S3

Assessment of Ca and Fe leaching and the percentage yield

The amount of Ca and Fe leaching of each composite was assessed using AAS method. The percentage amount of Ca and Fe released by these systems with respect to the total Ca and Fe content is given in Table 2 (Supplementary Information). Moreover the percentage yield of each system was also calculated

and tabulated in Table 2 (Supplementary Information).

These magnetic hydroxyapatite nanocomposites can be quickly separated from their dispersion under a magnetic field placed close to the sample holder as given in Fig.7. This indicates that the dispersions of these magnetic components can be easily manipulated under an external magnetic field.



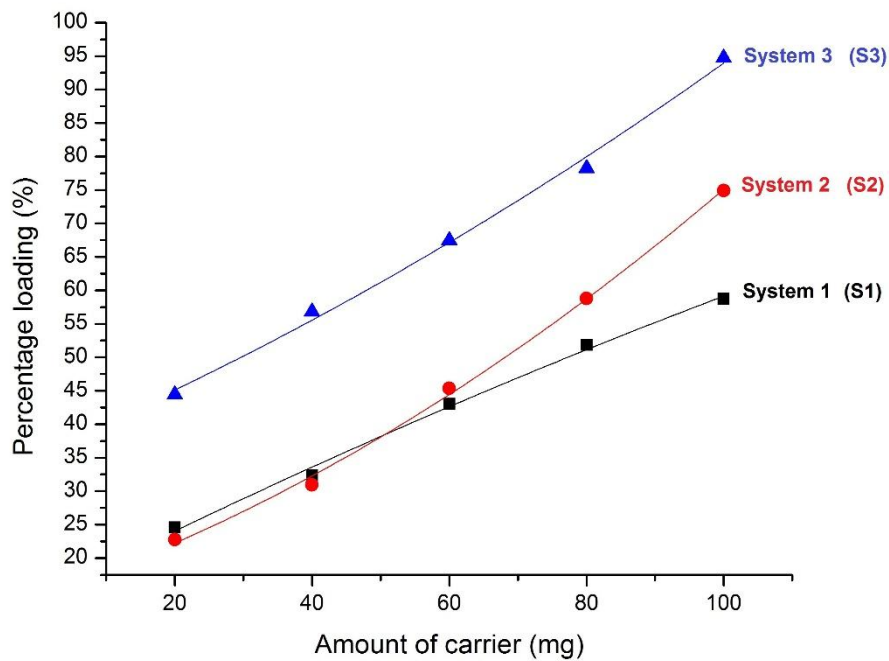
Figure. 6. Magnetic separation of composites placed under a magnetic field

Paracetamol loading and releasing studies

The drug adsorption behavior of S1,S2 and S3 was assessed by adding a constant amount of drug concentration over a varying amount of the carrier material from each system. As given in Fig. 7, the

system S3 has shown the maximum encapsulation efficiency of 95.1% which was identified as the best over the other two systems. Therefore this particular system was selected to carryout the drug releasing studies.

Figure. Drug



7.

adsorption capability of S1, S2 and S3 over a constant amount of paracetamol, at varying concentrations of the carrier

The paracetamol releasing behavior from the paracetamol adsorbed S3 system with an initial concentration of 8.56 mg/L was investigated in PBS (pH 7.4) and sodium acetate (pH 5.5) buffer solutions at 37 °C. As shown in Fig. 8.a and b, the paracetamol release was somewhat high in the first several hours. After this rapid release stage, the releasing rate was reduced and have maintained a level still below 30%. At the end of the incubation for 7 days the cumulative release percentage in PBS was 14% (Fig.8. a) and in acetate buffer it was 25% (Fig. 8. b) , and more importantly the release is still continuing. This highlights that S3 has extended its slow releasing property both in pH 7.4 and pH 5.5 more than for 7 days. A higher releasing profile at low pH can be attributed to the increased dissolution of the nanocarrier in the acidic medium. This dissolution process may enhance the release of the drug

molecules in to the solution. Also as this composite contains NaAlg as a polymer by being incorporated in to HAp, that might also trigger the drug release more in acidic medium rather than in alkaline pH, because the polymer might get swollen with the lowering of the pH and that will create much void areas for the release of the drug molecules.

However when compared with the neat paracetamol release without a carrier material, after 3 ½ days the total amount of the paracetamol is completely released in both pH 7.4 buffer and in pH 5.5 buffer (Fig. 8.c and d). These experimental results indicate that the as prepared HAp/IONPs have favorable pH controlled drug releasing property and it is promising for the application as a pH responsive drug carrier which can be identified as a potential candidate for the delivery of drugs to diseases like cancer.

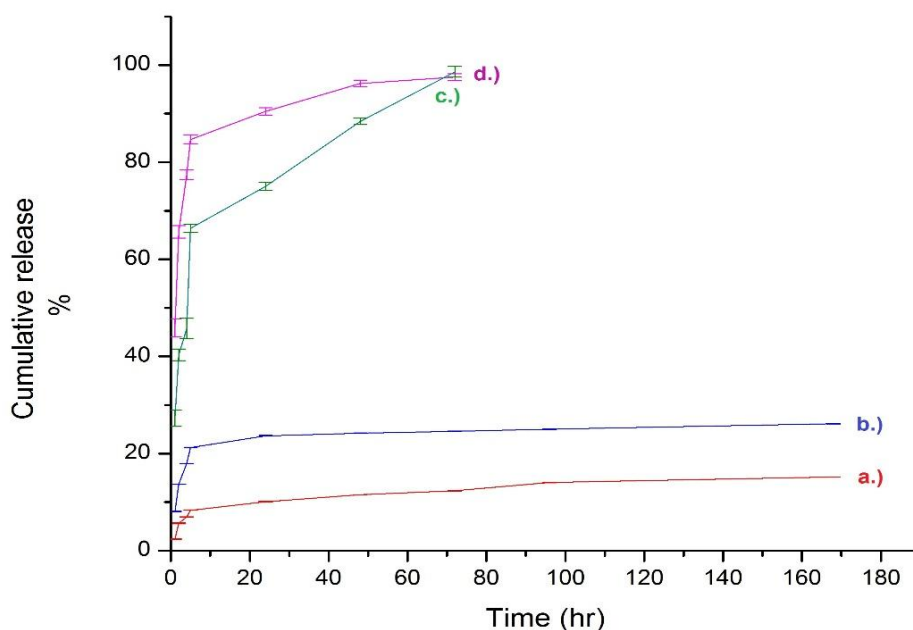


Figure. 8. Cumulative release percentage of paracetamol from S3 system a.) in PBS, b.) in acetate buffer, c.) Cumulative release of neat paracetamol in PBS, d.) Cumulative release of paracetamol in acetate buffer

CONCLUSIONS

A facile wet chemical co-precipitation technique has been developed for the creation of HAp coated IONPs via three different approaches. These as prepared HAp/IONP nanocomposites have shown different crystallinity and morphologies based on the additives that has been added during the preparation

of these composites. The drug encapsulation efficiency of those systems was investigated by loading a model drug like paracetamol. NaAlg incorporated S3 system has shown the highest encapsulation efficiency over the other two systems and also it has highlighted its capability to mediate a good sustained releasing profile in a pH controlled manner which could even continue the drug releasing

property more than 7 days. Due to the high biocompatibility, magnetic responsive behavior and pH controlled slow drug releasing ability, these composites can be identified as a promising tool for targeted drug delivery, specially in cancer treatment. Also this approach introduces a novel and a greener, rapid approach to synthesize HAp/IONP composites which eliminates the use of high temperature, long processing time, calcination and freeze drying.

ACKNOWLEDGEMENT

Authors like to convey the sincere gratitude for all the supporting bodies, specially the National Research Council (NRC) for the financial support, all the members in Sri Lanka Institute of Nanotechnology (SLINTEC) for the help given for characterization purposes and the lab technicians of University of Colombo for the help provided.

REFERENCES

Akbarzadeh. A., Samiei. M., Joo. S. W., Anzaby. M., Hanifehpour. Y., Nasrabadi. H. T., Davaran. S. (2012). *Journal of Nanobiotechnology*, 10, 1-13.

Gopi. D., Ansari. M. T., Shinyjoy. E., Kavitha. L. (2012), *Spectrochimica Acta Part A*, 87, 245-250.

Covaliu. C. I., georgescu. G., Jitaru. I., Malaeru. T., Neamtu. J., Oprea. O., Patroi. E. (2009), *REV. CHIM.(Bucuresti)*, 60(12). Retrieved from <http://www.revistadechimie.ro>

Wu. H. C., Wang. T. W., Sun. J. S., Wang. W. H., Lin. F. H., (2007). *Nanobiotechnology*, 18,1-9.

Ansar. E. B., Ajeesh. M., Yokogawa. Y., Wunderlich. W., Varma. H. (2012). *Journal of American Ceramic Society*, 95, 2695-2699.

Gloria. A., Russo. T., D'Amora. U., Zeppetelli. S., D'Alessandro. T., Sandri. M., Lopez. M. B., Redondo. Y. P., Uhlarz. M., Tapieri. A., Rivas. J., Herrmannsdörfer. T., Dediu. V. A., Ambrosio. L., De Santis. R., (2013). *Journal of the Royal Society Interface*, 10, 1-11.

Pistone. A., Iannazzo. D., Panseri. S., Montesi. M., Tampieri. A., Galvagno. S., (2014). *Nanotechnology*, 25, 1-9.

Koneracka. M., Zavisona. V., Timko. M., Kopcansky. P., Tomasovicova. N., Csach. K., (2008), *Acta Physica Polonica A*, 113, 595.Habibi. N., (2014). *Spectrochimica Acta Part A: Molecular and Biomolecular Spectroscopy*, 131, 55-58.

Iwasaki. T., Nakatsuka. R., Murase. K., Talcata. H., Nakamura. H., Watano. S., (2013). *International Journal of Molecular Sciences*, 14, 9365-9378.

Zuo. G., Wan. Y., Zhang. Y., (2012). *Material Letters*, 68, 225-227.

Yu. Q., Li. X. S., Yuan. B. F., Feng. Y. Q., (2014), *Journal of Separation Science*, 37, 580-586.

Yang. H., Masse. S., Zhang. H., Helary. C., Li., Coradin. T., (2014), *Journal of Colloid and Interface Science*, 417, 1-8.

Sheikh. L., Mahto. N., Nayar. S., (2015), *Journal of Material Science: Materials in Medicine*, 26, 1-8.

Tran. N., Webster. T. J., (2011), *Acta Biomaterialia*, 7, 1298-1306.

Epple. M., Ganesan. K., Heumann. R., Kleising. J., Kovtun. A., Neumann. S., Sokolova. V., (2010). *Journal of Material Chemistry*, 20, 18-23.

Hou. C. H., Hou. S. M., Hsueh. Y. S., Lin. J., Wu. H. C., Lin. F. H., (2009). *Biomaterials*, 30, 3956-3960.

Panseri. S., Cunha. C., D'Alessandro. T., Sandri. M., Russo. A., Giavaresi. G., Marcacci. M., Hung. C. T., Tampieri. A., (2012). *PLoS One*, 7, 1-8.

Chen. F., Li. C., Zhu. Y. J., Zhao. X. Y., Lu. B. Q., Wu. J., (2013), *Biomaterials Science*, 1, 1074-1081.

Chen. F., Tang. Q. L., Zhu. Y. J., Wang. K. W., Zhang. M. L., Zhai. W. Y., Chang. J. A., (2010). *Acta Biomaterialia*, 6, 3013-3020.

Chen. F., Zhu. Y. J., Wang. K. W., Zhao. K. L., (2011), *Crystal Engineering Communication*, 13, 1858-1863.

Zhang. H. B., Zhou. K. C., Li. Z. Y., Huang. S. P., (2009). *Journal of Physics and Chemistry Solids*, 70, 243-248.

Jevtic. M., Mitric. M., Skapin. S., Jancar. B., Ignjatovic. N., Uskokovic. D., (2008). *Crystal Growth & Design*, 8, 2217-2222.

Zeng. X. B., Hu. H., Xie. L. Q., Lan. F., Jiang. W., Wu. Y., Gu. Z. W., (2012). *International Journal of Nanomedicine*, 7, 3365-3378.

Wu. H. C., Wang. T. W., Bohn. M. C., Lin. F. H., Spector. M., (2010). *Advanced Functional Materials*, 20, 67-77.

Wakiya. N., Yamasaki. M., Adachi. T., Inukai. A., Sakamoto. N., Fu. D., Sakurai. O., Shinozaki. K., Suzuki. H., (2010). *Materials Science and Engineering: B*, 173, 195-198.

Wu. H. C., Wang. T. W., Sun. J. S., Wang. W. H., Lin. F. H., (2007). *Nanotechnology*, 18, 165601-165609.

Mir. A., Mallik. D., Bhattacharyya. S., Mahata. D., Sinha. A., Nayar. S., (2010). *Journal of Material Science: Materials in Medicine*, 21, 2365-2369.

Donadel. K., Felisberto. M. D. V., Laranjeira. C. M., (2009). *Anais da Academia Brasileira de Ciencias*, 81, 179-186.

Chitprasert. P., Sudsai. P., Rodklongtan. A., (2012). *Carbohydrate Polymers*, 90, 78-86.

Haas. H., Banewicz. J., (1980). *Radiocarbon*, 22, 537-544.

Appendix

FACILE SYNTHESIS OF HYDROXYAPATITE/ IRON OXIDE NANOCOMPOSITE TO BE USED AS A DRUG CARRIER

SUPPLEMENTARY INFORMATION

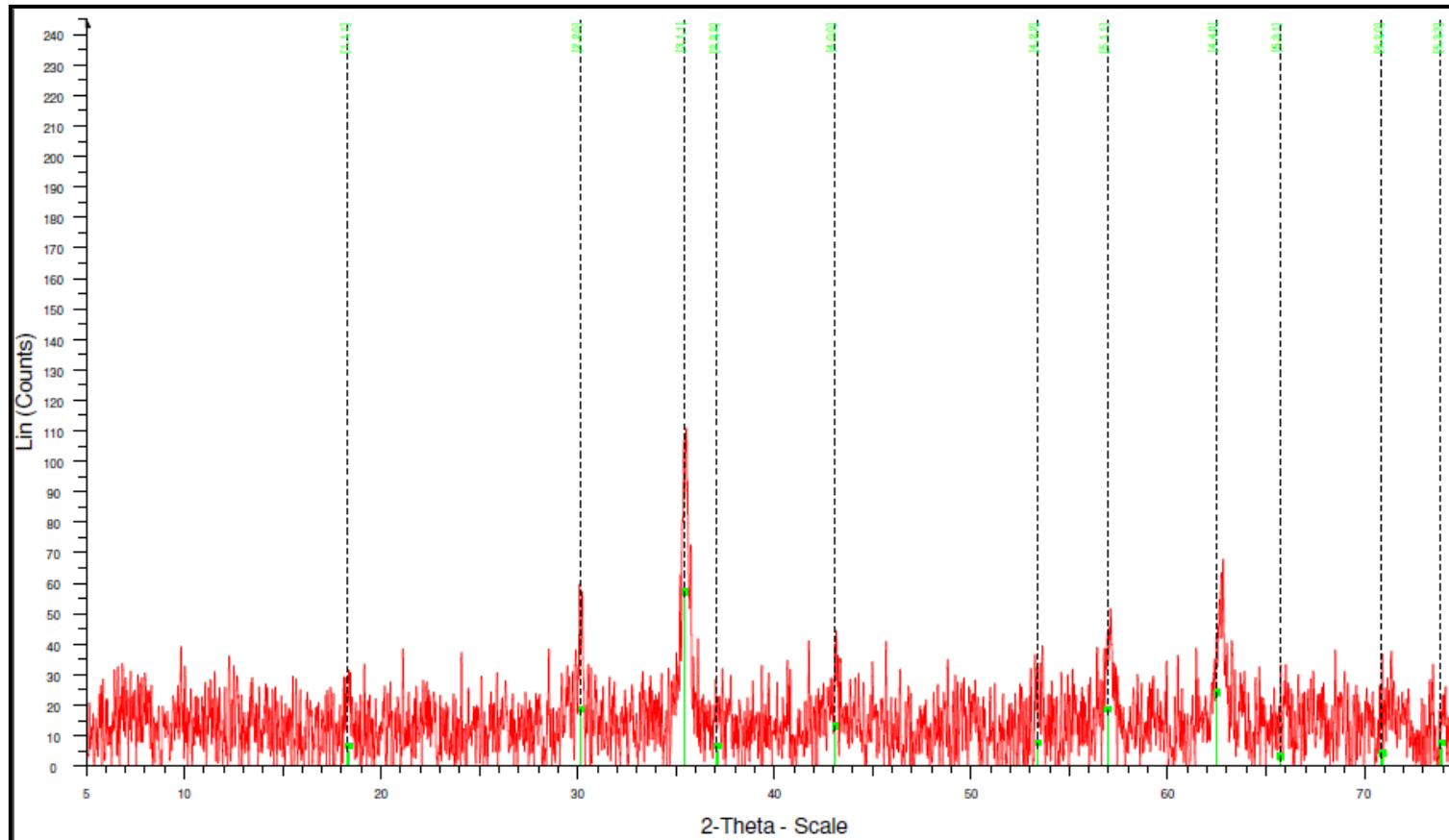


Figure. S1. XRD pattern of neat IONPs

a.)

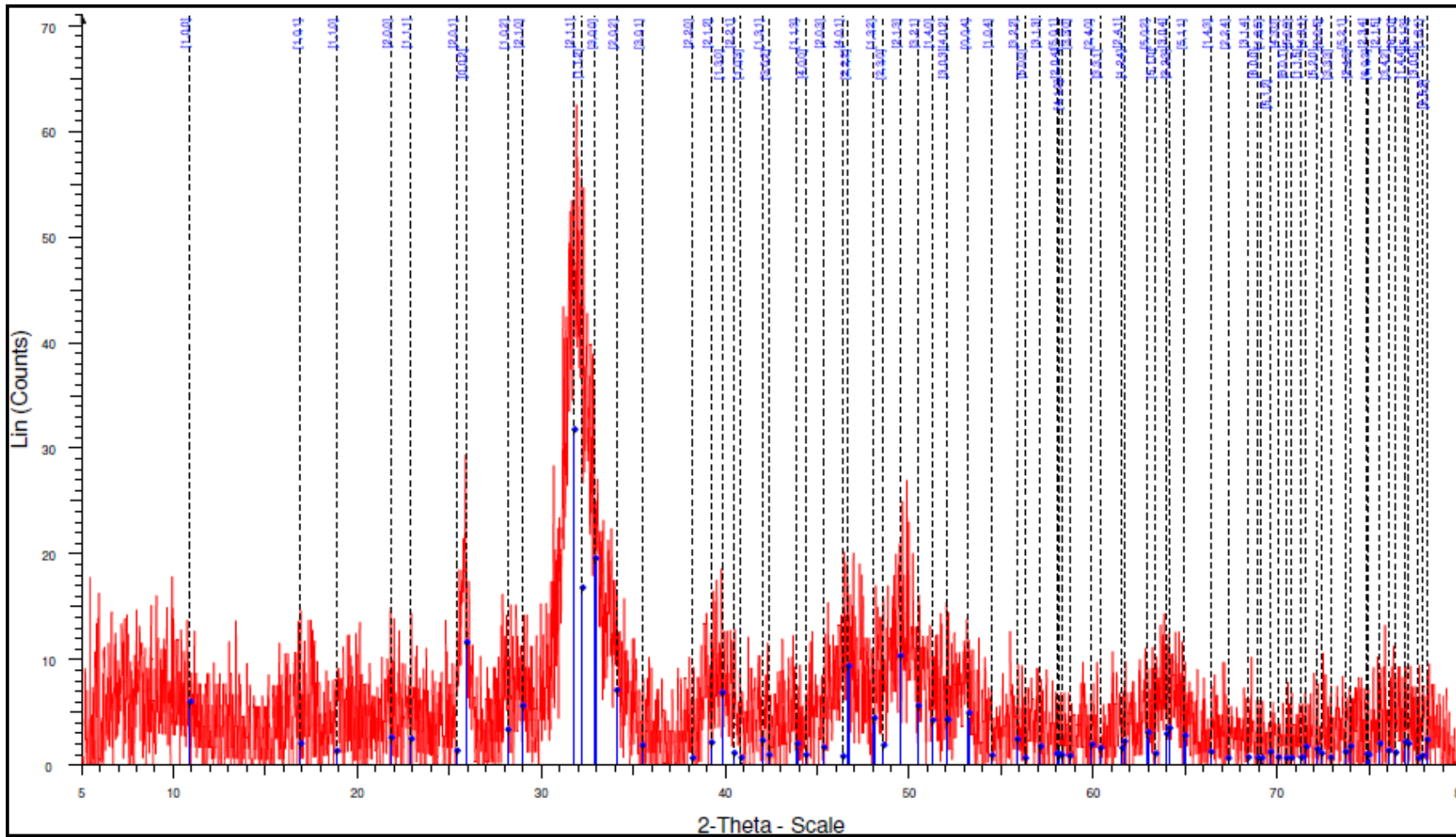
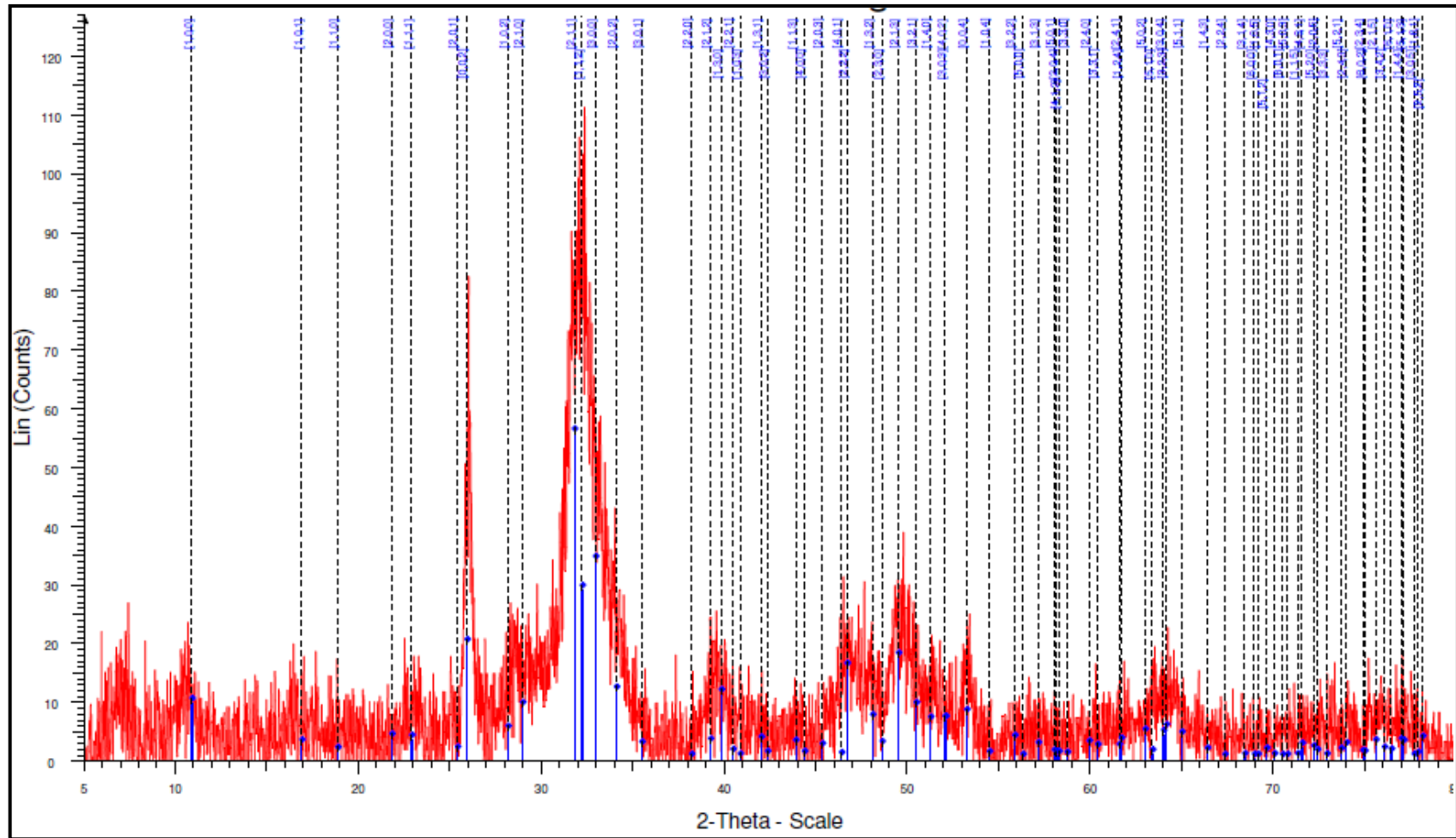


Figure.
PXRD



S2.

patterns of a.) HAp synthesized in the presence of CMC, b.) HAp synthesized in the presence of Mg^{2+} , c.) HAp synthesized in the presence of NaAlg

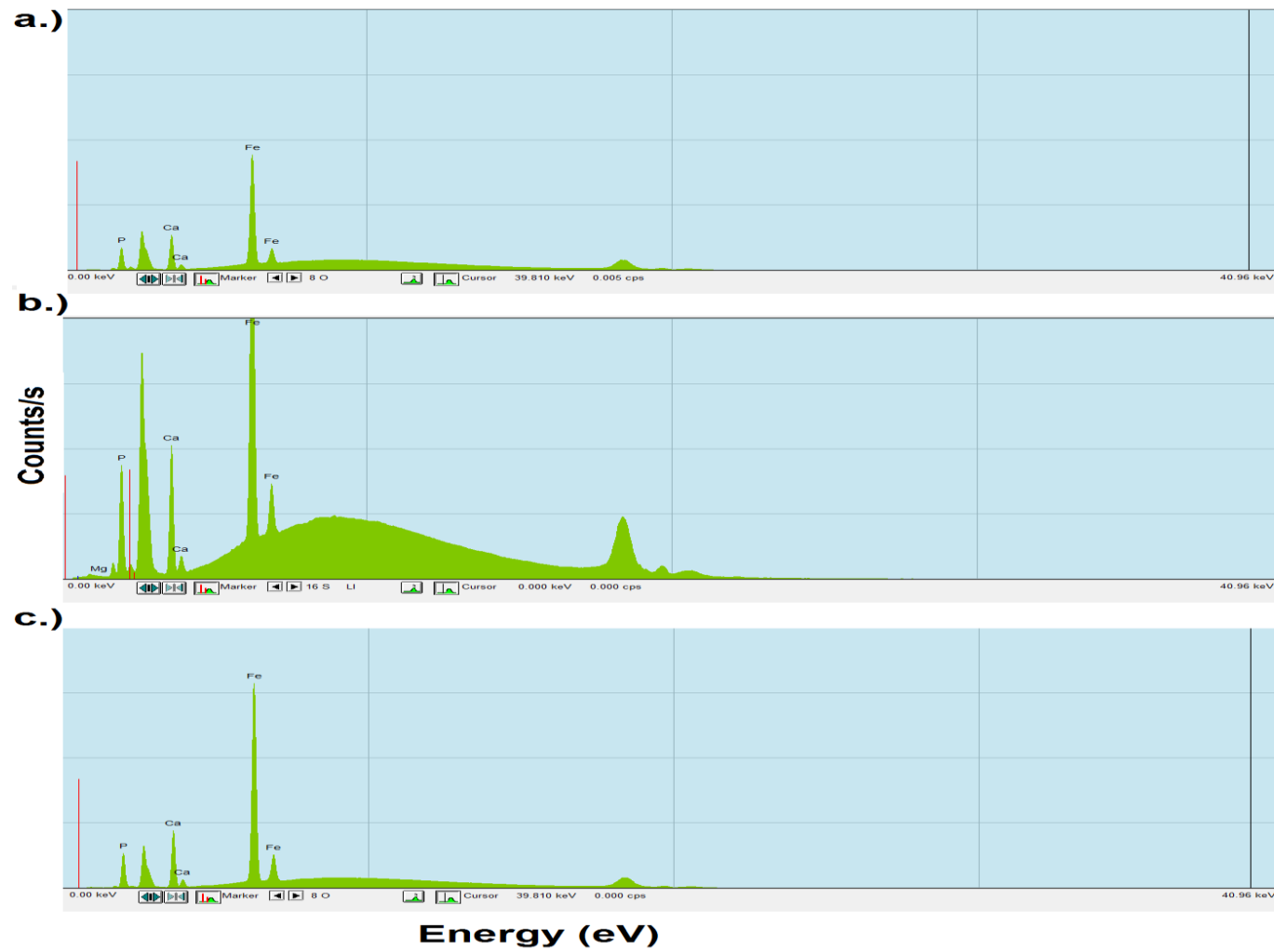


Figure. S3. XRF pattern of a.) S1, b.) S2, c.) S3

Table 2: Percentage Ca and Fe leaching and percentage yield of HAp/ IONP composites

System	Ca leaching %	Fe leaching %	% Yield
S1	0.022	0.30	56.76
S2	0.070	0.08	80.89
S3	0.063	0.08	91.60

COMPARISON OF SURFACE MORPHOLOGY OF SMOOTH VERSUS POROUS MICROFIBRES MADE FROM POLY (L-LACTIDE)

Macajová, E¹, Cudlínová, M² and Kejzlar, P³

¹*Department of Material Science, Technical University of Liberec, Liberec, Czech Republic*

²*Nanopharma, a.s., Czech Republic*

³*Institute for Nanomaterials, Advanced Technologies and Innovation, Technical University of Liberec, Liberec, Czech Republic*

Abstract

Nano/microfibers prepared by electrospinning have a plenty of extraordinary properties applicable in many industrial fields. Large specific surface area is main advantage of these fibers. Usually the surface of nano/microfibers is almost smooth. Through the process parameters it is possible to obtain porous surface of individual fibres which leads to the pronounced increase in surface area. Their morphology can be affected not only by the spinning process parameters but also by the composition of polymer solution and by the used solvents. Porous fibers may have a variety of uses in numerous applications because they show even larger specific surface area compared to smooth fibers. Porous nanofibers can provide better adhesion for the cells, more rapid degradation time, etc. Porous biodegradable Poly(l-lactide) (PLLA) fibers were produced using the electrospinning method from the needle. One of the possible method to evaluate the increase of the surface area is HR-SEM image analysis. The present work demonstrates the usage of new method enabling the assessment of porosity contribution to increase in micro/nanofiber surface area.

Keywords: Porous nanofibers, electrospinning, surface morphology, micro/nanofibers, structure

INTRODUCTION

Polymeric nano/microfibres can be produced by the use of an electrospinning method, in which electric forces affect polymeric solution or melt. Under appropriate conditions an electrically charged polymer solution will create very thin fibres by the use of the electrostatic field effect. The formation of fibre occurs between two oppositely charged electrodes, one of which is in contact with the liquid, the second electrode serves as a collector where fibrous layer is formed. The diameter of fibres made by electrospinning may vary from tens of nanometers to micrometers. The diameter of fibres is most often in the range of 100-750 nm, depending on the type of polymer and external conditions of spinning process. Fibres produced by electrospinning have enormous potential in many fields especially in medicine, engineering, clothing industry, aerospace, energy etc. [1-5]

Currently, some scientists are focused on the studies of the structural morphology of nanofibres. The studies are focused on the method how to characterize and optimize the spinning process and determine the best spinning parameters. [6-8] Electrospinning process is influenced by the properties of the polymer solution, i.e. viscosity or surface tension. Morphology and diameter of the fibers are influenced by the composition of solvent/precipitants mixture.

Porous nanofibers exhibit many advantages over smooth fibres, because due to their porosity they have a significantly larger surface area. High porosity and rough surface are beneficial for the adhesion and proliferation of cells into nanofibrous layers in tissue engineering and in controlled drug release. For the use in medicine, material must not be toxic, carcinogenic, mutagenic, allergenic and must not contain any impurities. [6] These nanofibers can be made from natural materials like from biodegradable polymers suitable for application in medicine due to their biocompatibility. These materials include a

variety of natural and synthetic polymers. Examples of the useable natural materials either pure or partially modified can be collagen and gelatin, cellulose and its derivatives, chitin and its derivatives. From the synthetic polymers dominate polylactic acid (PLA) and its copolyesters, polyglycolic acid (PGA) or polycaprolactone (PCL) and polyurethanes (PUR). Many nanofibers of this type can be good carriers of active pharmaceutical substances. The advantage is that during the therapeutic effect may be some types of these fibres spread and do not represent long term burden for the organism. [9-11] In addition, the large specific surface is important in filtration or in the chemical industry. [5] The structure and porosity of fibres can also affect the different evaporation speed of the solvent/ precipitants mixture in the polymer solution. [12] A study dealing with the production of porous fibres was published in [13].

It was experimentally established that the pores in the surface of nanofibers arise due to evaporation of a secondary solvent. Their shape depends on the stage, wherein pores are formed (during drawing the fiber, respectively, after completion of stretching).

MATERIAL

For the present experiment was selected poly(L-lactide) – PLLA. Poly (lactic acid) (PLA) and their

copolymers are the most widely investigated and used synthetic degradable polymers for biomedical applications. [14]

Poly(lactide) (PLA) is synthesized via ring-opening polymerization of lactic acid dimers (lactide rings) which contain two optical isomers, referred to as D-lactide or L-lactide. Poly(L-lactide) (PLLA) is a semicrystalline polymer exhibiting a high modulus and a slow degradation time (more than 24 months); whereas poly(D,L-lactide) (PDLA) is amorphous and has a low modulus and a more rapid degradation time (12 to 16 months) which makes it more suitable for drug delivery systems. [15-16] .

EXPERIMENTAL PART

Electrospinning

This work aims with creating of pores into nanofibers surface and evaluation of their effect on the increase of fibre specific surface area. Nanofibrous layers were produced by a needle electrospinning method; this device is shown in Figure 1. The electrospinning process is described in detail in [17].

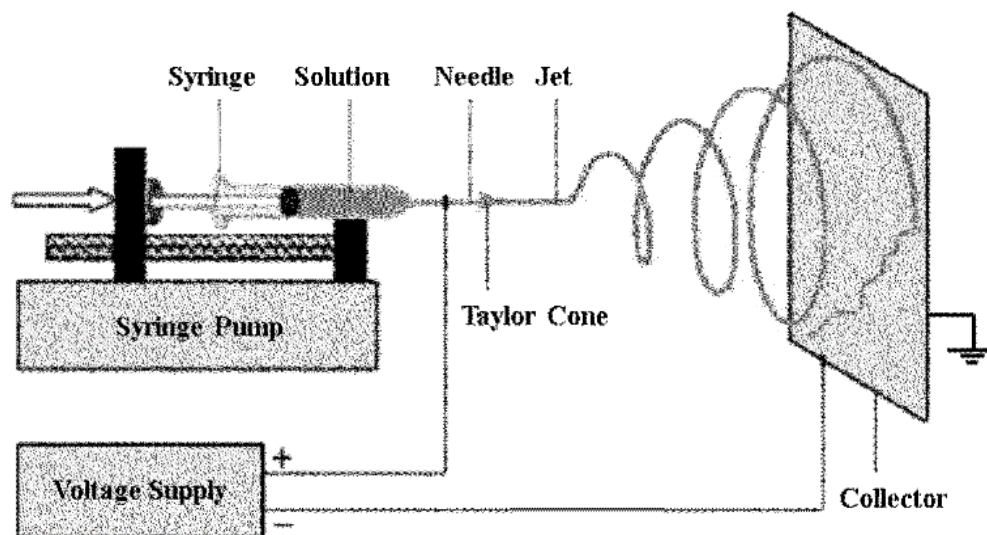


Figure 1. Diagram of the electrospinning setup. Basic electrospinning device consists of syringe with polymer solution, needle serving as the electrode with high voltage and collector which can be grounded or connected to an opposite high voltage. The polymer solution is fed through the needle and fibers are ejected from drop of polymer in high electric field between the needle and collector. These fibers are then collected on Collector.

Preparation of PLLA solution

10% PLLA solution with molecular weight $M_w = 75\,000 - 120\,000$ g/mol was used for the preparation of porous nanofibers. PLLA was dissolved in the mixture of Dichlormethane (DCHM) und dimethyl sulfoxide (DMSO). Mixing ratio of solvents (DCHM/DMSO) was 9:1.

Other monitored parameters were following: spinning tension, collector distance and dosage (see Table 1).

Table 1 Proposed experimental parameters.

Concentration HPLC/DMSO	High voltage [kV]	Collector distance [cm]	Polymer dosing [ml/h]
9:1	15; 20; 25	25	15; 20; 25

Evaluation of the Structure

The morphology of the PLLA micro/nanofibers layers was assessed on the basis of image analysis of HR-SEM images.

In Figure 2 there is detailed view of the individual porous microfiber. The solvent ratio was 9:1, voltage of electrode 30 kV, the collector distance was 25 cm and polymer dosage of 15 ml / h. The fibre diameter ranged from 700 to 1100 nm; the diameter of the particular pores ranged in the order of tens of nm.

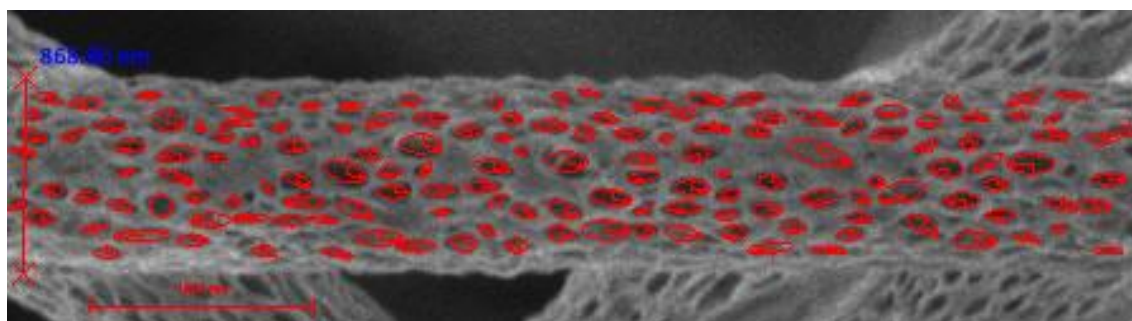


Figure 2. HR SEM image of electrostatically electrospun fibre of 10% PLLA. Measurement of whole pores

Specific Surface Area of Porous Fibres

For the evaluation of the effect of pores-implementation into the fiber surface, following method was suggested.

Evaluated fibrous structures have to fulfil the following conditions:

1. All fibres have nearly similar diameter.
2. The shape of pores is ellipsoidal.
3. All produced fibres are porous.

Porous microfibers were evaluated on the basis of image analysis of HR-SEM images in NIS – Elements SW. Diameter of fiber, length and diameters of individual pores were measured on the selected representative part of porous fibre (see Figure 3).

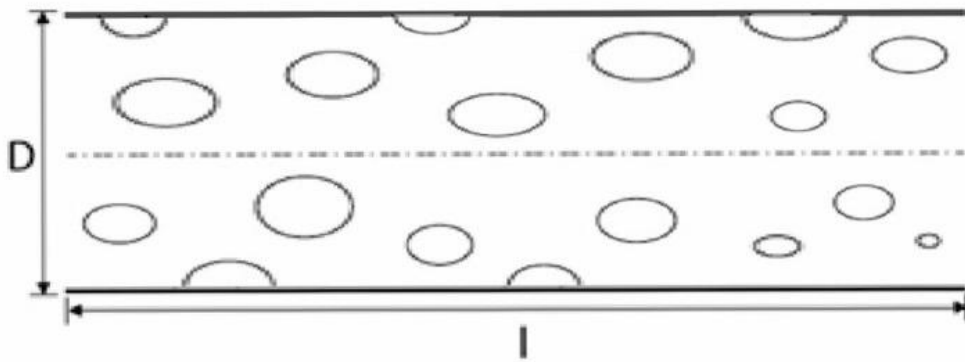


Figure 3. A schema of porous fibre, where l is measured length and D is its diameter

Smooth fibre:

The surface area (S_{sf}) of smooth fibre can be calculated using the equation (1), its volume corresponds to (2).

$$S_{sf} = \pi \cdot D \cdot l \tag{1}$$

$$V_{sf} = \frac{\pi \cdot D^2 \cdot l}{4} \tag{2}$$

Then the specific surface (KSF) could be calculated as (3).

$$K_{SF} = \frac{S_{sf}}{V_{sf}} = \frac{4}{D} \tag{3}$$

- Ssf..... surface area of the smooth fibre
- Spf..... surface area of the porous fibre
- Vsf..... volume in smooth fibre
- Vpf..... volume in porous fibre
- D..... diameter of the fibre
- di..... diameter of individual pores
- n..... quantity of pores on the measured length of the fibre
- l..... measured length of the fibre

Porous fibre:

The surface area of porous fibres (S_{pf}) can be calculated as (4).

S_{pf} = surface of smooth fibre - projected area of pores + surface of ellipsoids

$$S_{pf} = \pi \cdot D \cdot l - \sum_{i=1}^n S_i + \sum_{i=1}^n \frac{P_i}{2} \tag{4}$$

The volume of porous fibre is equal to (5).

$$V_{pf} = \pi \cdot \frac{d^2}{4} \cdot l - \sum_{i=1}^n \frac{4}{3} \cdot \pi \cdot \frac{ab^2}{2} - \sum_{i=1}^n \frac{1}{4} \cdot \frac{4}{3} \cdot \pi ab^2 \tag{5}$$

a, b are semi-axes of oval pores.

Finally, the specific surface of porous fibre can be calculated as (6).

$$K_{PF} = \frac{S_{pf}}{V_{pf}} \quad (6)$$

Relative area increase (RAI) due to porosity (7).

$$RAI = \frac{S_{pf} \cdot V_{sf}}{V_{pf} \cdot S_{sf}} \quad (7)$$

For the example shown in Fig. 2, the relative area increase RAI due to fibre porosity:

$$RAI = \frac{20364167,07}{3694070126} \cdot \frac{3694905660}{15236724,37} = 1,34 \Rightarrow \text{The increase in surface area due to pores presence is approximately 34 \% .}$$

CONCLUSION

This work was focused on the usage of new method enabling the assessment of porosity contribution to increase surface area in micro/nanofibers.

The first part deals with samples preparation with a respect to various parameters of the electrospinning process. The structure and porosity of micro / nanofibers is strongly influenced by a combination of many factors. The shape of pores depends on the stage when pores are formed. If the fibre drawing by the electric forces is finished before pores forming, resulting pores will be spherical and on the other hand if pores are formed during the fibre is still drawn, pores will be oval shaped. Therefore, various configurations of spun solution, various voltage and dosage were tested. The best results with respect to the surface porosity were obtained at following conditions: the solvent ratio was 9:1, voltage of electrode 30 kV, the collector distance of 25 cm and polymer dosage of 15 ml/h. These conditions caused the oval-shape of pores in the surface of PLLA fibres. The average diameter of obtained porous fibres was \approx

870 nm; the average pore's equivalent diameter of pores was \approx 100 nm.

In the second part the morphology of layers was assessed using the image analysis of high resolution images taken by the scanning electron microscope.

In Ref. [18] there was proposed a method for evaluation of RAI parameter for spherical pores, in this work the equations were modified for oval pores. The basic measured dimensions were the fibre length and diameter and both semi-axis of pores. RAI parameter was calculated by the use of equations (1-7). This article demonstrates that porosity of the fiber contributes to increase the specific surface area. The RAI parameter was about 34 % due to porosity.

ACKNOWLEDGMENTS

This article is financially supported by the "Institutional Development Project" of CZ Ministry of Education, Youth and Sports.

REFERENCES

ANDRADY, A. L. (2008), Science and Technology of Polymer Nanofibres, (Wiley, Hoboken, NJ.)

FILATOV, Y., BUDYKA, A. KIRICHENKO, V. (2007), Electrospinning of Micro- and Nanofibers: Fundamentals in Separation and Filtration Processes (Begell House, Redding)

JIRSÁK, O., et al.: (2005), A method of nanofibres production from a polymer solution using electrostatic spinning and a device for carrying out the method, US Patent, WO2005024101.

LUKÁŠ, D., et al.: (2009), Physical principles of electrospinning (Electrospinning as a nano-scale technology of the twenty-first century), Textile Progress, Taylor & Francis, Vol. 41, No2, 2009, 59-140, ISBN – 13: 978-0-415-55823-5

Chempoint. Využití elektrospinningu pro syntézu materiálů použitelných v tkáňovém inženýrství

[online]. 28. 03. 2012. [cit. 2015-03-06]. Available at:

<http://www.chempoint.cz/vyuziti-elektrospinningu-pro-syntezu-materialu-pouzitelnych-v-tkanovem-inzenyrstvi>

KOLBUKA, D., P. SAJKIEWICZA, K. MANIURA-WEBER a G. FORTUNATOD. 2013. Structure and morphology of electrospun polycaprolactone/gelatine nanofibres [online]. : 10 [cit. 2015-03-01]. DOI: 10.1016/j.eurpolymj.2013.04.036. Available at: <http://www.sciencedirect.com/science/article/pii/S0014305713002280#>

KRISHNAN K, Asha, Cintil JOSEC, Rohith K. R a K.E. GEORGE. 2015. Sisal nanofibril reinforced polypropylene/polystyrene blends: Morphology, mechanical, dynamic mechanical and water transmission studies [online]. : 12 [cit. 2015-04-12]. DOI: 10.1016/j.indcrop.2015.03.076. Available at: <http://www.sciencedirect.com/science/article/pii/S0926669015002666#>

MUGE YUKSELOGLU, S., Nihal SOKMEN a Suat CANOGLU. Biomaterial applications of silk fibroin electrospun nanofibres [online]. October 2015 [cit. 2015-05-12]. DOI: 10.1016/j.mee.2015.04.008. Available at: <http://www.sciencedirect.com/science/article/pii/S0167931715002142#>

KNOW C.H., Biomaterials, et al.: 2, S52 (2007)

Choi J.S. Leong K.W., Yoo H.S. 29, 587 (2008)

GERALD SCOTT. Degradable polymers: Principles and Applications. 2002. vyd. Netherlands: Kluwer Academic Publishers, 2002. ISBN 1-4020-0790-6.

LUBASOVÁ, Daniela, Lenka MARTINOVÁ. Mechanismus tvorby porézních nanovláken z polykaprolaktonu připravených elektrostatickým zvláknováním. Nanocon [online]. 2009, s. 1-6 [cit. 2015-01-20]. Available at: http://www.nanocon.eu/files/proceedings/nanocon_09/Lists/Papers/087.pdf

ALEXANDROS G. KATSOGIANNIS, Konstantinos, Goran T. VLADISAVLJEVIĆ a Stella GEORGIADOU. Porous electrospun polycaprolactone (PCL) fibres by phase separation. Macromolecular Nanotechnology [online].

2015, 69: 284-295 [cit. 2015-07-03]. DOI: 10.1016/j.eurpolymj.2015.01.028. Available at: <http://www.sciencedirect.com/science/article/pii/S0014305715000403>

SCOTT, G. a (Ed.). Degradable Polymers: Principles and Applications. 2. Kluwer Academic, 2002. ISBN 978-94-017-1217-0.

Huayu Tian, Zhaohui Tang, Xiuli Zhuang, Xuesi Chen, and Xiabin Jing, “ Biodegradable Synthetic Polymers: Preparation, Functionalization and Biomedical Application” Progress in Polymer Science, 2012, 37(2), 237-280.

Anna Musyanovych and Katharina Landfester, “Biodegradable Polyester-based Nanoparticle Formation by Miniemulsion Technique” Material Matters, 2012, 7(3), 30-32

Available at: <http://www.google.com/patents/US2013006869>

MACAJOVÁ, Eva. DUFKOVÁ Iva, KEJZLAR Pavel. Nanocon 2014: Structure and morphology of PCL porous nano/microfibres layers. [online]. 2014, r. 6, s. 5 [cit. 2015-02-15]. Available at:

http://www.nanocon.eu/files/uploads/01/NANOCON%202014_2%20content.pdf

ANALYZING THE MULTI-RESONANT PROPERTY OF GRAPHENE OPTICAL NANOANTENNA

Yang, J¹ and Kong, F²

¹*School of Information Science and Engineering, Shandong University, China*

²*Kang, Li, School of Information Science and Engineering, Shandong University, China*

Abstract

The graphene nanoantenna was modeled and its properties were analyzed by finite difference time-domain simulations. The field enhancement and radar cross-section of the antenna for different chemical potentials were calculated, and the effect of the chemical potential on the resonance frequency was analyzed. It is shown that large modulation of resonance peak and intensity in log-periodic nanoantenna can be achieved via turning the chemical potential of graphene. The multi-resonance properties of the antenna have great potential for nanoscale highly nonlinear response and optical sensing.

Keywords: Nanoantenna, graphene, multi-resonance, field enhancement

INTRODUCTION

In the past decades, metal nanoantennas have gained significant interests due to their enormous applications in sensing [1], non-linear spectroscopy [2], nano-imaging [3] active photonic devices [4] and so on. However, the difficulty in controlling and varying permittivity functions of metals degrade the resonant properties of the nanoantenna, and the large ohmic losses limit the relative propagation lengths of SPP waves along the interface between such metals and dielectric materials. These drawbacks constrain the functionality of nanoantennas based on metals.

Recently, graphene, an attractive two-dimensional (2D) carbon material, has attracted great research interest in the last decade [5, 6]. Since its density-of-states and Fermi energy can be tuned by electrostatic or chemical doping, graphene has become a fantastic material for applications, including frequency multipliers [7], optical switches [8] and filters [9, 10]. Though some interesting initial theoretical and experimental studies have been presented [11-13], the use of graphene in log-periodic nanoantennas has been by far less investigated. Compared with the conventional plasmonic metal, graphene exhibits several appealing properties. For example, the permittivity of graphene can be easily tuned by gating voltage [13, 14]. Meanwhile the

Ohmic loss is low at a high doped level. Besides, graphene plasmons are confined to volumes ~ 106 times smaller than the diffraction limit which facilitates the light-matter interaction. Thereby, nanoantennas based on graphene have several advantages over metal nanoantenna. Here, we propose a graphene log-periodic nanoantenna and systematically investigate the field enhancement and the radar cross section of graphene log-periodic nanoantenna by adopting a log-periodic model with variable permittivity.

STRUCTURE AND FORMULATIONS

The configuration of the self-standing graphene log-periodic nanoantenna illuminated by an x-polarized plane wave is presented in Fig. 1. The antenna is based on the bowtie antenna with a flare angle of 30° . The angle of teeth spread on both sides of the bowtie is defined as 15° . The n th tooth is characterized by an outer radius R_n and inner radius r_n , where $r_n/R_n = 0.86$, $R_{n-1}/R_n = 0.74$ the maximum outer radius being 1000 nm. And the teeth number n is fixed at 3. The gap between the two teathed structures is 50 nm. The tips of the two circular-toothed structures are rounded off with a radius of curvature of 5 nm to account for fabrication imperfection.

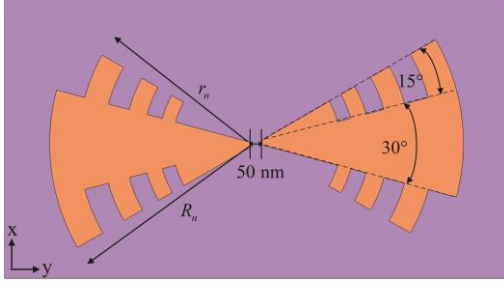


Fig. 1 Sketch of the graphene log-periodic nanoantenna

$$\sigma(\omega, \mu_c, \Gamma, T) = -\frac{ie^2(\omega + i2\Gamma)}{\pi\hbar^2} \left[\frac{1}{(\omega + i2\Gamma)^2} \times \int_0^\infty \varepsilon \left(\frac{\partial f_d(\varepsilon)}{\partial \varepsilon} - \frac{\partial f_d(-\varepsilon)}{\partial \varepsilon} \right) d\varepsilon - \int_0^\infty \left(\frac{f_d(-\varepsilon) - f_d(\varepsilon)}{(\omega + i2\Gamma)^2 - 4(\varepsilon/\hbar)^2} \right) d\varepsilon \right] \quad (1)$$

Where $f_d = \left\{ \exp\left[\frac{\varepsilon - \mu_c}{k_B T}\right] + 1 \right\}^{-1}$ and k_B are the Femi-Dirac distribution function and the Boltzmann constant, respectively. carrier scattering rate is set as $\Gamma = 0.43$ meV. It should be noted that the surface conductivity of the graphene sheet can be represented in a Drude-like form contribution by the random-phase approximation. The intraband contribution is given by

$$\sigma(\omega) = \frac{2e^2}{\pi\hbar} \frac{k_B T}{\hbar} \ln \left[2 \cosh \left[\frac{\mu_c}{2k_B T} \right] \right] \frac{i}{\omega + i\tau^{-1}} \quad (2)$$

In the terahertz frequency range, the intraband contribution dominates. Here ω is the angular frequency, e is the charge of electron, \hbar is the reduced Planck constant, and τ is the relaxation time. Here, the temperature is assigned the value of $T = 300$ K.

The graphene layer used here has a very small thickness d . The volume conductivity σ_v can be given by the equation $\sigma_v = \sigma_s/d$, where σ_s is the surface conductivity. From the time-harmonic Maxwell equations, the expression of the relative bulk permittivity of monolayer graphene can be obtained by

$$\varepsilon_v(\omega) = 1 - i\sigma_v(\omega)/\varepsilon_0\omega \quad (3)$$

The surface conductivity of an infinite graphene film is calculated by the Kubo formula [15, 16] as a function of the frequency (ω), chemical potential (μ_c), carrier scattering rate Gamma (Γ) and temperature (T):

Where ε_0 is the vacuum permittivity. In the calculation, d is assumed to be 1 nm. The modified Drude dielectric of graphene is fitted to a particular frequency range of 4-21 THz. And a comparison of the fitted Drude model to the theory values is shown in Fig. 2. The solid dots are the real part and the open circles are the imaginary part of the modified Drude fitting. In detailed, the real and imaginary part of the Drude fitting dielectric constant of graphene with different chemical potential is shown in Fig. 3.

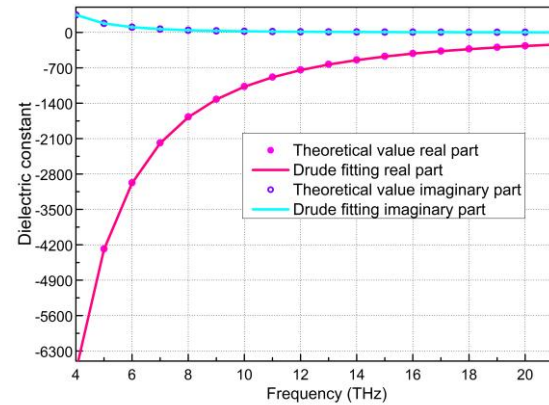
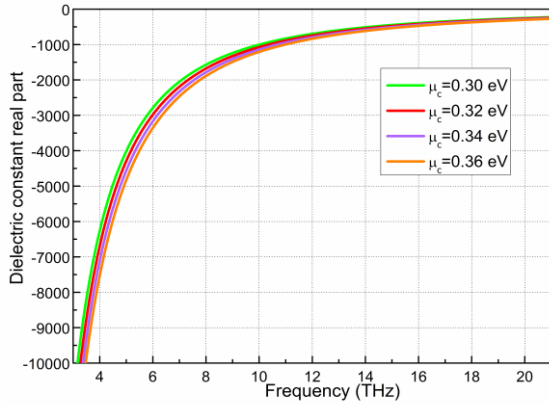


Fig. 2 Real and imaginary part of the dielectric data for graphene with chemical potential. The solid line is the theory value and the dot line is the modified Drude fitting.

(a)



(b)

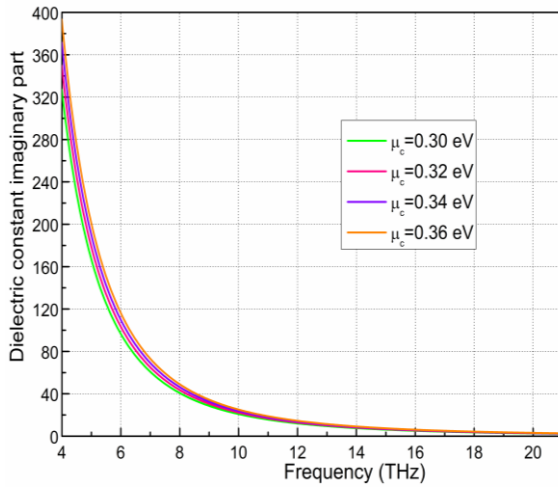


Fig. 3 The Drude fitting dielectric constant real part (a) and imaginary part (b) of graphene at different chemical potentials ($\mu_c = 0.30, 0.32, 0.34, 0.36$ eV)

To exactly analyze the theoretical description of radar cross-section, the total radar cross-section is defined as the ratio of the scattered power to the intensity of the incident plane wave, namely

$$\sigma_{RCS} = \lim_{R \rightarrow \infty} 4\pi R^2 \frac{|E_s|^2}{|E_0|^2} \quad (4)$$

Where, E_s and E_0 are the scattered and incident fields, respectively. R is the distance from the observation point to the antenna.

RESULTS AND DISCUSSION

Initially, the dependence of the field enhancement on the chemical potential is investigated for a graphene log periodic nanoantenna as seen in Fig. 4. Similar to

metal log periodic nanoantenna, one can identify several peaks in the field enhancement spectra. As expected from the metal log periodic nanoantenna, the log periodic nanoantenna based on graphene also allows for a systematic widening of the wavelength bandwidth. It can be easily found that the second and the third resonances are blue-shifted when the chemical potential increases from 0.30 eV to 0.36 eV. In addition, it is worth noticing that the resonant properties of the graphene log periodic nanoantenna can be turned by means of adjusting the chemical potential.

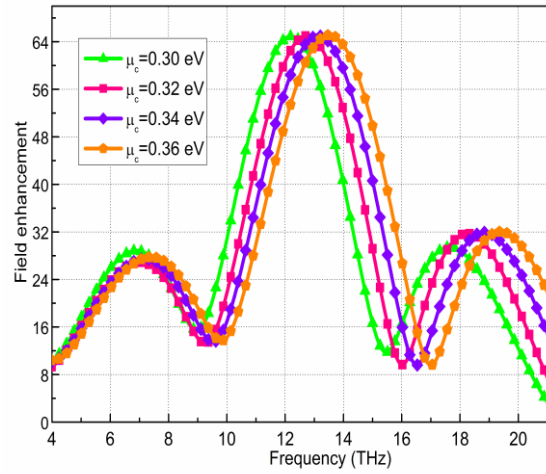


Fig. 4 The field enhancement with respect to the incident field at the center of the graphene nanoantenna with the chemical potential varying from 0.30 eV to 0.36 eV.

To understand the multi-resonant peaks mechanism of the field enhancement spectra, we calculated the near field distribution of the nanoantenna at frequency of every peak shown in Fig. 5 (a)-(c). The three main resonance peaks appear at 7, 12.7 and 18.3 THz. According to our simulations, the maxima amplitude of the near fields occurs at 9.7 THz shown in Fig. 4 (a). This phenomenon is due to the strong localized surface plasmon resonance of the graphene material and local field enhancement in the gap region. On the other hand, it can be seen that the local field enhancement region shifts from the ends of the nanoantenna toward its center as the frequency increases. This can be explained by the multi-resonant properties of the graphene log-periodic nanoantenna having multiple teeth with different lengths, which lead to the antenna to exhibit multi-resonant characteristic. As the local field enhancement associated with considerable field enhancement is formed in the gap region of all the near field images.

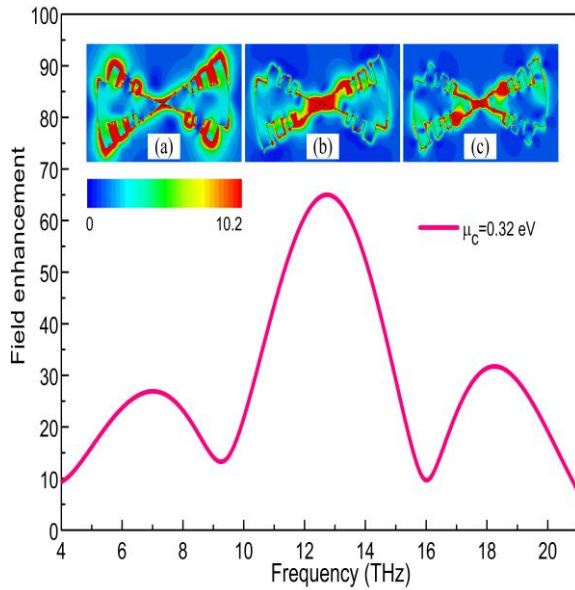


Fig. 5 Field enhancement spectrum of the graphene nanoantenna, the resonances are indicated. (a)-(c) the response fields in the middle cross-section at the frequency of 7/12.7/18.3 THz, respectively.

In order to find the electromagnetic field scattered by the graphene nanoantenna, the total radar cross-section is plotted for various values of chemical potential. Fig. 6 shows a clear evidence of a trend described above, where the resonant wavelength exhibits a blueshift with the increase of the chemical potential. The blueshift is due to the increase of the resonant frequency, which is effected by the chemical potential. And for different chemical potential from top to bottom, the peak values increase due to the radiated power increased caused by the increase of resonant frequency, which is influenced by the chemical potential mentioned above. These results suggest that, by adjusting the chemical potential of the graphene, the radiation properties of the graphene nanoantenna can be tuned in a wide spectral range, which provide additional degrees of freedom in optical device design.

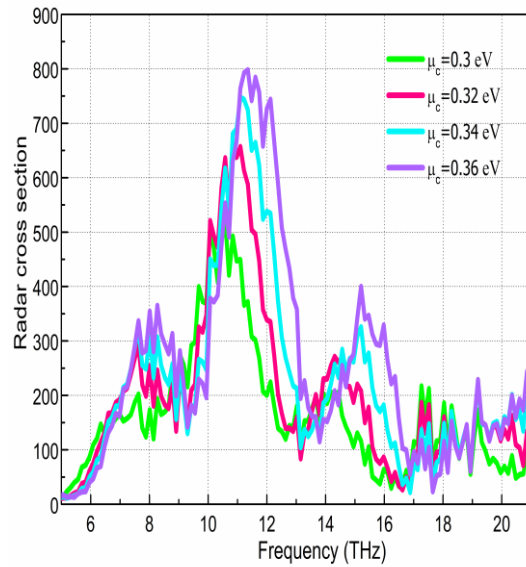


Fig. 6 The radar cross-section spectrum of a graphene log-periodic nanoantenna with chemical potential value ranged from 0.30 eV to 0.36 eV, which shows a blueshift of the resonant wavelength with the increase of the chemical potential.

CONCLUSION

A numerical simulation to the optical properties of optical nanoantenna based on graphene has been completed. Field enhancement and radar cross-section of the nanoantenna have been analyzed and their spectra have been evaluated versus different chemicals potential of graphene. It has been shown that the graphene optical nanoantenna creates a hot spot in the gap region and offer multi-resonant peak field enhancement. To be more specific, the resonant region shifts from the end of the graphene antenna to its center, when the resonant frequency increases. Specially, the field enhancement resonant spectrum can be easily tuned by changing the chemical potential of the graphene. In addition, an increase of the chemical potential result in an increase of the peak and a slight blueshift of the radar cross section spectrum. These results show that graphene is ready to play a unique role for controllably the resonant properties of optical nanoantenna, leading to applications such as sensing and enhanced quantum emission.

ACKNOWLEDGMENT

This work is supported by the National Natural Science Foundation of China (No. 61475084), and the Fundamental Research Funds of Shandong University (No. 2014JC032).

REFERENCE

- N. Liu, M. L. Tang, M. Hentschel, H. Giessen and A. P. Alivisatos. *Nature Mater* 10, 631 (2011).
- T. Hanke, G. Krauss, D. Träutlein, B. Wild, R. Bratschitsch and A. Leitenstorfer. *Phys Rev Lett* 103, 257404 (2009).
- H. G. Frey, S. Witt, K. Felderer and R. Guckenberger. *Phys Rev Lett* 93, 200801 (2004).
- H. A. Atwater and A. Polman. *Nature Mater* 9, 205 (2010).
- K. S. Novoselov, V. Fal, L. Colombo, P. Gellert, M. Schwab and K. Kim. *Nature* 490, 192 (2012).
- W. B. Lu, W. Zhu, H. J. Xu, Z. H. Ni, Z. G. Dong and T. J. Cui. *Opt Express* 21, 10475 (2013).
- H. Wang, D. Nezich, J. Kong and T. Palacios. *Electron Device Letters, IEEE* 30, 547 (2009).
- J.-S. Gómez-Díaz and J. Perruisseau-Carrier. *Opt Express* 21, 15490 (2013).
- H.-J. Li, L.-L. Wang, J.-Q. Liu, Z.-R. Huang, B. Sun and X. Zhai. *Appl Phys Lett* 103, 211104 (2013).
- J. H. Lee, C. Y. Koh, J. P. Singer, S. J. Jeon, M. Maldovan, O. Stein and E. L. Thomas. *Adv Mater* 26, 532 (2014).
- I. Llatser, C. Kremers, D. N. Chigrin, J. M. Jornet, M. C. Lemme, A. Cabellos-Aparicio and E. Alarcón In *Characterization of Graphene-Based Nano-Antennas in the Terahertz Band, Antennas and Propagation (EUCAP), 2012 6th European Conference on, 2012; IEEE: pp 194.*
- S. Thongrattanasiri and F. J. G. de Abajo. *Phys Rev Lett* 110, 187401 (2013).
- Y. Yao, M. A. Kats, P. Genevet, N. Yu, Y. Song, J. Kong and F. Capasso. *Nano Lett* 13, 1257 (2013).
- K. S. Novoselov, A. K. Geim, S. Morozov, D. Jiang, Y. Zhang, S. Dubonos, I. Grigorieva and A. Firsov. *Science* 306, 666 (2004).
- L. Falkovsky and S. Pershoguba. *Phys Rev B* 76, 153410 (2007).
- G. W. Hanson. *Antennas and Propagation, IEEE Transactions on* 56, 747 (2008).

SYNTHESIS OF SILVER NANOPARTICLES USING THE MEDICINAL PLANT *Pterocarpus marsupium* AND EVALUTION OF ITS ANTIMICROBIAL ACTIVITES

Parvathy, S^{1*} and Venkatraman, B.R^{2**}

¹Department of Chemistry, Government Arts College (Autonomous), Salem-636 007, Tamil Nadu, India.

²PG & Research Department of Chemistry, Periyar E.V.R.College (Autonomous), Tiruchirappalli-620 023, Tamil Nadu, India.

Abstract

A green synthesis route for the production of silver nano particles (AgNPs) using methanol extract from *Pterocarpus marsupium* (PM) is reported in the present investigation. The AgNPs were synthesized by reacting PM (as capping as well as reducing agent) with AgNO₃. The synthesized AgNps were characterized using UV-visible spectroscopy (UV-vis), Fourier Transform Infrared spectroscopy (FTIR), powder X-ray diffraction (XRD), and transmission electron microscopy (TEM). The results showed that the time of reaction, temperature and volume ratio of PM to AgNO₃ could accelerate the reduction rate of Ag⁺ and affect the AgNps size and shape. The NPs were found to be about 60 nm in size, mono-dispersed in nature, and spherical in shape. The formation and the crystalline nature of the synthesized nanomaterial were confirmed by XRD and TEM analyses. Further, these nanoparticles were found to exhibit high antibacterial activity against two different strains of the bacteria *Escherichia coli* (Gram negative) and *Staphylococcus aureus* (Gram positive).

Keywords: silver nanoparticles; *Pterocarpus marsupium*, TEM, AFM, XRD, antibacterial activity

INTRODUCTION

In the recent decades, medicinal plants played a significant role in traditional medicines as well as in modern medicinal chemistry. The health care product incorporated with the medicinal herbal offers a valuable impact to the commercialization in the market [1]. Recently, synthesis of engineered nano particles without using toxic chemicals is an emerging practice in nano science and nanotechnology [2]. However, among all other metal nano particles, gold and silver have gained much attention towards researchers from the past few years. In particular, Silver is a one such metal which has long been documented for its strong antimicrobial activity from the ancient days [3]. More commonly, Human beings are often infected by microorganisms such as bacteria, molds, yeasts, and viruses in their living environment. To protect them from the contagions, the urgency to develop effective

therapeutic agents is tremendously increasing in medicinal chemistry.

For the past decades, very deepest investigation over the antibacterial activity of material containing various natural and inorganic substances has intensively been explored in order to enhance the usefulness of the substance more effectively [4] [5]. Therapeutically, the topical ointments containing either silver metal or silver nano particles are the most important healing material to prevent infection against burn and open wounds [6]. Very recently, based on the Ayurvedic literature, Bala Chandra Prathab et al has reviewed the plant, namely *Pterocarpus marsupium* to investigate their phytochemical and pharmacological activity [7]. Basically, the respective plants are coming under the group called Rasayana in Ayurvedic system of medicine. Evidently, these rasayana drugs are actively as immune-modulator and relieve stress in

Corresponding Authors' Emails: * paruchem70@gmail.com, **brvenkatraman@yahoo.com

the human body [8]. In this connection, in order to make use of medicinal plant, in this paper, we demonstrated the synthesis of silver nano particles using the leaves of *Pterocarpus marsupium* and they are subjected to their antibacterial study.

EXPERIMENTAL

Healthy and fresh leaves of the plant *Pterocarpus marsupium* (PM) were collected in the early morning from Yercaud in Salem District, Tamil Nadu, India, in April 2014. All the chemicals and reagents were of analytical grade and were used as received without further purification. All glassware was washed with chromic acid and rinsed thoroughly with double-distilled water prior to use and dried in a hot air oven. All solutions were freshly prepared using double-distilled water and kept in the dark to avoid any photochemical reactions.

Preparation of *Pterocarpus marsupium* leaf extract

The plant was identified and it was authenticated with vouch specimen by Rapinant Herbarium, St. Joseph'College, Trichy, Tamilnadu, India. The collected plant leaves, washed several times in distilled water to remove the dust particles and shade-dried for fifteen days to remove the moisture. The shade dried plant material was powdered using a mixer grinder and that the powder was subjected to Soxhlet extraction with hexane, ethyl acetate, methanol and distilled water (60°C) for 24 hrs. Each solvent extract was distilled and condensed at 40°C. The condensed extract was stored at room temperature in airtight bottles and used for phytochemical analysis and green synthesis of AgNps using silver nitrate.

Phytochemical analysis of leaf extract

Preliminary phytochemical analysis was carried out qualitatively for various solvents such as hexane, ethyl acetate, methanol and water extracts of PM as per standard methods. Phytochemicals such as alkaloids, flavonoids, steroids, terpenoids, anthraquinones, phenols, saponins, tannins, carbohydrates, oils and resins were investigated.

Synthesis of silver nanoparticles

For the reduction Ag^+ ions, 1mM AgNO_3 was added to the PM plant leaf extracts to make up a final solution 200mL and centrifuged at 2,000rpm for 10 min. The supernatants were heated at 100°C. A change in the color of solutions was observed during the heating process.

Characterization

The prepared PM AgNps were characterized by UV-visible (UV-vis), X-ray Diffraction (XRD), Fourier-transform infrared spectroscopy (FTIR), Transmission electron microscopy (TEM) and Atomic force microscope (AFM) study. UV-vis spectral analysis was done using Elico spectrophotometer at a resolution of 1nm from 300 to 750nm. FT-IR spectral analysis carried out using a Perkin-Elmer spectrometer FTIR Spectrum in the range 4000–400 cm^{-1} . The structures of SEAgNps produced were examined by XRD (XRD-6000, Shimadzu) XRD patterns were recorded at a scan speed of 4°/ minute. TEM analysis was done using JEOL JEM 100SX TEM at an accelerating voltage of 80kv. The PMAgNps were visualized with an AFM. A thin film of the sample was prepared on a glass slide by dropping 100 μL of the sample on the slide, and was allowed to dry for 5 min. The slides were then scanned with the AFM (Nanosurf AG, Switzerland, Product: BT02089, v1.3R0). Nanosurf Easyscan-2 software was used for the AFM analysis. Antibacterial activities of the synthesized PMAgNps were evaluated against twenty bacterial strains by disc diffusion method [37]. *In-vitro* antibacterial activity was screened by using Muller Hinton Agar (MHA) obtained from Hi-media (Mumbai). The MHA plates were prepared by pouring 15mL of molten media into sterile petri plates. The plates were allowed to solidify for a few minutes, 0.1% inoculums suspension was swabbed uniformly and the inoculums were allowed to dry for five minutes. The concentration of PMAgNps (40mg/disc) was loaded on 6mm sterile disc. The loaded disc was placed on the surface of the medium, the PMAgNps was allowed to diffuse for five minutes and the plates were kept in incubation at 37°C for 24h. At the end of incubation, inhibition zones formed around the disc were measured with a transparent ruler in millimeter.

RESULTS AND DISCUSSION

Phytochemical analysis

Phytochemical analysis of the plant extracts revealed the presence of phytochemicals, which are known to exhibit medicinal as well as physiological activities. The phytochemical investigation of PM extract (ethyl acetate, hexane, methanol and water) showed some differences (Table 1). Steroids were present in all the four solvent extracts of SE plant leaves have been reported to show antibacterial properties. While alkaloids are present in hexane, methanol and water extracts of PM plant leaves, but tannins are present only in methanol extract. While comparing the phytochemical activity of all the four solvent extracts of SE plant leaves and number of phytochemicals were present in hexane and water.

Characterization of silver nanoparticles

UV-visible spectrum study

Reduction of silver ions into silver nanoparticles during exposure to plant extracts was observed as a result of the color change. The color change is due to the Surface Plasmon Resonance (SPR) phenomenon. The metal nanoparticles have free electrons, which give the absorption SPR absorption band, due to the combined vibration of electrons of metal nanoparticles in resonance with light waves. A strong and broad peak, located at 534nm was observed for the synthesized PMAgNps in the UV-visible spectrum and this peak, assigned to a surface plasmon, is well documented for various metal nanoparticles with sizes ranging from 2 to 100 nm .

FT-IR spectrum study

FTIR measurements were carried out to identify the functional group in PM plant leaf extracts responsible for the reduction and capping of the bio-reduced AgNps. The FTIR spectrum of PMAgNps is represented (Fig. 1a&b) and prominent IR bands are observed at 3432, 2975, 2837, 2362, 2301, 2072, 1641, 1386, 1028, 578, 420cm⁻¹. A sharp band at 3432cm⁻¹ reveals water and -OH absorption frequency. The sharp bands at and 2975 and 2887cm⁻¹ arises from C-H stretching modes. The absorption bands located at 1386 and 1028cm⁻¹ may be attributed to -C-O and -C-O-C stretching modes.

Powder X-ray diffraction study (XRD)

The figure (Fig.2) shows the XRD pattern of vacuum-dried AgNps synthesized using *Solanum erianthum*. The XRD pattern of PMAgNps indicated that the structure is face-centered cubic. In addition PMAgNps had a similar diffraction profile (Ag XRD ref No. 01-087-0719), and XRD peaks at 2 θ of 38.18°, 44.32°, 57.52°, 64.50° and 77.05° could be attributed to the 111, 200, 103, 220 and 311 crystallographic planes of the face-centered cubic silver crystals, respectively. The XRD pattern thus clearly illustrated that the PMAgNps formed in this study is crystalline in nature.

TEM analysis

The dried AgNps prepared from SE plant leaves extract were taken in the preparation of Transmission Electron Microscopic (TEM) analysis. TEM images of PMAgNps dispersed on a TEM copper grid (a, scale bar: 30 nm). The TEM picture shows an individual PMAgNps as well as a group of crystals in clusters of aggregates which is represented by the TEM micrograph (Fig. 3). The morphology of PMAgNps is slightly variable from spherical to triangular in shape in the photomicrograph. Under these observations, these PMAgNps were found to be in the size range of 20 to 50 nm. TEM image is shown in figure (Fig.3) which clearly indicates that PMAgNps were spherical in shape, having an average size of 50 nm and the particles in this range are well known for having excellent antimicrobial activity.

AFM study

Surface topology of the synthesized PMAgNps was studied by atomic force microscopy (AFM) analysis (Fig. 4) which confirms the spherical shape of the particles and again the tendency of particles to aggregate. The micrograph clearly indicates that the synthesized PMAgNps possess spherical shape and have the calculated sizes in the range of 20 to 50nm.

Antibacterial activity

The antibacterial activity was performed against nine Gram-positive and nine Gram-negative bacterial pathogens using synthesized PMAgNps of three solvents (methanol, ethyl acetate and distilled water). The most significant effect of distilled water and ethyl acetate mediated PMAgNps showed against *Shigella boydii* and its zone of inhibition is 32 mm

and 23mm respectively, than that of the control which showed only 18mm.

Table 1: Phytochemical activity of *Pterocarpus marsupium*

Phytochemicals	Extracts			
	Hexane	Ethyl acetate	Hydro Alcohol	Aqueous
Alkaloids				
Mayer's test	-	-	+	+
Wagner's test	-	-	+	+
Flavonoids				
Lead acetate test	+	+	+	+
H ₂ SO ₄ test	-	+	+	+
Steroids				
Liebermann-Burchard test	-	+	-	-
Terpenoids				
Salkowski test	-	-	+	-
Arthroquinone				
Borntrager's test	-	-	-	-
Phenols				
Ferric chloride test	-	+	+	-
Lead acetate test	-	+	+	-
Saponins				
Tannins	-	+	+	-
Carbohydrates				
Oils & Resins	+	+	-	+

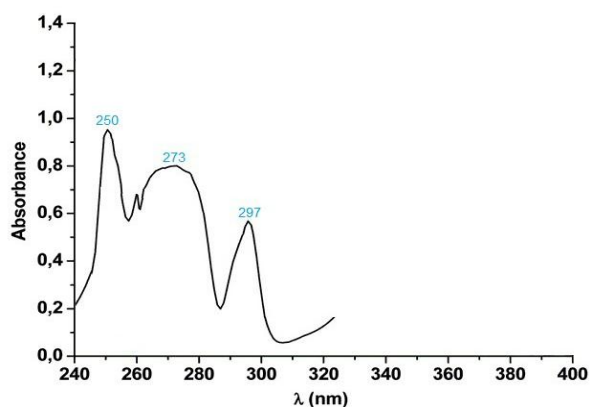


Fig 1: UV-Vis spectrum of synthesized PMAgNPs

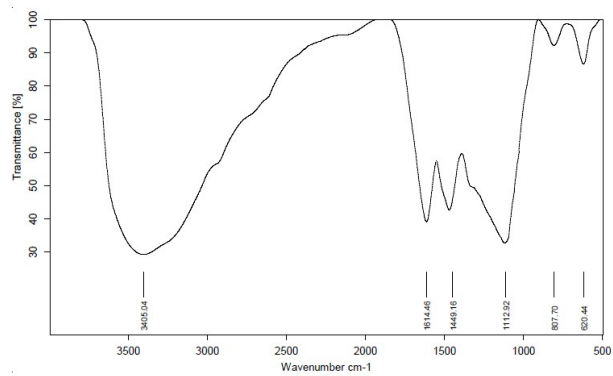


Fig.2: FTIR spectrum of synthesized PMAgNPs

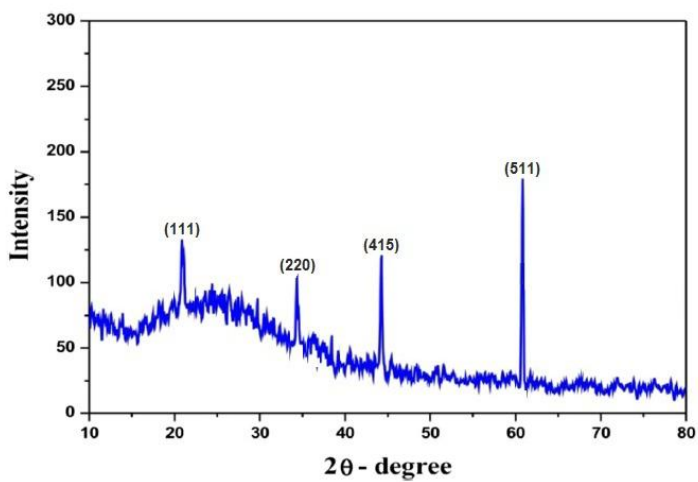


Fig.3: XRD pattern of synthesized PMAgNPs

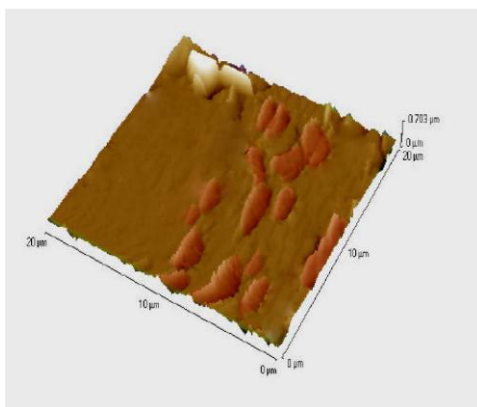


Fig.4: AFM Image of synthesized PMAgNPs

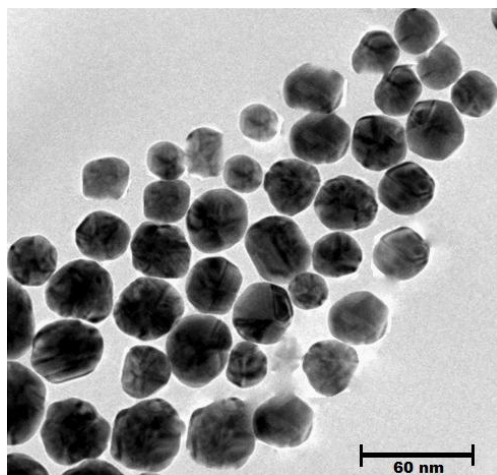


Fig 5: TEM image of synthesized PMAgNPs

REFERENCES

- [1] Calixto J.B., Efficacy, safety, quality control, marketing and regulatory guidelines for herbal medicines (phytotherapeutic agents), *Brazilian Journal of Medical and Biological Res.*, 2000, 33: 179-189.
- [2] Whitesides, G.M., *Nat. Biotechnol.*, 2003, 21, 1161-1165.
- [3] Lok, C.N., Ho, C.M., Chen, R., He, Q.Y., Sun, H., Tam, P.K., Chiu, J.F. and Che, C.M., *Silver nanoparticles: partial oxidation and antibacterial activities*, *J. Biol. Inorg. Chem.*, 2007, 12(4): 527-534.
- [4] Kim TN, Feng QL, Kim JO, Wu J, Wang H, Chen GC, et al. Antimicrobial effects of metal ions (Ag^+ , Cu^{2+} , Zn^{2+}) in hydroxyapatite. *J. Mater. Sci. Mater. Med.*, 1998; 9:129-34.
- [5] Cho KH, Park JE, Osaka T, Park SG. The study of antimicrobial activity and preservative effects of nanosilver ingredient. *Electrochimica Acta* 2005; 51: 956- 60.
- [6] Ip, M., Lui, S.L., Poon, V.K.M., Lung, I. and Burd, A., 2006, *Antimicrobial activities of silver dressings: An in vitro comparison*, *J. Med. Microbiol.*, 55, 59-63.
- [7] Bala Chandra Prathab, S., Ranjitha, B., Anusha, C.H., Nagasirisha, M., Madhusudhana Chetty, C. and Mohamed Saleem, T.S., *Pterocarpus marsupium Roxb.: A potent herb for life threatening diseases*, *Int. J. Res. Phytochem. Pharmacol.*, 2012, 2(2), 75-83.
- [8] Gariola, S., Gupta, V., Singh, B., Maithani, M., Bansal, P., *Phytochemistry and pharmacological activities of Pterocarpus marsupium- A Review*, *IRJP*, 2010, 1(1), 100-104.

PHOTOVOLTAIC PERFORMANCE OF CaCO₃- COATED SnO₂-BASED DYE-SENSITIZED SOLAR CELLS WITH COMPOSITE LIQUID/QUASI- SOLID-STATE ELECTROLYTES

Wanninayake, W. M. N. M. B^{1,3*}, Premaratne, K^{1,3} and Rajapakse, R. M. G^{2,3}

¹ Department of Physics, University of Peradeniya, Peradeniya, 20400, Sri Lanka

² Department of Chemistry, University of Peradeniya, Peradeniya, 20400, Sri Lanka

³ Postgraduate Institute of Science, University of Peradeniya, Peradeniya, 20400, Sri Lanka

Abstract

As liquid electrolyte-based dye-sensitized solar cells (DSCs) have shown some practical limitations due to their sealing imperfections, leakage and solvent evaporation, the composite liquid-gel system has become a subject of study. The composite electrolyte is expected to circumvent the above problems to a certain extent without a significant loss of efficiency compared to liquid electrolytes. This study focuses on a comparative study of DSCs-based on SnO₂/CaCO₃ composite system in which liquid, gel and liquid-gel electrolytes are employed separately. Our previous studies show that CaCO₃ acting as a coating layer on SnO₂ suppresses recombination in SnO₂-based DSCs resulting in higher efficiencies. In this study, we have attempted to examine the effect of using a liquid/gel composite as the electrolyte in SnO₂/CaCO₃ system. Our basic device structure was FTO/SnO₂/CaCO₃/D358 dye/electrolyte/lightly-platinized FTO counter electrode. The three different types of electrolytes mentioned above were used and their respective cell parameters were measured. The respective device efficiencies for Liquid-, liquid/gel- and gel- electrolytes were 5.50%, 5.30% and 5.00%. Their I₃⁻ ion diffusivities were 6.70 x 10⁻⁶ cm² s⁻¹, 3.00 x 10⁻⁶ cm² s⁻¹ and 0.39 x 10⁻⁶ cm² s⁻¹, respectively. The general trend of the results indicates that for SnO₂/CaCO₃-based DSCs there is no significant loss of efficiency due to the replacement of the liquid electrolyte by a pure gel-electrolyte or by a composite of the two. However, the use of a gel-based electrolyte could eliminate some of the practical limitations of the use of liquid electrolytes.

Keywords: Dye-sensitized solar cells, SnO₂/CaCO₃ composite system, liquid/gel composite system, diffusivity of triiodide ion, gel electrolyte, recombination

INTRODUCTION

Dye-sensitized Solar cells (DSCs) based on thin film nanocrystalline high band gap semiconductor material have received attention as an alternative to conventional single crystal silicon solar cells. Since the early development of DSCs by M. Grätzel in 1991, considerable effort has been devoted to improve their performance [1-4]. As the efficiency of the DSCs depend on many factors such as semiconductor material, sensitizer and electrolyte, this study focused on the development of the semiconductor material and electrolyte. In DSCs, TiO₂ is the most popular semiconductor material but

it shows some retarding effects due to its low electron mobility which leads to increase the dark current of the solar cell device. Also, photocatalytic ability of TiO₂ tends to degrade the dye molecules thus lowering the lifetime of the solar cell. Therefore, SnO₂ is employed in place of TiO₂ as it has ~250 cm² V⁻¹ s⁻¹ of electron mobility [5, 6]. The same property will contribute towards recombination through the surface trap levels. There are two major recombination processes present in DSCs. One is regeneration of excited dye molecules with the injected electrons. The other is combination of the injected electrons with the triiodide ions in the electrolytes due to the back tunneling of injected

Corresponding Author Email: *mihira.wanninayake@gmail.com

electrons. In order to overcome this recombination problem, here a CaCO₃ coating layer is employed on top of the SnO₂ semiconductor surface [7-10].

Generally, liquid-, gel polymer- and solid-electrolytes are used when the DSCs are fabricated. Liquid electrolyte based solar cells suffer from some practical limitations such as solvent evaporation, leakage and sealing imperfections despite their higher performance. Also, solid electrolytes show inferior performance due to poor wetting ability of the semiconductor network and low conductivity. Therefore, application of gel polymer electrolyte in DSCs has become important due to its cohesive nature of a solid and diffusive nature of a liquid. The use of gel electrolyte will sacrifice the performance of the DSCs to certain extent due to low ion mobility. In order to avoid these drawbacks associated with the gel electrolyte, this study focused on the use of the composite liquid/gel electrolytes.

EXPERIMENTAL

Preparation of gel electrolyte

The plasticized gel electrolyte was prepared by mixing 0.225 g of polyacrylonitrile (Aldrich), 0.525 g of ethylene carbonate (Aldrich 98%), 0.750 g of propylene carbonate (Sigma-Aldrich 99%), 0.152 g of tetrapropylammonium iodide (Aldrich 98%) and 0.020 g of iodine (Aldrich 99%). Then the electrolyte was stirred at 80 °C, until the mixture turned into a clear, homogeneous, viscous gel. Next, the hot gel electrolyte was pressed, by sandwiching it between two clean glass plates to obtain a free-standing polymer film and then it was subsequently dried in a vacuum desiccator overnight, at room temperature, to remove any absorbed moisture.

Preparation of working electrode

Colloidal SnO₂ (3.00 cm³, Alfa Aesar 15% in H₂O), acetic acid (10 drops, Aldrich 99.7%), Triton X-100 (3 drops, Lobachemie, Mumbai, India), 0.04 g of CaCO₃ (Aldrich 99%) and ethanol (40.0cm³, Sigma-Aldrich 99.8%) were mixed thoroughly and the resulting SnO₂/CaCO₃ suspension was sprayed onto a FTO glass plates at 150 °C. Then, samples were sintered at 500 °C for 30 minutes and allowed to cool down to 80 °C. Next, the samples were immersed in a dye solution (Indoline D358, 3.0x 10⁻⁴ M in 1:1

volume ratio of acetonitrile/tert-butyl alcohol) for 12 hours. Then the dye coated-SnO₂/CaCO₃ films were rinsed with acetonitrile to remove any physically adsorbed dye molecules. The gel electrolyte was subsequently sandwiched between the FTO/SnO₂/CaCO₃ working electrode and a lightly-platinized FTO counter electrode to assemble the solar cell device and then the commercial liquid was injected into the assembled device.

Characterizations

The film morphology and the performance of the solar cell device was studied using different characterization techniques. Crystallographic characterization of the composite SnO₂-based films was done by means of Powder X-ray diffraction (XRD) using a Siemens D5000 X-ray diffractometer with the Cu K_α radiation ($\lambda = 0.1540562$ nm) at a scan rate of 1° min⁻¹. The photovoltaic performance of the DSCs was measured by a solar simulator (PECCELL PEC-L01) with a source meter (Keithley 2400) at 25°C under AM 1.5 (100 mW cm⁻²) illumination. The total irradiated area of the DSCs was 0.25 cm². The Linear sweep voltammetric studies were carried out using an Autolab (PGSTAT12) at a scan rate of 1 mV s⁻¹ from +0.1 V to -0.6 V.

RESULTS AND DISCUSSION

XRD studies were conducted to examine the composite nature of fabricated film. Fig. 01 shows XRD spectra obtained for SnO₂/CaCO₃ composite system with the respective plane values. The SnO₂ (ICDD PDF 77-0451) peaks appear at 2 θ values of 26.62°, 54.91°, 58.29°, 61.81°. The presence of CaCO₃ (ICDD PDF 83-1762) in the composite system was verified by peaks at 2 θ values of 33.73°, 39.57° and 51.81°.

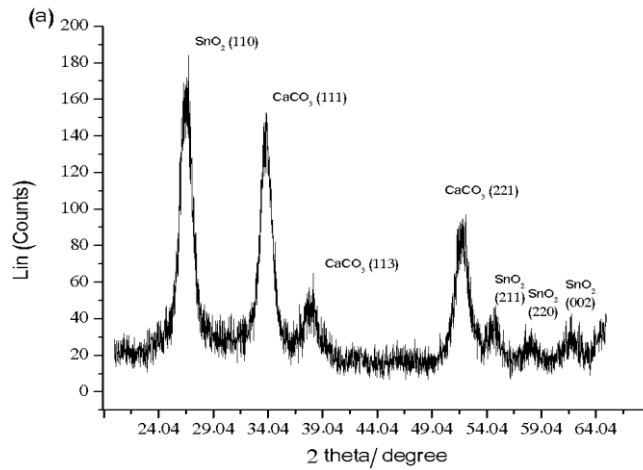


Fig. 01: XRD patterns of the composite SnO₂/CaCO₃ systems.

Linear sweep voltammetry measurements were conducted in order to study the diffusivity of I₃⁻ ions

in the electrolytes. The diffusivity values $D_{I_3^-}$ were calculated using equation (1) [11-13].

$$J_{lim} = \frac{2nF D_{I_3^-} c_{I_3^-}}{l}$$

(1) where F is the Faraday constant, J_{lim} is the limiting diffusion

current density, $c_{I_3^-}$ is the concentration of triiodide ions, n is the number of electrons involved in redox reaction and l is the distance between the two electrodes. The transport of I₃⁻ ions towards the cathode surface by diffusion and the rate of electron transfer reactions are the prominent factors which affect the current generation of the system. The calculated apparent diffusion coefficients of triiodide ions in the liquid-, gel- and liquid/gel-electrolytes are tabulated in the Table 01. We will utilize these data to explain the photovoltaic performance of DSCs fabricated using these electrolytes.

Table 01. Apparent diffusivity values of liquid-, gel- and liquid/gel-electrolytes.

Electrolyte	J _{lim} (x 10 ⁻⁴ A)	D _{I₃⁻} (x 10 ⁻⁶ cm ² s ⁻¹)
Liquid	10.2	6.70
Gel	0.55	0.39
Liquid/gel	4.57	3.00

According to the results obtained the gel electrolyte shows lowest diffusivity of triiodide ions. This might be due to the cohesive nature of the gel electrolyte. The composite liquid/gel system shows comparable triiodide diffusivity. This can be attributed to the filling of the pores in the gel by liquid electrolyte as the polymer network arrange in random manner when the formation of the gel electrolyte.

Table 02. Photovoltaic parameters of DSCs with liquid-, gel- and liquid/gel-electrolytes.

System	Electrolyte	J _{sc} (m A cm ⁻²)	V _{oc} (m V)	FF	Efficiency (%)
SnO ₂ /CaCO ₃	Liquid	14.7	704	0.550	5.50
	Gel	11.6	636	0.678	5.00
	Liquid/gel	13.3	637	0.625	5.30

SnO ₂	Liquid	9.1 4	490	0.35 0	1.60
	Gel	7.6 7	460	0.35 4	1.25

According to the results in Table 02, liquid electrolyte based composite SnO₂/CaCO₃ DSCs shows highest efficiency values with the highest short circuit current density and open circuit voltage values. Generally, SnO₂ based DSCs show low performance due to its high recombination property. By introducing an ultrathin outer layer of CaCO₃ on top of the SnO₂ nanocrystalline network, this recombination effect can be reduced to some extent. The results of the current density and voltage for the composite SnO₂/CaCO₃ DSCs can be explained as follows. The very fine outer layer of CaCO₃ on SnO₂ particles strongly adsorbs the D358 dye molecules and the electrons from photoexcited dye molecules will effectively tunnel through the coating layer and reach the conduction band of the SnO₂ while acquiring a lower energy. Then the back tunneling will be greatly reduced by the barrier layer according to equation (2).

$$T = \frac{16E}{V_0} \left(1 - \frac{E}{V_0}\right) e^{-2\alpha a} \quad (2)$$

where T is the tunneling transmission coefficient, V_0 is the barrier height, a is the barrier width and

$$\alpha = \frac{2m(V_0 - E)}{\hbar^2}$$

The coating layer formation and its action can be explained as follows. As the composite SnO₂/CaCO₃ system sinters at temperature of about 500 °C, CaCO₃ will sinter firmly onto the SnO₂ outer surface whereas their sintering each other is weak. Then the interconnected SnO₂ nanocrystalline network fully covered by interconnected CaCO₃ particles will supply a surface for adsorption of the dye molecules. The dye molecules are more strongly adsorbed and higher adsorbed dye amount onto CaCO₃ coating layer (5.1×10^{-5} mol L⁻¹ cm⁻²) than the SnO₂ surface (4.0×10^{-5} mol L⁻¹ cm⁻²) can be observed as the high isoelectric point of CaCO₃ (~11.0 pH) assists the dye adsorption. The outer shell firmly covered with dye molecules and coating layer will not allow

triiodide ions to penetrate through the barrier layer and reach into SnO₂ and recombine with injected electrons. The reduction of recombination will shift the Fermi level of SnO₂ upwards, as a result, the energy difference between the Fermi level and redox potential will increase thus increasing the VOC of the device. The bare SnO₂-based solar cell device gave a VOC value of about 470 mV, although the theoretical value lies of about 550 mV. However, presence of CaCO₃, the system showed VOC value around 700 mV. The very high VOC value can be considered to be due to the shifting of Fermi level above the conduction band of SnO₂ as a result of reduction of the recombination of the solar cell device.

The significant increase of JSC is possibly due to the following reasons. One is the reduction of recombination of the injected electrons with the oxidized dye molecules and the redox species in the electrolyte. Second is the boost of injected electrons due to the increase of adsorbed dye attachments. Third is fast generation of iodide ions at counter electrode which help regeneration of dye molecules due to the higher diffusivity.

The effect of the composite liquid/gel system is noteworthy. It shows 15% of significant increase of JSC with respect to the device which contains only gel electrolyte. As we employed same composite SnO₂/CaCO₃ system for the liquid-, gel-, liquid/gel-electrolytes, the only effect comes from the electrolyte for the variation of JSC. Since a gel electrolyte shows cohesive nature, it gave the lowest triiodide ion diffusivity. This will lead to slower generation of iodide ions at counter electrode and faster recombination of injected electrons with triiodide ions. When composite liquid/gel electrolyte is employed, liquid electrolyte will fill into the pores in the polymer network thus enhancing the diffusivity of triiodide. Also, this electrolyte system will lead to better wetting or contact with the semiconductor network. Perhaps first the liquid electrolyte fills into to the pores of the semiconductor network and then it covered by the gel electrolyte and thereby the liquid electrolyte will trap in the solar cell device without leakage.

CONCLUSIONS

We can conclude that the results we obtained imply the fact that the composite liquid/gel system gave a significant increase of performance compared to the device fabricated with pure gel electrolyte. The use of a gel-based electrolyte could eliminate some of practical limitations associated with the use of liquid electrolyte but the use of a gel electrolyte sacrifices the cell efficiency up to some extent. Employment of the composite liquid/gel electrolyte is expected to circumvent the problems such as leakage, solvent evaporation and sealing imperfections associated with liquid and drawbacks accompanied with gel electrolyte due to its low ion mobility, at once. The pores filling of the liquid electrolyte into the polymer network and tapping into the pore of nanocrystalline semiconductor network will help increase the JSC of the solar cell device. Suppression of back tunneling by barrier layer will also support to enhance the VOC of SnO₂/CaCO₃ composite system.

ACKNOWLEDGEMENT

Financial support from the National Research Council, Sri Lanka through research grant No:NRC 08-17 is gratefully acknowledged.

REFERENCES

- [1] B. O'Regan and M. Grätzel, "A low-cost, high-efficiency solar cell based on dye-sensitized colloidal TiO₂ films," *Nature*, 353 (1991) 737–740.
- [2] M. K. Nazeeruddin, A. Kay, I. Rodicio, R. Humphry-Baker, E. Mueller, P. Liska, N. Vlachopoulos, and M. Graetzel, "Conversion of light to electricity by cis-X2bis(2,2'-bipyridyl-4,4'-dicarboxylate)ruthenium(II) charge-transfer sensitizers (X = Cl-, Br-, I-, CN-, and SCN-) on nanocrystalline titanium dioxide electrodes," *J. Am. Chem. Soc.*, 115, (1993) 6382–6390.
- [3] P. Péchy, T. Renouard, S. M. Zakeeruddin, R. Humphry-Baker, P. Comte, P. Liska, L. Cevey, E. Costa, V. Shklover, L. Spiccia, G. B. Deacon, C. A. Bignozzi, and M. Grätzel, "Engineering of Efficient Panchromatic Sensitizers for Nanocrystalline TiO₂-Based Solar Cells," *J. Am. Chem. Soc.*, 123 (2001) 1613–1624.
- [4] A. Hagfeldt and M. Grätzel, "Molecular Photovoltaics," *Acc. Chem. Res.*, 33 (2000) 269–277.
- [5] Z. M. Jarzebski, "Physical Properties of SnO₂ Materials," *J. Electrochem. Soc.*, 123 (1976) 299.
- [6] H. Wang, B. Li, J. Gao, M. Tang, H. Feng, J. Li, and L. Guo, "SnO₂ hollow nanospheres enclosed by single crystalline nanoparticles for highly efficient dye-sensitized solar cells," *CrystEngComm*, vol. 14 (2012) 5177.
- [7] W.M. N.M.B. Wanninayake, K. Premaratne, G.R.A. Kumara and M. Karunaratne, "Quasi-Solid State SnO₂/CaCO₃ Solar Cells Sensitized with Indoline D-358 Dye," *PURSE*, 2011.
- [8] K. A. T. A. Perera, S. G. Anuradha, G. R. A. Kumara, M. L. Paranawitharana, R. M. G. Rajapakse, and H. M. N. Bandara, "The interconnected CaCO₃ coated SnO₂ nanocrystalline dye-sensitized solar cell with superior performance," *Electrochim. Acta*, 56 (2011) 4135–4138.
- [9] W.M.N.M.B. Wanninayake, K. Premaratne, G.R.R.A. Kumara, R.M.G. Rjapakse, "A Study of the Efficiency Enhancement of the Gel Electrolyte-based SnO₂ Dye-sensitized Solar Cells Through the Use of Thin Insulating Layers", *Electrochimica Acta* (2016) inpress.
- [10] S. Lee, J. Y. Kim, S. H. Youn, M. Park, K. S. Hong, H. S. Jung, J. Lee, and H. Shin, "Preparation of a Nanoporous CaCO₃-Coated TiO₂ Electrode and Its Application to a Dye-Sensitized Solar Cell," 18 (2007) 11907–11910.
- [11] F. Fabregat-Santiago, J. Bisquert, E. Palomares, L. Otero, D. Kuang, S. M. Zakeeruddin, and M. Gratzel, "Correlation between Photovoltaic Performance and Impedance Spectroscopy of Dye-Sensitized Solar Cells Based on Ionic Liquids," *J. Phys. Chem. C*, 111 (2007) 6550–6560.
- [12] A. Hauch and A. Georg, "Diffusion in the electrolyte and charge-transfer reaction at the platinum electrode in dye-sensitized solar cells," *Electrochim. Acta*, vol. 46 (2001) 3457–3466.
- [13] W.M.N.M.B. Wanninayake, K. Premaratne, G.R.R.A. Kumara, R.M.G. Rjapakse, "Use of Lithium iodide and tetrapropylammonium iodide in Gel Electrolytes for Improved Performance of Quasi-solid-state Dye-sensitized Solar Cells: Recording an Efficiency of 6.40%", *Electrochimica Acta* (2016) inpress

EFFECT OF ACID ON NANOVANADIUM OXIDE

Phetmung, H^{1*}, Prompakdee, S² and Kong rat, P³

^{1,2} *Inorganic and Materials Chemistry Research Unit, Department of Chemistry, Thaksin University, Amphur Muang, Songkhla, 90000, Thailand*

³ *Department of Physics, Faculty of Science, Thaksin University, Amphur Muang, Songkhla, 90000, Thailand*

Abstract

The facile hydrothermal synthesis of two vanadium oxide nanostructure compounds (**1**) and (**2**) were synthesized using the 2:1:400 mol ratio of ammonium metavanadate (NH₄VO₃), zinc acetate dihydrate [Zn(CH₃COO)₂·2H₂O] and water in the present of hydrochloric for compounds (**1**) and acetic acid for compounds (**2**) to adjust the pH of the solution to 3. The structure, morphology and composition of the as-synthesized products were characterized by field emission scanning electron microscopy (SEM), powder X-ray diffraction (XRD), Thermogravimetric analysis (TGA) and differential thermal analysis (DTG) measurement and Fourier transform infrared spectroscopy (FT-IR). SEM images show the nanobelt morphology of (**1**) and flower like nanobelt morphology of (**2**) with length of 3–6 micrometers in (**1**) and several tens of micrometers in (**2**) respectively. Their XRD patterns reveal the set of 1D vanadium oxide nanobelts, characteristic of (001) reflections. Based on FT-IR, XRD and TGA results, the chemical formulae of the as-obtained nanobelt (**1**) and flower like nanobelt (**2**) are the family of NH₄V₄O₁₀•nH₂O.

Keywords: hydrothermal synthesis, 1 D nanostructure, vanadium oxide nanobelt, flowerlike nanobelt, acid effect

INTRODUCTION

Over a few decades, vanadium oxide and its derivative compounds have been a great research interest as a new class of quasi-one-dimensional inorganic nanostructures (1D) (Liu et al., 2004; O'Dwyer et al., 2006; Chang et al., 2007; Xu et al., 2004; Wu et al., 2004). This is because of their properties that differ from those of zero-dimensional structures. The physical properties of these inorganic nanostructures fundamentally related to their sizes and morphologies, such as nanobelt (Lui et al., 2005; Yua et al., 2006; Zhang et al., 2006; Chang et al., 2007; Wang et al., 2008, nanoribbon (Kong et al., 2004; Maa et al., 2009), nanowire (Wu et al., 2004; Wang et al., 2008, nanorod (Xu et al., 2004), nanotube (O'Dwyer et al., 2006; (O'Dwyer et al., 2007; Pillai et al., 2000), nanofibre (Lutta et al., 2005), nanobundle (Wang et al., 2008) and nanoflower (Parida et al., 2011; Maa et al., 2009). These nanomaterials have been demonstrated to exhibit electrochemical (O'Dwyer et al., 2007; Lutta et al., 2005; Wang et al., 2011; Zhang et al.,

2009), 4,6,8,12,14,16,21,22 conductivity (Wang et al., 2008; Chernova et al., 2009; Stanley Whittingham et

al., 2004), magnetic (Parida et al., 2011; Fei et al., 2008), optical properties (Parida et al., 2011) and their special potential applications in the design of advanced nanodevices (Lui et al., 2005; Wang et al., 2008).

One of the most challenges in synthetic work is how to control their sizes and morphologies in a precise manner. Although several techniques have been successfully applied such as hydrothermal synthesis (Law et al., 2004; Lin et al., 2010; Zhang et al., 2006), sol-gel (O'Dwyer et al., 2007; Lutta et al., 2005; Spahr et al., 1999) and rheological phase reaction method (Lin et al., 2010). Among them, hydrothermal synthesis proves as a promising methodology.

However, the condition of hydrothermal process has also been widely concerned. To observe the growth on the size and morphology mechanism, one used

Corresponding Author Email: *tayaphetmung@yahoo.com

technique is the hydrothermal reduction method using acid as the reducing agent (O'Dwyer et al., 2006; Parida et al., 2011; Fei et al., 2008). An example is the $(\text{NH}_4)0.5\text{V}_2\text{O}_5$ nanobelt which is synthesized using hydrochloric acid gave the 50–200 nm in diameter and several micrometers in length (Wang et al., 2011). Hydrothermal method in the present of hydrochloric acid at differences pHs of 2.5, 1.5 and 0.5 gave different formulae of nanobelt $\text{NH}_4\text{V}_4\text{O}_{10}$, nanowire $(\text{NH}_4)2\text{V}_6\text{O}_{16}\cdot 1.5\text{H}_2\text{O}$ and nanobundle $(\text{NH}_4)_6\text{V}_{10}\text{O}_{28}\cdot 6\text{H}_2\text{O}$ respectively (Wang et al., 2008). This work obviously confirmed the effect of pH on structure, phase composition and morphology (Wang et al., 2008).

It is clearly that the reducing agent is a key role on size and morphology in hydrothermal synthesis. However, the effect of different acid in hydrothermal method is still challenge and need more development. Herein, we report the hydrothermal synthesis of vanadium oxide nanobelts in the present of different acids hoping for new sizes and morphology. Various techniques such as SEM with EDS, TGA-DTG, XRD and FT-IR were used to characterize the morphology, composition and structure of the as-obtained compounds.

EXPERIMENTAL

Preparation of nanobelts (1) and flower like nanobelts (2)

A mixture of NH_4VO_3 0.234 g (2 mmol), $\text{Zn}(\text{CH}_3\text{COO})_2\cdot 2\text{H}_2\text{O}$ 0.220 g (1 mmol) and H_2O (7.5 mL) in a molar ratio of 2:1:400 was stirred for 30 min. The pH of the yellow solution is 6. To adjust the solution pH to 3, hydrochloric acid for compound (1) and acetic acid for compound (2) were added drop wise with stirring. Then, the solutions were transferred and sealed in a 23 mL Teflon-lined stainless steel autoclave, and heated to 180 °C under autogenous pressure for 4 days before cooling to room temperature. The acidity of the products was constant at pH 3. The products were filtered off, washed with water, and air-dried at room temperature. The yield was 78% based on vanadium for nanobelts (1) and 82% flower like nanobelts (2).

Characterization

Melting points measurement

Melting points were determined in open glass capillaries and were measured on a Büchi melting point B-540 apparatus.

Powder X-ray diffraction analysis

The X-ray diffractometry (XRD) patterns were analyzed using X-ray diffractometer Rigaku (Japan) D/MAX RINT 2200-Ultima Plus. This diffractometer was equipped with graphite monochromatized $\text{Cu } K_\alpha$ radiation ($\lambda=1.54178 \text{ \AA}$). The accelerating voltage 40 kV, the applied current 30 mA and the scan rate 0.02 °/s were applied to record the pattern in the 2θ range of 2–70° which is used to characterize the crystalline phase of the products.

Field emission scanning electron microscope

The surface morphology was determined by field emission scanning electron microscope (FE-SEM) using a JEOL JSM-6700F microscope with an energy-dispersive X-ray (EDX) fluorescence analyzer. An accelerating voltage is 0.5 kV to 30 kV with vary magnifications.

Fourier transform infrared spectroscopy

The Fourier transform infrared (FT-IR) pattern was recorded on a Jasco 660 Plus spectrometer by standard KBr disk method. The measured range is between 400 to 4000 cm^{-1} .

Thermal analysis

Thermal analyses (thermogravimetry (TGA) and derivative thermogravimetry (DTG) are carried out on using Perkin Elmer TGA7 thermal analyzer. The sample was placed in platinum crucible (0.1 cm^3) and studied under air atmosphere with flowing rate of 10 °C min^{-1} .

RESULTS AND DISCUSSION

Compounds (1) and (2) are bronze thin platelets which are typical for vanadium oxide structure.¹ These compounds don't melt at limited temperature of a Büchi melting point apparatus, confirmed that their melting points are more than 350 °C. Fortunately, the hydrothermal preparations of (1) and

(2) gave the good yields of 78 % and 82% respectively.

SEM-EDX analysis

Nice looking crystalline compounds (1) and (2) were chosen for SEM/EDX analysis using the optical microscope. The crystal morphologies for the selection of compounds (1) and (2) were given in Figures 1 and 2 respectively.

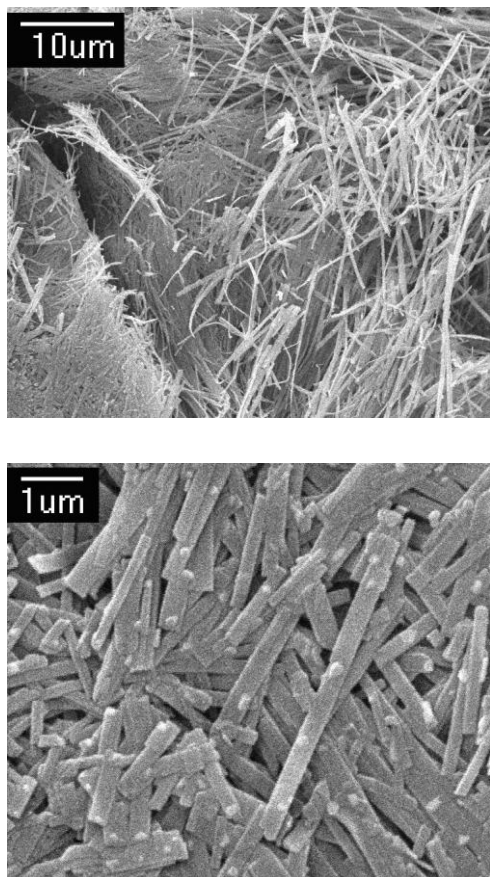


Figure 1 SEM images at different magnifications of nanobelt compound (1) adjusted the pH with hydrochloric acid.

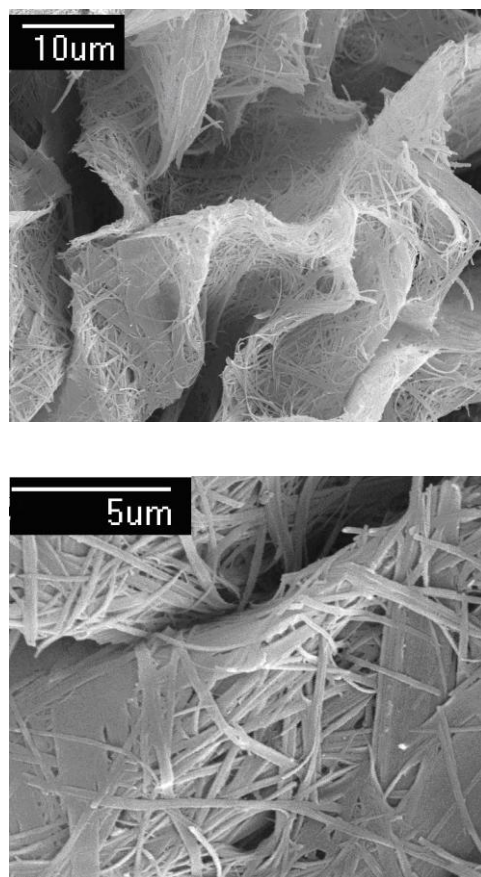


Figure 2 SEM images at different magnifications of flower like nanobelt compound (2) adjusted the pH with acetic acid.

At the pH 3 and in the presence of HCl, the morphology of compound (1) consists of nanobelts. At high magnification, the irregular separate nanobelts exhibit well-defined facets with the straight morphology, typical of the geometrical shape of nanobelts (Yua et al., 2006; Zhang et al., 2006).

The results from EDX spectra of compound (1) also showed that the nanobelts contain V, O and Cl atoms as shown in Figure 3. However, the atom ratio of V with O cannot be determined because of the overlapping peaks (Liu et al., 2004).

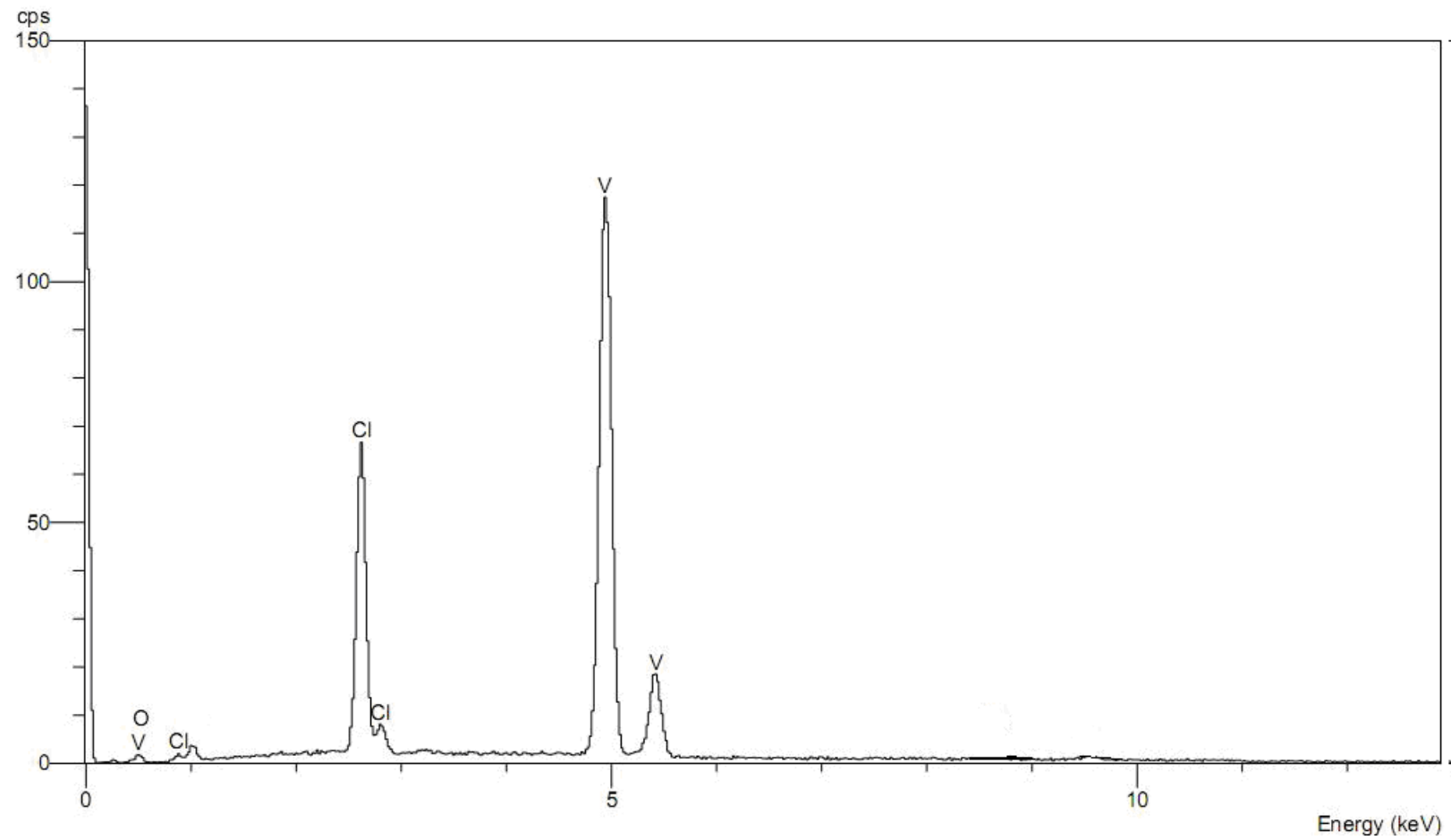


Figure 3 EDX pattern of the as-synthesized product (1).

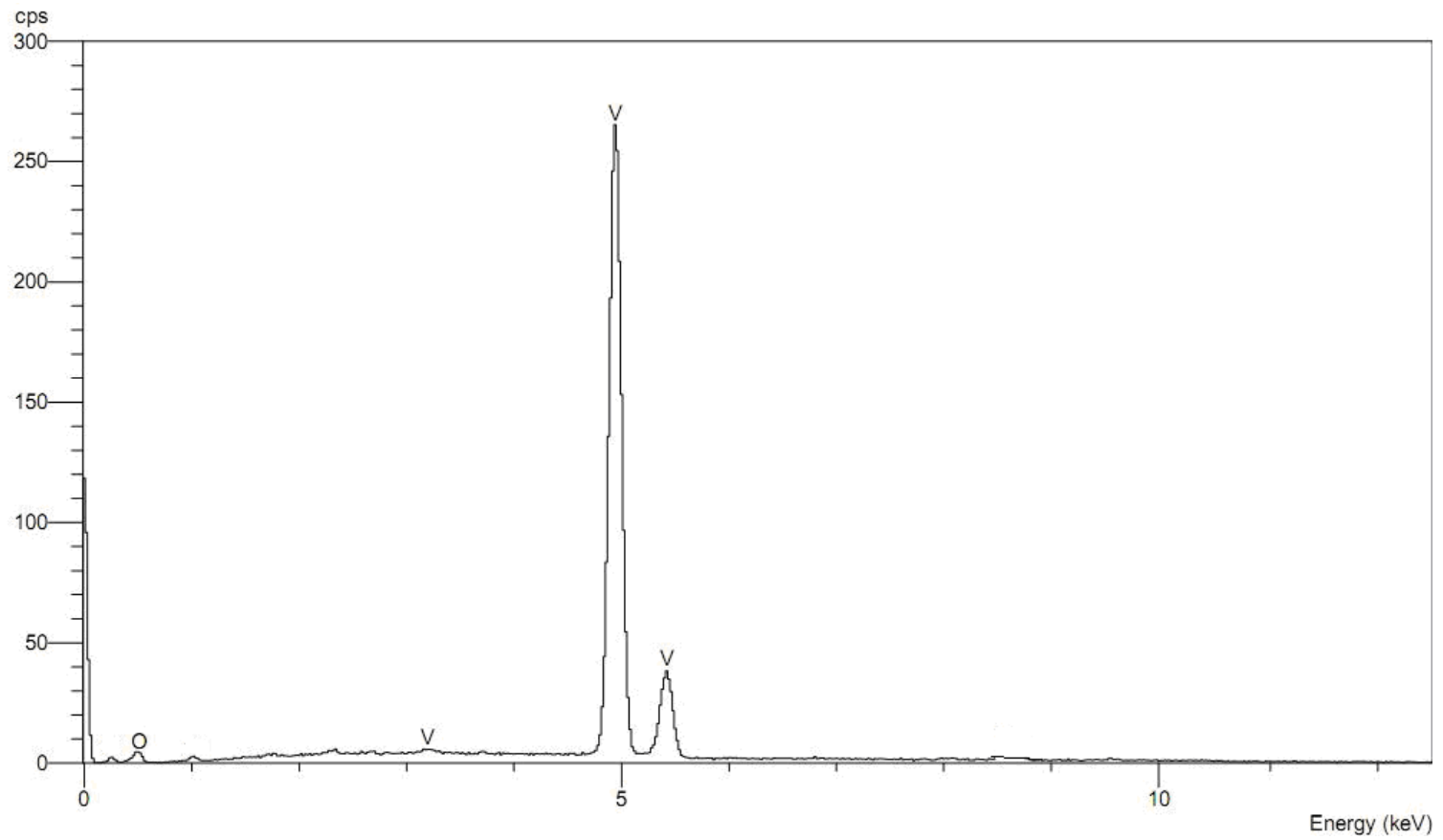


Figure 4 EDX pattern of the as-synthesized product (2).

The width and the length found in nanobelts (1) are in the range of 3–6 μm and 66 nm respectively. These morphology parameters are longer than those found in $\text{NH}_4\text{V}_4\text{O}_{10}$ nanobelts prepared using oxalic acid (Zhang et al., 2006), hydrochloric acid at pH 2.5 (Wang et al., 2008), but slightly shorter than those found in $(\text{NH}_4)_0.5\text{V}_2\text{O}_5$ nanobelts (Wang et al., 2011). Furthermore, some of the ribbon-like nanobelts stick together as shown in a high-magnification SEM image in Figure 1.

At the same pH as nanobelts (1), SEM images of compound (2) surprisingly exhibit the rectangular cross-section flower like nanobelt. The flower like nanobelt (2) reveals the entire smooth surface. Interestingly, these nanopetals were ca. 20-120 nm width, and several ten microns length which are extraordinary compare to typical ammonium vanadate nanobelts (Zhang et al., 2006). Its length

and the width are also greater than other vanadium oxide nanoflower (Parida et al., 2011; Maa et al., 2009). Astonishingly, these nanopetals of flowers like nanobelt (2) linked to each other to form 3D flowerlike structures as intensively demonstrated by the SEM images. In between the flower petals, many pores with different diameter sizes can be clearly seen. These pores may improve the chemical properties of the extraordinarily high capacity (Zhang et al., 2009). The EDX studies on compound (2) exhibited the existence of the elements of V and O as shown in Figure 4. Both compounds have similar patterns excepted the evidence elements of chlorine in compound (1).

Powder X-ray diffraction results

XRD was used to characterize the crystalline phase and the purity of these two compounds as shown in Figures 5 and 6.

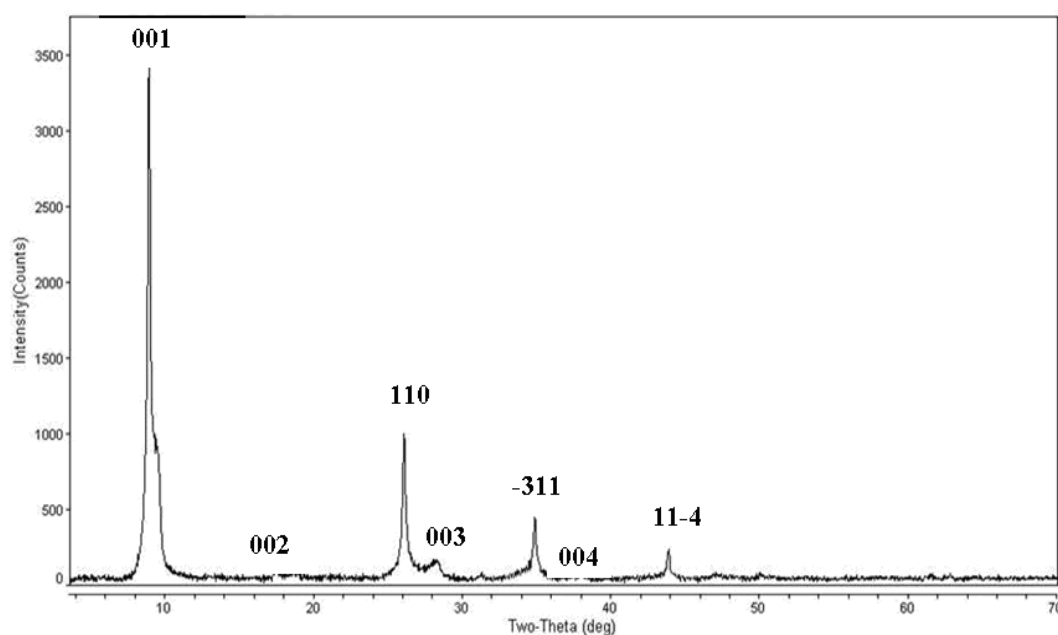


Figure 5 X-ray diffraction patterns of as obtained nanobelt (1) prepared in the present of hydrochloric acid.

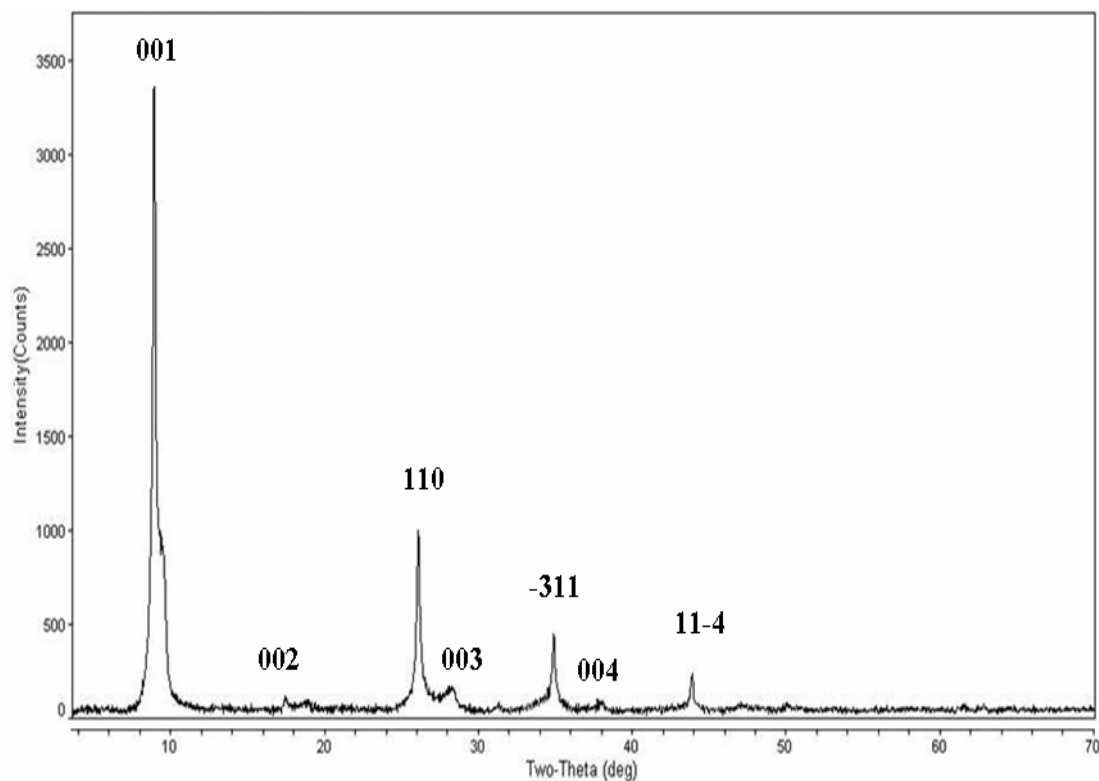


Figure 6 XRD patterns of as obtained flowerlike nanobelt (2) prepared in the presence of acetic acid.

The observed peaks of nanobelt (1) can be perfectly indexed to monoclinic crystalline phase which is in good agreement with the JCPDS, No. 31-0075 (JCPDS ICDD), confirming the phase composition of nanobelts (Zhang et al., 2006). All of the peaks in flowerlike nanobelt (2) are slightly shift (around 0.3°) to the higher degrees compare to nanobelt (1), indicating that the different acids have obviously effected on the crystalline phase. The XRD pattern were not similar to those of crystalline V_2O_5 (Maa et al., 2009; Menezes et al., 2009) and $(NH_4)_2VOCl_4$ (JCPDS, No. 20-1371) (JCPDS ICDD) or any zinc vanadium oxide compounds such as ZnV_2O_6 (Liu et al., 2009), $Zn_3(VO_4)_2$ (Pitale et al., 2011; Ni et al., 2010; Wang et al., 2012), $Zn_3(OH)_2V_2O_7 \cdot nH_2O$ (Ni et al., 2009; Ni et al., 2010; Ni et al., 2009), but similar to that given for $(NH_4)_4V_6O_{16} \cdot 1.5H_2O$

(JCPDS ICDD card no. 51-0376), nanowire $(NH_4)_{0.5}V_2O_5$ (Wu et al., 2004) □ nanobelt $(NH_4)_{0.5}V_2O_5$ (Wang et al., 2011), and $NH_4V_4O_{10}$ (Wang et al., 2011; Zhang et al., 2009; Wang et al., 2008; Zhang et al., 2006).

Furthermore, the strong and sharp peaks suggest that the as-synthesized products are well-crystallized. Considering the peaks in both compounds, the strong reflections at $2\theta < 15^\circ$ are 00l peaks, typical for the vanadium oxide layers (Liu et al., 2004). They appear that most of the nanobelts packed along (00l). Interestingly, no peaks of any other phases or impurities were detected. Compared our XRD pattern with the previously report $NH_4V_4O_{10}$ (Wang et al., 2011; Wang et al., 2008; Zhang et al., 2006) and $NH_{0.25}V_2O_5$ (Wang et al., 2011), the strongest peak

(001) is given in XRD pattern of the as-obtained sample, and the other peaks are relatively weak, indicating these nanobelts grow along (001) direction (Zhang et al., 2006).

Fourier transform infrared spectroscopy results

The infrared (FT-IR) spectra of compounds (1) and (2) are shown in Figures. 7 and 8 which clearly confirm the existence of ammonium vanadate hydrate compound (Wu et al., 2004; Yua et al., 2006; Wang et al., 2011; Wang et al., 2008). These two compounds show similar peak excepted the peaks which are over than 1600 cm^{-1} . The terminal V=O bonds in both compounds, occur at same 1002 cm^{-1} region (Yua et al., 2006; Wang et al., 2008; Menezes et al., 2009) which is slightly different from its starting materials NH_4VO_3 at 997 cm^{-1} (Phetmung et al., 2008), and slightly lower than that of the IR band of $\text{V}^{5+}=\text{O}$ in crystalline V_2O_5 showed at $1015\text{--}1020\text{ cm}^{-1}$ (Wang et al., 2008; Maa et al., 2009). The peak is attributed to the stretching vibration between vanadium and oxygen atoms and correspond to ribbon-like nanobelts ($(\text{NH}_4)_{0.5}\text{V}_2\text{O}_5$) (Wu et al., 2004; Wang et al., 2011; Wang et al., 2008). The FT-IR bands found at 766 cm^{-1} is ascribed to V-O-V antisymmetric stretching mode (Yua et al., 2006), but the bands found close to 540 cm^{-1} are corresponded to V-O-V bending (Wu et al., 2004; Yua et al., 2006; Wang et al., 2008; Menezes et al., 2009). No evidence band below 500 cm^{-1} which correspond to the stretching vibration Zn-O-V (Yua et al., 2006). No evidences of Zn-Cl or V-Cl vibration bands (Wellington et al., 2008). The stretching and bending vibrations of water appear at 3426 cm^{-1} and 1632 cm^{-1} of compound (1) and 3426 cm^{-1} and 1632 cm^{-1} of compound (2) (Wu et al., 2004; Yua et al., 2006).

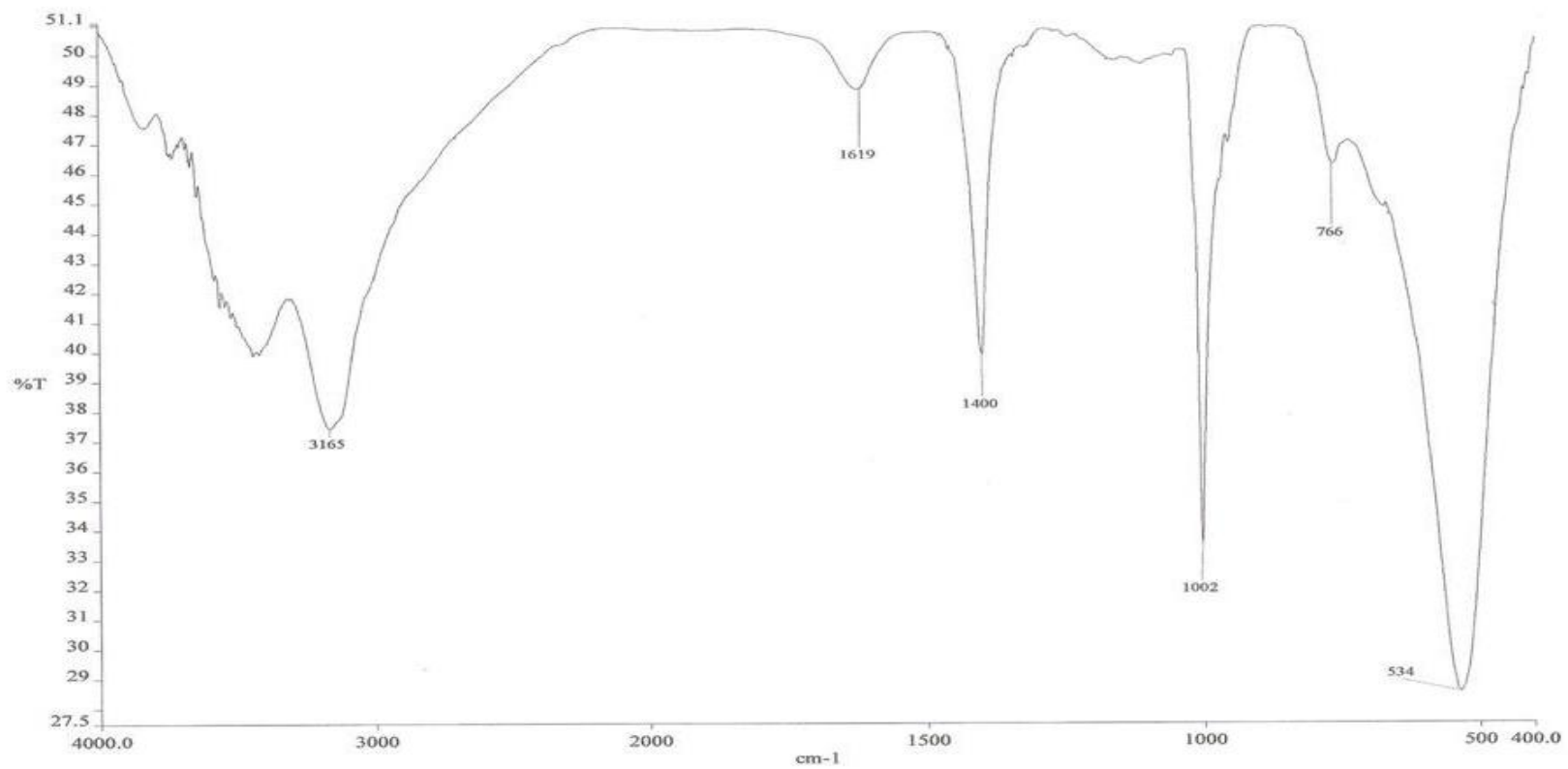


Figure 7 The FT-IR graph of compounds (1).

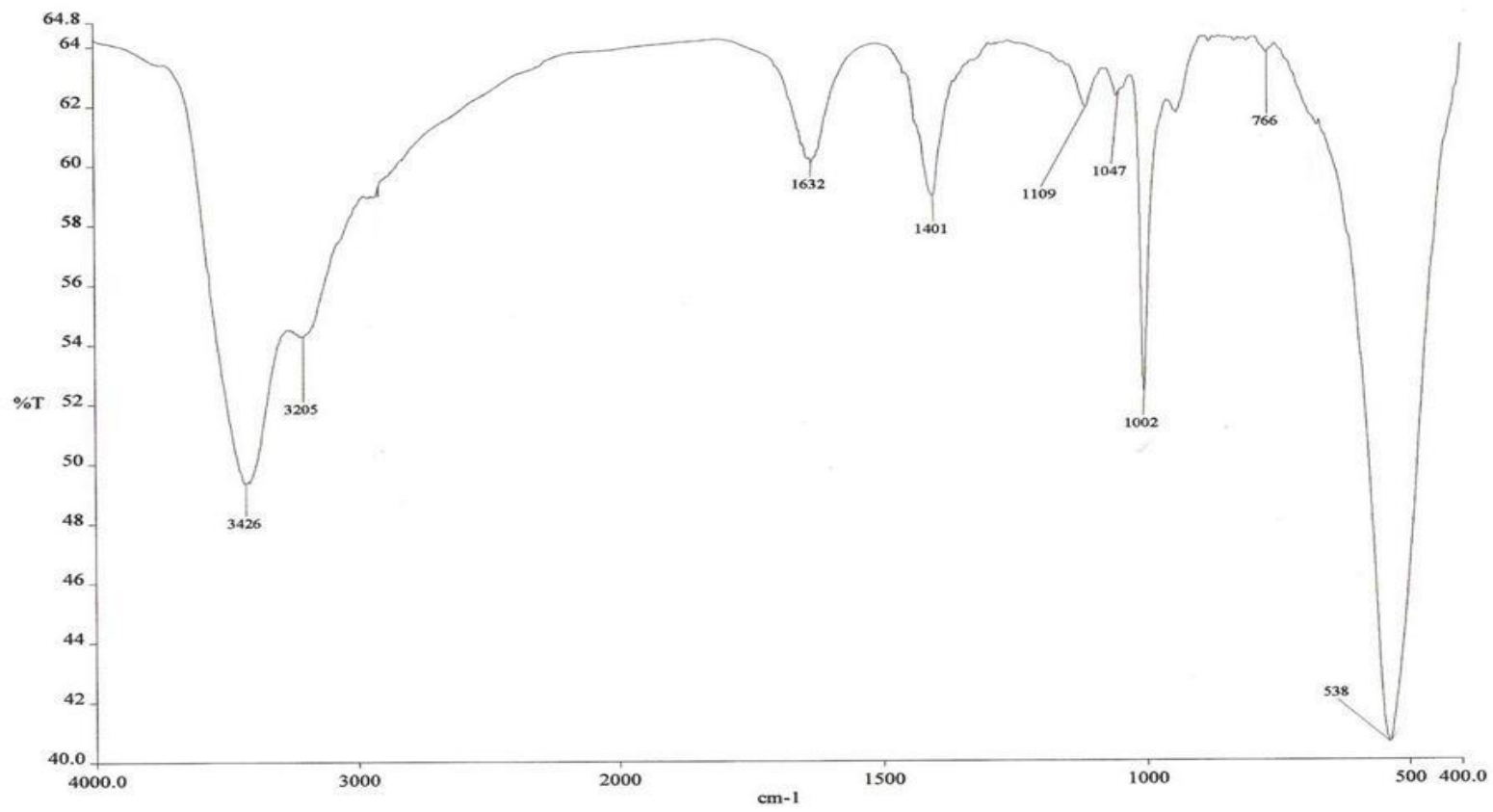


Figure 8 The FT-IR graph of compounds (2).

From both compounds, the N–H stretching and bending of ammonium group bands are at around 3100-3200 cm^{-1} and 1400 cm^{-1} as appeared in $(\text{NH}_4)_{0.26}\text{Na}_{0.14}\text{V}_2\text{O}_5$ and are ascribed to the asymmetric stretching vibrations and the symmetric bending vibration of $(\text{NH}_4)^+$ (Wu et al., 2004; Yua et al., 2006; Wang et al., 2008; Fei et al., 2008). The peaks at over 3400 and around 1610-1640 cm^{-1} can be assigned to the symmetric stretching and bending vibrations of H–O–H of H_2O , respectively.

Based on FT-IR results, it might be implied that no certain amount of chloride ion in nanobelt (1) is embedded between the vanadium oxide layers, but water molecules. Thus, the chemical formula of the as-obtained nanobelts (1) and flower like nanobelt (2) could be described as $(\text{NH}_4)_4\text{V}_6\text{O}_{16}\bullet 1.5\text{H}_2\text{O}$ and

$\text{NH}_4\text{V}_4\text{O}_{10}\bullet n\text{H}_2\text{O}$ respectively, which are the family of $\text{NH}_4\text{V}_4\text{O}_{10}\bullet n\text{H}_2\text{O}$.

Thermal analysis results of nanobelts (1) and flowerlike nanobelts (2)

Thermal decomposition TGA and DTG profiles of these two compounds are similarity as shown in Figures. 9 and 10.

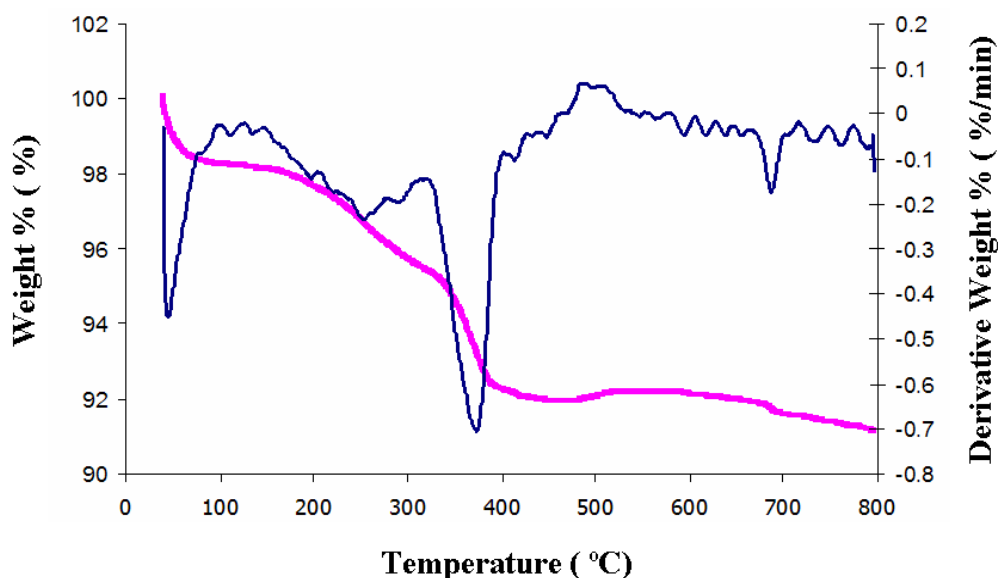


Figure 9 TGA-DTG curves of nanobelts (1).

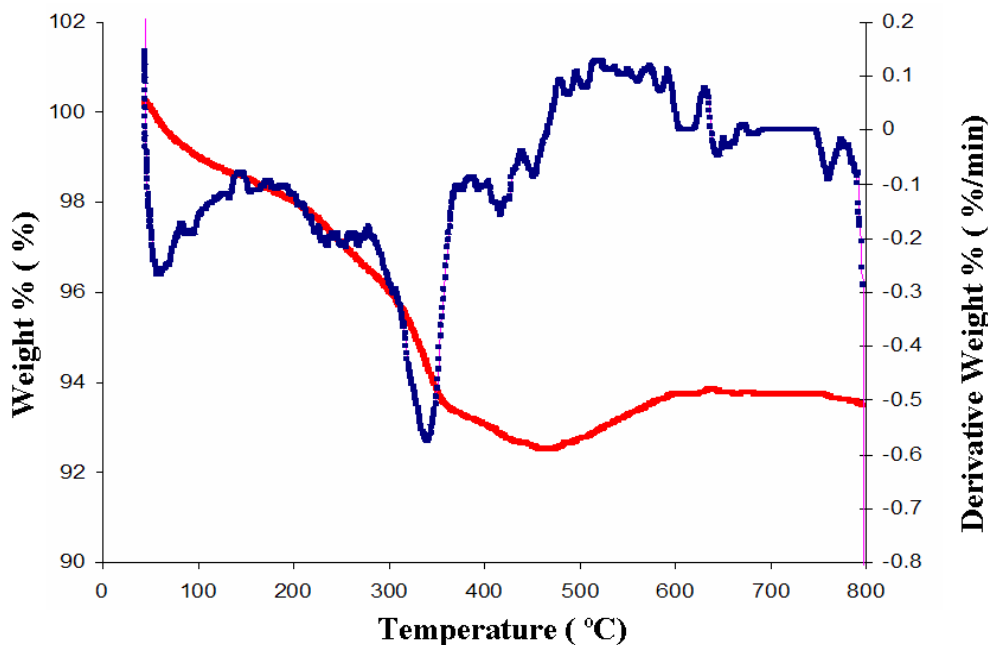


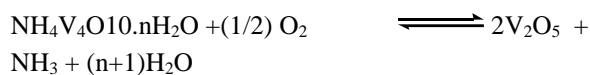
Figure 10 TGA-DTG curves of flower like nanobelts (2).

The DTG curve of nanobelt (1) and flower like nanobelts (2) records the endothermic peaks. The two sharp endothermic peaks occurred during the temperature range of 40-220 °C and range 221-440 °C. The other peaks appear very small endothermic (Maa et al., 2009).

The complicated TGA curve registers a total weight loss about 9.5 % in nanobelt (1) and about 8.5 % in flower like nanobelts (2). These total weight losses are very small amount which are related to the decomposition of water molecules and the phase transformations (Ni et al., 2009). Although these two thermograms are complicated, an only 1% different weight loss between nanobelts (1) and flowerlike nanobelts (2) may point to the presence of chloride anion of nanobelts (1) as shown in the EDX spectrum.

However, for these two compounds, the first thermal decomposition step represents the removal of physisorbed water. Next step of decomposition corresponds to the complete decomposition of NH_3 . The third step in compound (1) is corresponded to the decomposition of chloride. Interpreting from their thermograms, it can be summarized the

decomposition of compounds (1) and (2) as the equations below.



As known, when the pH of hydrochloric acid of the system is smaller than 3, it plays an important role to control the formula structure, size and morphologies (Wang et al., 2008). For our work, since the shape and morphologies differed by the presence of different acids, it can be deduced that acids play a crucial role to improve the morphology of the products when the pH of the system is 3. Although the mechanism of the effect of acids on the shape and morphology of the products is unclear, it would be of great importance in hydrothermal synthesis, and worth to be further research.

CONCLUSION

By using the same starting materials and conditions except the types of acids (hydrochloric vs. acetic acids), hydrothermal synthesis of compounds (1) and (2) gave the good yield of 78% and 82% respectively. The SEM observations confirmed a plate-like

morphology and exclusively belt-like nanostructures of (1) with length of 3–6 micrometers and the flower like nanobelt morphology of (2) with the length of several tens of micrometers and nanopetals were ca. 20-120 nm width, and several ten microns length which are extraordinary which linked to each other to form 3D flowerlike structures, indicating that the different acids have obviously effected on the crystalline morphology. Their XRD patterns reveal the set of 1 D vanadium oxide nanobelts, characteristic of (001) reflections. Based on the evidences of FT-IR, XRD and TGA, the chemical formula of the as-obtained nanobelt (1) and flowerlike nanobelt (2) are the family of $\text{NH}_4\text{V}_4\text{O}_{10} \cdot n\text{H}_2\text{O}$.

ACKNOWLEDGMENT

We gratefully acknowledge to X-ray techniques laboratory of MTEC for XRD measurement and a partial grant from Department of Chemistry, Thaksin University.

REFERENCES

- Chang, K-H. and Hu, C-C. (2007) 'H₂V₃O₈ single-crystal nanobelts: hydrothermal preparation and formation mechanism', *Acta Mater*, Vol. 55, pp.6192-6197.
- Chernova, N.A., Roppolo, M., Dillon, A.C. and Whittingham, M.S. (2009) 'Layered vanadium and molybdenum oxides: batteries and electrochromics', *J. Mater. Chem*, Vol. 19, pp.2526–2552.
- Fei, H-L., Shen, Z-R., Wang, J-G., Zhou, H-J., Ding, D-T. and Chen, T-H. (2008) 'Novel bi-cation intercalated vanadium bronze nano-structures for stable and high capacity cathode materials', *Electrochem. Commun*, Vol. 10, pp.1541–1544.
- JCPDS ICDD card No. 31-0075.
- JCPDS ICDD card No. 51-0376.
- JCPDS, No. 20-1371.
- Kong, L., Liu, Z., Shao, M., Xie, Q., Yu, W. and Qian, Y. (2004) 'Controlled synthesis of single-crystal VO_x·nH₂O nanoribbons via a hydrothermal reduction method', *J. Solid State Chem*, Vol. 77, pp.690-695.
- Law, M., Goldberger, J. and Yang, P.D. (2004) 'Semiconductor nanowires and nanotubes', *Annu. Rev. Mater. Res*, Vol. 34, pp.83-122.
- Lin Xu, Liqiang Mai, Chunhua Han, Xu Xu and Yanzhu Luo, (2010) 'Vanadium oxide nanostructures for lithium battery applications world', *J. Eng.*, Vol.7 supplement 2, pp.1-4.
- Liu, H. and Tang, D. (2009) 'Synthesis of ZnV₂O₆ powder and its cathodic performance for lithium secondary battery', *Mater. Chem. Phy*, Vol. 114, pp.656- 659.
- Liu, J., Li, Q., Wang, T., Yu, D. and Li, Y. (2004) 'Hydrothermal synthesis, electrical transport, and magnetic properties', *Angew. Chem. Int. Ed.*, Vol. 43, No. 28, pp.5048- 5050 and reference therein.
- Lui, J., Wang, X., Peng, Q. and Li, Y. (2005) 'Vanadium pentoxide nanobelts: highly selective and stable ethanol sensor materials', *Adv. Mater*, Vol. 17, No. 6, pp.764-767.
- Lutta, S.T., Dong, H., Zavalij, P.Y. and Whittingham, M.S. (2005) 'Synthesis of vanadium oxide nanofibers and tubes using polylactide fibers as template', *Mater. Res. Bull*, Vol. 40, pp.383-393.
- Maa, J., Wua, Q. and Chen, Y. (2009) 'An oxides-hydrothermal approach from bulky V₂O₅ powder to V₃O₇ H₂O nanoribbons or V₃O₇ nanoflowers in various ethanol/water mixed solvent', *Mate. Res. Bull*, Vol. 44, pp.1142–1147.
- Menezes, W.G., Reis, D.M., Benedetti, T.M., Oliveira, M.M., Soares, J.F., Torresi, R.M. and Zarbin, A.J.G. (2009) 'V₂O₅ nanoparticles obtained from a synthetic bariandite-like vanadium oxide: Synthesis, characterization and electrochemical behavior in an ionic liquid', *J. Colloid. Interf. Sci*, Vol. 337, pp.586–593.
- Ni, S., Lin, S., Pan, Q., Huang, K., Yang, F. and He, D. (2009) 'Crystallized Zn₃(OH)₂V₂O₇·nH₂O: Hydrothermal synthesis and magnetic property', *J. Alloy Compd*, Vol. 477, pp.L1–L3.
- Ni, S., Wang, X., Zhou, G., Yang, F., Wang, J. and He, D. (2010) 'Crystallized Zn₃(VO₄)₂: synthesis, characterization and optical property', *J. Alloy Compd*, Vol. 49, pp.378–381.
- Ni, S., Zhou, G., Lin, S., Wang, X., Pan, Q., Yang, F. and He, D. (2009) 'Hydrothermal synthesis of Zn₃(OH)₂V₂O₇·nH₂O nanosheets and its application in lithium ion battery', *Mater. Lett*, Vol. 63, pp.2459–2461.
- Ni, S., Zhou, G., Wang, X., Sun, X., Yang, F., Liu, Y. and He, D. (2010) 'Synthesis of Zn₃(OH)₂V₂O₇·nH₂O hierarchical nanostructures and their photoluminescence properties', *Mater. Chem. Phys*, Vol. 120, pp.426–430.
- O'Dwyer, C., Navas, D., Lavayen, V., Benavente, E., Santa Ana, M.A., González, G., Newcomb, S.B. and Sotomayor Torres, C. M. (2006) 'Nano-urchin: the formation and structure of high-density spherical clusters of vanadium oxide nanotubes', *Chem. Mater*, Vol. 18, No 13, pp. 3016–3022.
- O'Dwyer, C., Lavayen, V., Santa Ana, M.A., Benavente, E., González, G. and Sotomayor Torres, C.M. (2007) 'Anisotropic vanadium oxide nanostructured host matrices for lithium ion intercalation', *Res. Lett. Phys. Chem*, Vol. 2007, pp.1-5.
- Parida, M.R., Vijayan, C., Rout, C.S., Suchand Sandeep, C.S., Philip, R. and Deshmukh, P.C. (2011) 'Room temperature ferromagnetism and optical limiting in V₂O₅ nanoflowers synthesized by a novel method', *J. Phys. Chem. C*, Vol. 115, pp.112–117.
- Phetmung, H., Kim, T.W., Hwang, S.J. and Choy, J. H. (2008) 'A simple and direct method for synthesis of vanadium oxide ribbon-like nanobelts', *J. Iran. Chem. Soc*, Vol 5, pp.706-711.

- Pillai, K.S., Krumeich, F., Muhr, H.J., Niederberger, M. and Nesper, R. (2000) 'The first oxide nanotubes with alternating inter-layer distances', *Solid State Ionics*, Vol. 141-142, pp.185-190.
- Pitale, S.S. Gohain, M., Nagpure, I.M., Ntwaeaborwa, O.M., Bezuidenhout, B.C.B. and Swart, H.C. (2011) 'A comparative study on structural morphological and luminescence characteristics of $Zn_3(VO_4)_2$ phosphor prepared via hydrothermal and citrate-gel combustion routes', *Physica B*, Vol. 1, pp.1-4.
- Spahr, M.E., Stoschitzki-Bitterli, P., Nesper, R., Haas, O. and Novák, P. (1999) 'Vanadium oxide nanotubes a new nanostructured redox-active material for the electrochemical insertion of lithium', *J. Electrochem. Soc.*, Vol. 146, No. 8, pp.2780-2783.
- Stanley Whittingham, M. (2004) 'Lithium batteries and cathode materials', *Chem. Rev.*, Vol. 104, pp.4271-4301.
- Wang, H., Huang, K., Huang, C., Liu, S., Ren, Y. and Huang, X. (2011) '(NH₄)_{0.5}V₂O₅ nanobelt with good cycling stability as cathode material for Li-ion battery', *J. Power Sources*, Vol. 196, pp.5645-5650.
- Wang, M., Shi, Y. and Jiang, G. (2012) '3D hierarchical $Zn_3(OH)_2V_2O_7 \cdot 2H_2O$ and $Zn_3(VO_4)_2$ microspheres: synthesis, characterization and photoluminescence', *Mater. Res. Bull.*, Vol. 47, pp.18-23.
- Wang, N., Chen, W., Mai, L. and Dai, Y. (2008) 'Selected-control hydrothermal synthesis and formation mechanism of 1D ammonium vanadate', *J. Solid State Chem.*, Vol. 181, pp.652-657.
- Wellington, K.W., Kaye, P.T. and Watkins, G.M. (2008) 'Designer ligands. Part 14. Novel Mn(II), Ni(II) and Zn(II) complexes of benzamide- and biphenyl-derived ligands', *Arkivoc*, Vol. XVII, pp.248-264.
- Wu, X., Tao, Y., Dong, L. and Hong, J. (2004) 'Synthesis and characterization of self-assembling (NH₄)_{0.5}V₂O₅ nanowires', *Mater. Chem.*, Vol. 14, pp.901-904.
- Xu, H., He, W., Wang, H. and Yan, H. (2004) 'Solvothermal synthesis of K₂V₃O₈ nanorods', *J. Cryst. Growth.*, Vol. 260, pp. 447-450.
- Yua, J., Liu, S., Cheng, B., Xiong, J., Yu, Y. and Wang, J. (2006) 'Polymer-directed large-scale synthesis of single-crystal vanadium oxide nanobelts', *Mater. Chem. Phys.*, Vol. 95, pp.206-210.
- Zhang, K-F., Zhang, G-Q., Liu, X., Su, Z-X. and Li, H-L. (2006) 'Large scale hydrothermal synthesis and electrochemistry of ammonium vanadium bronze nanobelts', *J. Power Sources*, Vol. 157, pp.528-532.
- Zhang, G-Q. and Zhang, S-T. (2009) 'Charge-discharge mechanisms of ammonium vanadium bronze NH₄V₄O₁₀ nanobelts as cathode for lithium-ion battery', *Power and Energy Engineering Conference*, pp. 1-4.
- Zhang, S., Li, Y., Wu, C., Zheng, F. and Xie, Y. (2009) 'Novel flowerlike metastable vanadium dioxide (b) micronanostructures: facile synthesis and application in aqueous lithium ion batteries', *J. Phys. Chem. C*, Vol. 113, pp.15058-15067.